A thesis of

Accretion Scenario of Black Hole X-ray Binaries During Outburst

submitted by

Geethu Prabhakar

in partial fulfillment for the award of the degree of

Doctor of Philosophy

Department of Earth and Space Sciences
Indian Institute of Space Science and Technology
Thiruvananthapuram, India

August 2023

Certificate

This is to certify that the thesis titled ***Accretion Scenario of Black Hole X-ray Binaries During Outburst*** submitted by **Geethu Prabhakar**, to the Indian Institute of Space Science and Technology, Thiruvananthapuram, in partial fulfillment for the award of the degree of **Doctor of Philosophy** is a bona fide record of the original work carried out by him/her under my supervision. The contents of this thesis, in full or in parts, have not been submitted to any other Institute or University for the award of any degree or diploma.

Dr. Samir Mandal
Supervisor & Professor
Department of Earth & Space Sciences

Dr. Rama Rao Nidamanuri
Professor & Head
Department of Earth & Space Sciences

Place: Thiruvananthapuram
Date: August 2023

Declaration

I declare that this thesis titled ***Accretion Scenario of Black Hole X-ray Binaries During Outburst*** submitted in partial fulfillment for the award of the degree of **Doctor of Philosophy** is a record of the original work carried out by me under the supervision of **Dr. Samir Mandal**, and has not formed the basis for the award of any degree, diploma, associateship, fellowship, or other titles in this or any other Institution or University of higher learning. In keeping with the ethical practice in reporting scientific information, due acknowledgments have been made wherever the findings of others have been cited.

Place: Thiruvananthapuram
Date: August 2023

Geethu Prabhakar
(SC17D009)

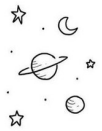

This thesis is dedicated to my beloved parents, sister and husband.

Acknowledgements

First, I would like to thank *Indian Institute of Space Science and Technology* (IIST), for providing me with the opportunity to conduct my research work. I am thankful to the Director of IIST for providing the necessary facilities for the completion of my thesis.

I would like to acknowledge and express my gratitude to my supervisor, Prof. Samir Mandal, for his constant support and motivation. I greatly appreciate his commitment to respond to any of my academic queries, regardless of time. His unwavering patience and willingness to assist me whenever required are highly valued and appreciated.

I express my deep sense of gratitude to my collaborators Dr. Anuj Nandi, Dr. Santabrata Das, Athulya M P, Bhuvana G R., and Dr. Indu Kalpa Dihingia for their invaluable contribution. I learned a lot through the discussions I had with them.

I would like to thank my doctoral committee members Prof. Anandmayee Tej, Prof. Anand Narayanan, Dr. Dinesh N. Naik, and Dr. Sachindra Naik for helping me to improve the quality of my work through their valuable suggestions. I also thank our faculty members, Prof. Jagadheep D, Prof. Sarita Vig, and Prof. Resmi Lekshmi for their support and suggestions.

One of the most unforgettable experiences during my Ph.D. life was the time spent with my friends on the campus: Babitha, Arun, Amal, Sam, Sanjay, Visakh, Minha, Vibin, Fransis and Nibin. I am truly grateful for the countless hours of conversations we had, on a wide range of topics, nearly everything in the universe, and I will surely miss them. I am thankful to my hostel mates Anna, Anu, Sreelakshmi, Haritha, Soumya, Ann Mary for making my hostel life lively and memorable. I am indebted to my senior Dr. Aneesha, who has been a great mentor and friend to me during my time on the campus. She has been an unwavering source of encouragement and support during all of the emotions and obstacles. I also acknowledge our lab assistant, Sai Krishnan, for his help and support.

As a personal note, achieving all of this would not have been possible without my parents' sacrifices. I am deeply grateful to them for their unwavering faith in me and my abilities, which has been the driving force behind my academic achievements. I owe a special thanks to my sister, who instilled confidence in me, and helped me in realizing my strengths. I would like to express my utmost gratitude to my husband Mr. Renjith, who has been my constant support through all the challenges and triumphs of life, particularly

during the highs and lows of my research career, and for providing me with emotional support during difficult times. I've also been lucky to have very supportive in-laws who are always there for me.

Geethu Prabhakar

Abstract

In an X-ray binary (XRB) system, a compact object with strong gravity accretes mass from the donor, often a young or evolved star. As the transferred matter falls onto the compact object, potential energy is released, resulting in the emission of X-ray radiation. Some of these systems display episodes of active (outburst) and quiescent phases consecutively. This thesis investigates the accretion scenario of different black hole X-ray binaries (BH-XRBs) during their outbursts.

Chapter 1 introduces a general overview of accretion processes. We comprehensively discuss various accretion scenarios focusing on transient black hole XRBs. We explore the spectral and temporal variability and state classification of these systems. Also, we review outflows/jet and accretion disc wind associated with the system.

The purpose of Chapter 2 is to brief various space X-ray instruments used in this study and the data reduction techniques associated with each of them. We discuss the methods of analyzing X-ray data: spectral and timing analysis. A quick overview of different models used for fitting the X-ray spectra of black hole XRBs and related physical phenomena are also provided in this chapter. Also, we briefly discuss the modelling of the power density spectra.

In Chapter 3, we aim to unveil the accretion scenario of the galactic XRB source MAXI J1820+070 in its 2018 double outburst. The study is performed using observations obtained from the telescopes *Swift/XRT, NICER, NuSTAR* and *AstroSat*. We carried out spectral modelling independently for *XRT* and *NICER* observations and studied the evolution of various physical parameters and the hardness-intensity diagram of the outburst. Then we extended the study by modelling the simultaneous wideband *XRT-NuSTAR, NICER-NuSTAR* and *AstroSat* observations using phenomenological and reflection models. The evolution of model parameters from both studies is thoroughly analysed. The timing analysis of the source is carried out using the *NICER* observations of the outburst. We look for time variability in the data, and finally, its connection with the spectral characteristics is studied in this chapter.

Chapter 4 discusses the spectro-temporal analysis of the galactic XRB source 4U 1543−47 in its 2021 outburst using data from three instruments, *NICER, NuSTAR* and *AstroSat*. Wideband phenomenological and reflection modelling is carried out for simultaneous *NICER-NuSTAR* and *AstroSat* observations. The spectra of the source show the

presence of a strong and dynamic absorption feature at $\sim 8-11$ keV, which has never been observed in any XRB before. A comprehensive spectral study of the outburst is performed using *NICER* observations, and the hardness-intensity diagram of the outburst is generated. Also, we performed timing studies using the *NICER, NuSTAR* and *AstroSat* observations during the first 100 days of the outburst.

Next, in Chapter 5, we have thoroughly investigated the origin of the absorption features observed at $\sim 8-11$ keV in the spectra of the 2021 outburst of 4U 1543−47. This study is based on the *NuSTAR* observations of the outburst. Different possibilities behind the origin of this absorption feature and their role in regulating the accretion scenario are studied. *NuSTAR* data also show a neutral absorption feature at ~ 7.1 keV. The correlated behaviour of the neutral and ionized absorption components is also closely examined.

In Chapter 6, we summarize the findings from the study and discuss the future perspectives.

Contents

List of Figures

List of Tables

Abbreviations

AGN	Active Galactic Nuclei
ARF	Ancillary Response Files
ASAS-SN	All-Sky Automated Survey for SuperNovae
BAT	Burst Alert Telescope
BH	Black Hole
BHL	Bondi-Hoyle-Lyttleton
BH-XRB	Black Hole X-Ray Binary
CCD	Charge-Coupled Devices
CM	Centre of Mass
CZTI	Cadmium-Zinc-Telluride Imager
DIM	Disc Instability Model
EW	Equivalent Width
FPM	Focal Plane Module
FW	Fast Windowed mode
FWHM	Full-width at half maximum
GMRT	Giant Metrewave Radio Telescope
GRB	Gamma Ray burst
GSC	Gas Slit Camera
GTI	Good Time Interval
HEASARC	High Energy Astrophysics Science Archive Research Center
HFQPO	High-frequency QPO
HID	Hardness-Intensity diagram
HIMS	Hard intermediate state
HMXB	High Mass X-ray Binary
HR	Hardness ratio
HRD	Hardness-RMS diagram
HSS	High/soft state

HWHM	Half-width at half maximum
IM	Imaging mode
ISCO	Innermost Stable Circular Orbit
ISM	Interstellar Medium
ISRO	Indian Space Research Organization
ISS	International Space Station
LAXPC	Large Area X-ray Proportional Counters
LFQPO	Low-frequency QPO
LHS	Low/hard state
LMXB	Low Mass X-ray Binary
MAXI	Monitor of All-sky X-ray Image
MJD	Modified Julian Date
MPU	Measurement and Power Unit
NICER	Neutron star Interior Composition Explorer
NS	Neutron Star
NuSTAR	Nuclear Spectroscopic Telescope Array
PHA	Pulse Height Amplitude
PC	Photon Counting mode
PD	Photo-Diode mode
PDS	Power Density Spectrum
PI	Pulse Invariant
QPO	Quasi-periodic Oscillations
RA	Right Ascension
RID	RMS-Intensity diagram
RMF	Response Matrix Files
RMS	Root-Mean-Square
RPM	Relativistic Precession Model
SDD	Silicon Drift Detectors
SIMS	Soft intermediate state
SMBH	Super-massive black holes
SPL	Steep Powerlaw State
SXT	Soft X-ray Telescope
UVOT	Ultraviolet/Optical Telescope
VLBA	Very Long Baseline Array
VLBI	Very Long Baseline Interferometry

WD	White Dwarf
WT	Windowed Timing mode
XRB	X-Ray Binary
XRC	X-ray concentrators
XRT	X-ray Telescope
XTI	X-ray Timing Instrument

Nomenclature

a	Binary separation
a_*	Spin parameter
A_{Fe}	Iron abundance
$A_{Fe,\odot}$	Solar abundance of Iron
c	Velocity of light
cm	Centimeter
c_s	Sound speed
cov_frac	Covering fraction
Dec	Declination
dof	Degrees of freedom
D_{10}	Distance to the source in 10 kpc
G	Gravitational constant
h	Planck constant
h	lamp-post height
H	Half thickness of the accretion disc
Hz	Hertz
J	Spin angular momentum
k_B	Boltzmann constant
keV	kiloelectron volt
kpc	kiloparsec
L	Luminosity
L_{Edd}	Eddington luminosity
m_e	Mass of electron
m_p	Mass of proton
M	Mass of the compact object
M_{BH}	Mass of the black hole
M_s	Mass of the companion star

$\dot{M}$	Accretion rate
$\dot{M}_{Edd}$	Eddington accretion rate
$M_{\odot}$	Solar mass
n_H	Hydrogen column density
Ni	The *NICER* instrument
Nu	The *NuSTAR* instrument
P_{∞}	Pressure at infinity
q	Mass ratio
q	Emissivity index
Q	Q-factor
r_g	Gravitational radius
r_{ISCO}	Radius of ISCO
r_{in}	Apparent inner radius of the disc
R_{in}	Inner radius of the disc
R_{out}	Outer radius of the disc
$R_{\odot}$	Solar radius
R_s	Radius of the companion star
R_f	Reflection fraction
s	seconds
t_{dyn}	Dynamical timescale
t_{th}	Thermal timescale
t_{visc}	Viscous timescale
T_{bb}	Blackbody temperature
T_e	electron tempertature
$T_{\rm eff}$	Effective temperature
T_{expo}	Exposure time
T_{in}	Inner disc temperature
T_{th}	Thermal temperature
θ	Accretion disc inclination
τ	Optical depth
ν	Frequency
ν_c	Characteristic frequency of QPO
$\mathcal{M}$	Mach number
γ	Adiabatic index
Γ	Photon index or Spectral index

η	Radiative efficiency of accretion
ρ_∞	Density at infinity
ξ	Ionization parameter
σ_T	Thomson scattering cross-section
Σ	Surface density
χ^2_{red}	Reduced χ^2

Chapter 1

Introduction

The dramatic advancements in science during the twentieth century changed our perception of nature. A much better understanding of the celestial bodies and the universe has been achieved through radical technological developments. The remarkable progress in observational techniques has enabled us to access the entire electromagnetic spectrum, leading to the discovery of more and more energetic events at high-energy (X-ray to Gamma-ray) wavelengths. It has been found that gravity is the source of energy for celestial bodies, particularly for compact objects, through accretion, the process of accumulating matter onto a compact object from its surroundings under the influence of strong gravity. The gravitational potential energy released from this accreted matter is believed to be the source that powers the most luminous objects in the universe.

1.1 Compact Objects and Properties

Compact objects are astrophysical systems with enormous density left by the stars at their end stages of evolution. Stars are born in molecular clouds by the collapse of gas under gravity. It causes gas to warm and eventually become hot enough to start nuclear fusion in its core and release immense amounts of energy. This way, stars shine and maintain an equilibrium between gravitational pull towards the core and outward force due to the pressure gradient. Once the fuel gets exhausted, the star collapses into a denser entity called the compact object due to the inward pull of gravity. The extent to which it collapses will lead to the formation of different types of compact objects; they are white dwarfs (WD), neutron stars (NS) and black holes (BH), depending on the mass of the stellar core.

In WDs, the degenerate electron pressure balances the gravity and prevents it from further collapse. This is the end product of a low-mass star. Chandrasekhar (1939) deduced a theoretical limit for the mass of the WD as 1.4 $M_{\odot}$ beyond which it would undergo

gravitational collapse. Out of all the three types of compact objects, WD is the most common outcome of stellar evolution. The observed lowest and highest mass of the WDs are 0.17 $M_\odot$ (Kilic et al., 2007) and 1.35 $M_\odot$ (Burleigh & Jordan, 1998) respectively. Once the gravity exceeds electron degeneracy pressure, the neutron degeneracy pressure comes into action, and it supports the core from further collapse. Such systems are called NSs. The lowest detected mass limit of NSs is 1.15−1.2 $M_\odot$, and the highest limit is 2.4 $M_\odot$ (Lattimer, 2012). However, Rhoades & Ruffini (1974) used a causality argument to propose a maximum neutron star mass of $3.2M_\odot$. With a further increase of the stellar core mass, no mechanism can support the collapse against gravity, and the core completely collapses into a singularity, forming a BH. Studies reveal that there may exist a 'mass gap' between the highest mass NS and the lowest mass BH (Farr et al., 2011). The WD and NS have a solid surface, whereas the BH does not have a well-defined surface. Instead, there exists a region known as the *event horizon*, which separates the interior of the BH from its surroundings.

This thesis deals with the binary system of a stellar-mass BH and a normal star. I shall thus focus more of my discussion on BHs. In general relativistic point of view, BHs are simple objects characterized by only three parameters, their mass M, spin angular momentum J, and electric charge Q (Israel, 1967, 1968; Carter, 1971). A Schwarzschild black hole is a spherically symmetric, non-rotating, and electrically neutral solution (Schwarzschild, 1999) of Einstein's field equation. A Kerr black hole is a rotating, electrically neutral solution developed by Kerr (1963). The spherically symmetric and non-rotating solution with a non-zero electric charge is called Reissner-Nordström black holes.

With the discovery of the X-ray emitting source Cyg X−1 by Bolton (1971, 1972), the first plausible proof of a stellar-mass black hole's existence was established. Later, numerous black hole candidates associated with astrophysical sources were reported. When massive stars collapse to form BHs, the resulting *spacetime* will generally be Kerr in nature (Pretorius, 2005). It can be either co-rotating or counter-rotating based on whether the direction of the angular momentum of the orbiting particle is parallel or anti-parallel to the BH spin. For such a huge and massive entity, the electric charge is extremely small and can be neglected (Bambi et al., 2009). Thus the Astrophysical BHs are characterized by their mass M and dimensionless *spin parameter*, $a_* = Jc/GM^2$, where c is the speed of light, and G is the Gravitational constant. For a non-rotating BH, $a_* = 0$ and the limiting value for the spin of a maximally rotating BH is a_* =0.998 (Thorne, 1974). In the case of a BH, an *innermost stable circular orbit* (ISCO) exists beyond which particles cannot sustain its Keplerian orbit. The radius of ISCO is a function of the mass and spin parameter given by

(Bardeen et al., 1972)

$$r_{ISCO} = \left[3 + Z_2 - \sqrt{(3 - Z_1)(3 + Z_1 + 2Z_2)}\right] r_g \tag{1.1}$$

where, $Z_1 = 1 + \sqrt[3]{1 - a_*^2}\left[\sqrt[3]{1 + a_*} + \sqrt[3]{1 - a_*}\right]$, $Z_2 = \sqrt{3a_*^2 + Z_1^2}$ and $r_g \equiv GM/c^2$, is the gravitational radius of the BH. For a Schwarzschild black hole, r_{ISCO} =6 r_g and for an extreme Kerr black hole, r_{ISCO} =1.24 r_g. The study of BHs can be done by analyzing the electromagnetic radiation emitted by the matter from its vicinity via different physical processes.

1.2 X-ray Binaries

The X-ray binary (XRB) system consists of a primary component, which is a compact object such as a BH or NS, and a secondary component or companion, which is a normal star. They are generally known as black hole X-ray binaries (BH-XRBs) and neutron star X-ray binaries (NS-XRBs), respectively, based on the nature of the primary compact object. The mass transfer (or accretion of matter) takes place from the companion star to the compact object due to its strong gravity. The accreted matter becomes dense and hot near the compact object. It radiates predominantly in X-rays as a result of extracting the gravitational potential energy of the accreted matter. A white dwarf binary system, known as Cataclysmic Variables (CVs) mostly emits optical and UV radiation, while also consistently being observed to emit soft and hard X-rays. However, CVs exhibit significantly lower X-ray emissions compared to NS-XRBs and BH-XRBs.

The XRBs can be categorized based on the mass of the companion star. If it is a low-mass ($M \leq 1M_\odot$), K−M spectral type star, the system is called a low-mass X-ray binary (LMXB). The XRBs such as Sco X-1 (Mirabel & Rodrigues, 2003), GRO J1655−40 (Mirabel et al., 2002), and GRS 1915−102 (Castro-Tirado et al., 1994; Deegan et al., 2009) fall into this category. On the other hand, a massive ($M \geq 10M_\odot$), early type, O-B star serves as the companion in a high-mass X-ray binary (HMXB). A few examples of this category are Vela X-1 (Grinberg et al., 2017; Kretschmar et al., 2019b), Cyg X-1 Deka et al. (2021), XTE J0421+560 (Robinson et al., 2002), etc. The modes of accretion are different in these two classes of XRBs and are discussed in successive sections.

1.3 Accretion onto Compact Objects

The extraction of gravitational energy through the accretion of matter appears to be the most efficient method for powering the most luminous celestial objects in the universe, such as XRBs, active galactic nuclei (AGNs) and quasars. The gravitational potential energy that is released when a mass m accretes onto a compact object with mass M and radius R is

$$E_{acc} = \frac{GMm}{2R}. \tag{1.2}$$

This can be written in terms of the fraction of gravitational potential energy converted to radiation (η, the radiative efficiency of accretion) as $E_{acc} = \eta\, mc^2$. The dimensionless efficiency is defined as $\eta = GM/2Rc^2$. The higher the compactness (M/R), more is the efficiency of energy release. Since BHs don't have a hard surface, the value of R in Equation 1.2 can be taken as r_{ISCO} (Equation 1.1) and therefore, η for BHs depend on both compactness and spin. The value of η for accretion onto WD, NS, and BH are 0.001, 0.03 and $0.06 - 0.42$, respectively (Frank et al., 1992). Therefore, the efficiency of accretion onto NS and BH is much higher than that of non-gravitational processes, such as the nuclear fusion reaction in a star that occurs during the hydrogen burning, where $\eta = 0.007$. However, the accretion efficiency of WDs is lower than the nuclear efficiency. The observed accretion luminosity $L = \eta \dot{M} c^2$, where $\dot{M} = dM/dt$ is the accretion rate. Higher the rate of accretion, the higher the emitted luminosity of the system.

For a steady and spherically symmetrical accretion, one can define the highest limit on the accretion luminosity, known as the Eddington luminosity (L_{Edd}). We assume the accreting material is fully ionized hydrogen. The outward radiation mainly interacts with the electrons in the in-falling matter via scattering. The force due to radiation on an electron at a radial distance r is $F_{out} = \sigma_T L/4\pi r^2 c$, where σ_T is the Thomson scattering cross-section. The protons will also feel the same force via Coulomb coupling between electrons and protons. The inward gravitational force on the protons in the in-falling matter is $F_{in} = GMm_p/r^2$, where m_p is the mass of a proton. These two forces balance at a critical luminosity (L_{Edd}) and is given by,

$$L_{Edd} = \frac{4\pi GMm_p c}{\sigma_T} = 1.265 \times 10^{38} \left(\frac{M}{M_\odot}\right) \text{ergs s}^{-1} \tag{1.3}$$

When $L > L_{Edd}$, the radiation pressure prevents the matter from getting accreted. Corresponding to this critical luminosity, there exists a limit for the accretion rate also, which is

called the Eddington accretion rate, $\dot{M}_{Edd} = L_{Edd}/\eta c^2$. As we mentioned before, this is applicable only for spherically symmetric accretion. However, the accretion luminosity can be super-Eddington for other geometries such as disc accretion.

The temperature profile of the system can be estimated from the observed luminosity L. An object of characteristic size R emits a blackbody spectrum at a temperature T_{bb} given by,

$$T_{bb} = \left(\frac{L}{4\pi R^2 \sigma}\right)^{1/4}, \tag{1.4}$$

where σ is the Stefan-Boltzmann constant. The maximum possible temperature of a plasma called the *thermal temperature* (T_{th}), can be estimated by equating the potential energy, $GM(m_p + m_e)/R \approx GMm_p/R$, of the particles with its thermal energy ($2 \times 3k_BT/2$):

$$T_{th} = \frac{GMm_p}{3k_BR}, \tag{1.5}$$

where k_B is Boltzmann constant, m_p and m_e are the mass of proton and electron respectively. There may arise two limiting situations for XRBs; the accretion flow can be optically thick or optically thin. In the first case, the radiation comes into thermal equilibrium with the accretion flow before escaping from the system, and the emitted spectrum will be a blackbody. Hence the temperature, T_{emit} of the emitted radiation will be approximately equal to the blackbody temperature of the system ($T_{emit} \approx T_{bb}$). In the second case, the radiation will escape immediately from the optically thin accretion flow once it is produced; therefore, $T_{emit} \approx T_{th}$. In practical terms, the temperature of the emitted radiation typically falls between these two limits, $T_{bb} \lesssim T_{emit} \lesssim T_{th}$. All these estimations are under the assumption of a single temperature for the accretion flow.

1.4 Types of Accretion

Various models have been proposed in the literature for how a compact object can accrete matter from the companion star or the surrounding medium. The most common among them are the accretion through Roche lobe overflow and stellar wind (spherically symmetric accretion) from the companion. It is generally observed that the HMXBs are fed by wind accretion and LMXBs are by Roche lobe overflow, although the realistic accretion scenario may be very complex (Chaty, 2011; Kretschmar et al., 2019a).

1.4.1 Spherically Symmetric Accretion

The idea of accretion onto a point mass moving through a uniform infinite medium having a supersonic flow of uniform velocity was established through the classical solutions developed by Hoyle & Lyttleton (1939) and Bondi & Hoyle (1944) (Bondi-Hoyle-Lyttleton (BHL) accretion). According to the BHL accretion scenario, an overdense accretion column exists behind the star, through which matter passes as streamlines and within a certain radius around the accretor. In this scenario, the relative motion of the star and the gas cloud control the accretion rate. The effect of pressure was ignored in this picture. While it is hard to believe that the pressure of the interstellar medium is zero, no matter how far it is from the star. Bondi (1952) put forward a more realistic picture of the accretion scenario, where he assumed the pressure and the sound speed at infinity are not zero. It depicts a spherically symmetric accretion onto a non-magnetic star, where the gravitating matter is highly radially symmetric and has negligible angular momentum.

Consider a star of mass M at rest with respect to the surrounding medium. The pressure and density at infinity are given by P_∞ and ρ_∞ respectively. Consider spherical polar coordinates (r, θ, ϕ) with the star at its origin. Only the radial component, $V(r)$ of velocity (V) of the surrounding gas comes into the picture. For the accretion process, $V(r) < 0$ implies that the gas is being pulled towards the star by its gravitational field, while $V(r) > 0$, implies a stellar wind blowing away from the star's surface. The steady-state continuity equation is in the form,

$$\frac{1}{r^2}\frac{d}{dr}(r^2\rho V) = 0, \tag{1.6}$$

where ρ is the mass density. Integration of this equation gives rise to the steady mass accretion rate, i.e., in-fall rate $(\dot{M})$ of the material, to the star:

$$\dot{M} = 4\pi r^2 \rho(r) V(r). \tag{1.7}$$

In the steady state, the Euler equation becomes

$$V\frac{dV}{dr} + \frac{1}{\rho}\frac{dP}{dr} + \frac{GM}{r^2} = 0, \tag{1.8}$$

where P is the pressure. To solve Equation 1.8, we assume a polytropic equation of state: where the pressure $P = K\rho^\gamma$; γ is the adiabatic index and K is the proportionality constant. For isothermal gas, $\gamma = 1$ and for non-relativistic adiabatic accretion, $\gamma = \frac{5}{3}$. Now the

Equation 1.8 can be rearranged as

$$\frac{1}{2}\left(1-\frac{c_s^2}{V^2}\right)\frac{d(V^2)}{dr} = -\frac{GM}{r^2}\left(1-\frac{2c_s^2 r}{GM}\right) \tag{1.9}$$

where $c_s = \sqrt{dP/d\rho}$ is the sound speed. The term on the right-hand side of Equation1.9

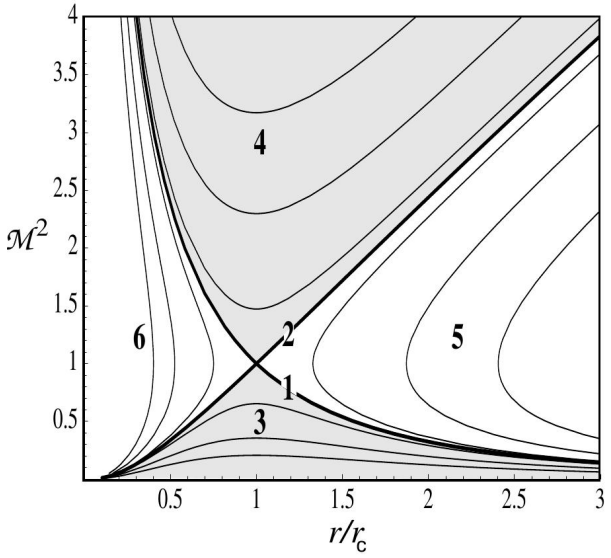

Figure 1.1: The six classes of solutions of the Equation 1.9 in terms of $V^2(r)/c_s^2(r)$ versus r/r_c. The two transonic solutions are marked with 1 (accretion) and 2 (wind), and the unphysical solutions are marked with 3−6. Credit: Frank et al. (1992)

becomes positive at a larger distance ($r \to \infty$) from the star. While on the left hand side, $V \to 0$ as $r \to \infty$ and $d(V^2)/dr$ must be negative. This suggests a subsonic ($V^2 < c_s^2$) flow far from the star. As the flow approaches the star ($r \to 0$), the right-hand side becomes negative and $c_s^2/V^2 < 1$, i.e., flow is supersonic ($V^2 > c_s^2$) close to the star. At the *sonic point*, $r_c = GM/2c_s^2$, the flow speed is equal to the speed of sound, $V^2(r_c) = c_s^2(r_c)$. The solutions that pass through a sonic point are called *transonic* flows.

All the solutions of the Equation 1.9 are plotted as $\mathcal{M}^2 = V^2(r)/c_s^2(r)$ versus r/r_c in Fig. 1.1, where $\mathcal{M}$ is the mach number. The accretion process is identified by a flow that starts subsonic at a greater radius and transitions to supersonic near the star (marked as 1 in Fig. 1.1). The other transonic solution of Equation 1.9, where the flow is subsonic close to the star and becomes supersonic at $r > r_c$, is the wind solution (marked as 2 in Fig. 1.1). The remaining four solutions (marked as 3−6 in Fig. 1.1) of Equation 1.9 are unphysical.

We can obtain the accretion rate in terms of the physical conditions at infinity by integrating Equation 1.8 and using the polytropic relation and Equation 1.7. The sound

speed at the sonic point is given by, $c_s(r_c) = c_s(\infty)\sqrt{\frac{2}{5-3\gamma}}$, where $c_s(\infty)$ is the sound speed at infinity. For a typical interstellar medium parameters at infinity: $\rho_\infty \approx 10^{-24}$ g cm^{-3}, $c_s(\infty) \approx 10$ km s^{-1}, and temperature $T_\infty \approx 10^4$ K, the rate of accretion will be,

$$\dot{M} \approx 1.4 \times 10^{11} \left(\frac{M}{M_\odot}\right)^2 \left(\frac{\rho_\infty}{10^{-24}\text{g cm}^{-3}}\right) \left(\frac{c_s(\infty)}{10 \text{ km s}^{-1}}\right)^{-3} \text{ g s}^{-1}. \tag{1.10}$$

Therefore, the accretion luminosity for a typical solar mass star, $L_{acc} = GM\dot{M}/2R \approx 2 \times 10^{31}$ ergs s^{-1}, is much lower than the luminosity generally observed in XRBs. The spherical accretion is radiatively inefficient because the matter does not have enough time to radiate before falling onto the central object due to the high radial infall speed. The accretion through a disc (discussed below) gained popularity to overcome the shortfall of spherical accretion.

1.4.2 Accretion through Disc: Standard Disc Model

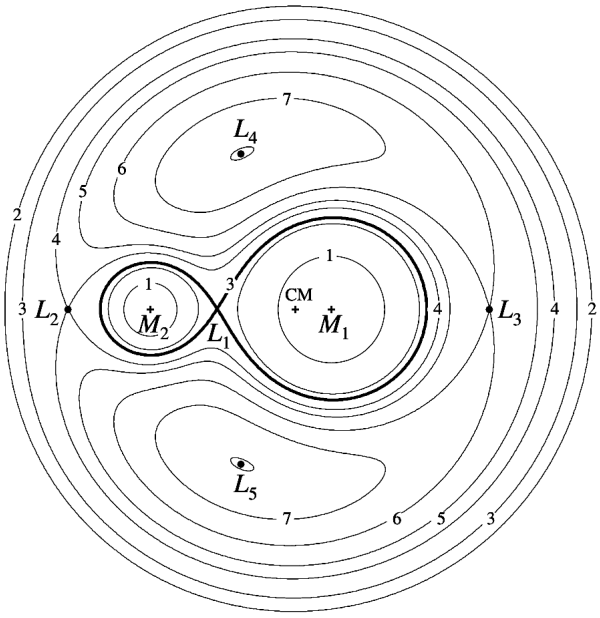

Figure 1.2: The equipotential surfaces of $\Phi_R(\mathbf{r})$ for a binary system with mass ratio q= $M_2/M_1 = 0.25$. The system has five Lagrange points ($L_1 - L_5$). Materials can pass between the dumbbell-shaped Roche lobes through L_1. Credit: Frank et al. (1992)

Edouard Roche was the first to study the possibility of mass transfer in binary systems. He considered a test mass in the gravitational potential of two point masses (M_1 and M_2) orbiting around their common centre of mass (CM). The angular speed of the binary system

is given by $\Omega = \sqrt{GM/a^3}$, where $M = M_1 + M_2$ and 'a' is the binary separation. The potential (called the Roche potential), Φ_R, experienced by the test mass at a distance $\mathbf{r}$ is (Frank et al., 1992)

$$\Phi_R(\mathbf{r}) = -\frac{GM_1}{|\,\mathbf{r}-\mathbf{r}_1\,|} - \frac{GM_2}{|\,\mathbf{r}-\mathbf{r}_2\,|} - \frac{1}{2}(\mathbf{\Omega}\times\mathbf{r})^2, \tag{1.11}$$

where, $\mathbf{r}_1$ and $\mathbf{r}_2$ are the position vectors of the two masses. The equipotential surfaces of $\Phi_R(\mathbf{r})$ are plotted in Fig. 1.2. The shape of the equipotential surfaces is governed by the mass ratio, q$\equiv M_2/M_1$. However, their qualitative characteristics are universal. For a test particle at a large distance ($r \gg$ a), the system appears as a point mass centred at the CM. At the close vicinity of both stars, the equipotentials are circular, and the test particle suffers strong gravitational pull. A figure-of-eight surface connects these two deep potential wells, which appear as lobes (*Roche lobes*) in three-dimension. There are five Lagrange points where the test mass does not experience any force. In a compact binary system, if the companion star can fill the Roche lobe, its material can transfer to the Roche lobe of the primary through L_1. This type of mass transfer in binaries is called Roche lobe overflow. This is possibly the mechanism of mass transfer seen in LMXBs in general.

As a consequence of the Roche lobe overflow, the material can't directly land on the surface of the accretor since it possesses high angular momentum. It acts like a nozzle that rotates fast, and the materials are ejected at supersonic speeds. Therefore, the material initially be distributed around the primary in an elliptical orbit in the binary plane. It will interact with the further inflow of matter, dissipating energy via shocks and trying to circularise the orbit having the lowest energy. The specific angular momentum in a Keplerian orbit is a function of the distance r from the accretor, i.e., neighbouring radii are in differential rotations. Due to collision, turbulence, and magnetic field, the local viscous torque transfers the angular momentum outward, allowing the matter to move radially inward, eventually forming an accretion disc around the primary.

The study of disc accretion started with the pioneering work of Lynden-Bell (1969) and Pringle & Rees (1972, and reference therein). Shakura & Sunyaev (1973) provided a breakthrough in the development of the accretion disc theory known as *the Standard Accretion Disc Model* or α - *disc model*. This model describes a geometrically thin, $H/r \ll 1$, (where H is the half thickness of the disc in the vertical direction at a radial distance r), non-self gravitating (disc mass is much smaller than that of the central object), steady disc having a turbulent flow. This model encapsulates all the micro-physics of the flow through a dimensionless constant, $\alpha \lesssim 1$, and expresses the kinematic viscosity as

$\nu_k \equiv \alpha c_s H$. Let us use cylindrical polar coordinates (r, ϕ, z) to describe the dynamics of a thin Keplerian disc. The accreting star has a mass M and radius R, and the matter moves around it in Keplerian orbits. The mass conservation equation for the disc is given by (Frank et al., 1992),

$$\frac{\partial \Sigma}{\partial t} + \frac{1}{r}\frac{\partial}{\partial r}(r\Sigma V_r) = 0, \tag{1.12}$$

where $\Sigma(r, t)$ is the vertically integrated surface density of the disc at a time t and V_r is the radial drift velocity of the material (Frank et al., 1992),

$$V_r = -\frac{3}{\Sigma\sqrt{r}}\frac{\partial}{\partial r}\left(\nu_k \Sigma\sqrt{r}\right). \tag{1.13}$$

The time evolution of surface density is given by

$$\frac{\partial \Sigma}{\partial t} = \frac{3}{r}\frac{\partial}{\partial r}\left[\sqrt{r}\frac{\partial}{\partial r}\left(\nu_k \Sigma\sqrt{r}\right)\right]. \tag{1.14}$$

A ring of matter at a radius r spreads out due to the effect of viscosity on a timescale, known as *viscous* or *radial drift timescale*, $t_{vis} = r^2/\nu_k$. For rather longer timescales, the disc is assumed as steady and the conserved mass accretion rate through every point r in the disc is given by,

$$\dot{M} = 2\pi r \Sigma(-V_r), \tag{1.15}$$

with $V_r < 0$. For a steady-state disc, the local viscous energy dissipation per unit disc area is (Frank et al., 1992)

$$D(r) = \frac{3GM\dot{M}}{8\pi r^3}\left[1 - \sqrt{\frac{R}{r}}\right]. \tag{1.16}$$

The disc is assumed to be optically thick in the z direction; therefore, the radiation emitted will have a local blackbody spectrum. The viscous energy dissipated per unit area can be equated to the blackbody emission flux to define the temperature of the disc,

$$T(r) = \left[\frac{3GM\dot{M}}{8\pi\sigma r^3}\left(1 - \sqrt{\frac{R}{r}}\right)\right]^{1/4}. \tag{1.17}$$

The blackbody intensity at a frequency ν emitted from each radius is given by the Planck function,

$$B_\nu(r) = \frac{2h\nu^3}{c^2}\frac{1}{e^{\frac{h\nu}{k_B T(r)}} - 1}, \tag{1.18}$$

where h is the Planck constant. The accretion disc spectrum (Fig. 1.3) can be regarded

as a superposition of blackbody spectra emitted from different annuli of the disc. This is called a "multicolour disc blackbody" spectrum. The outer regions of the disc with a lower temperature contributes to the Rayleigh-Jeans regime ($\propto \nu^2$). While the hot, innermost regions of the disc produces the Wien regime. The middle part ($\propto \nu^{1/3}$) is the modified blackbody due to the combined effect of local emission and the area of the emitting region.

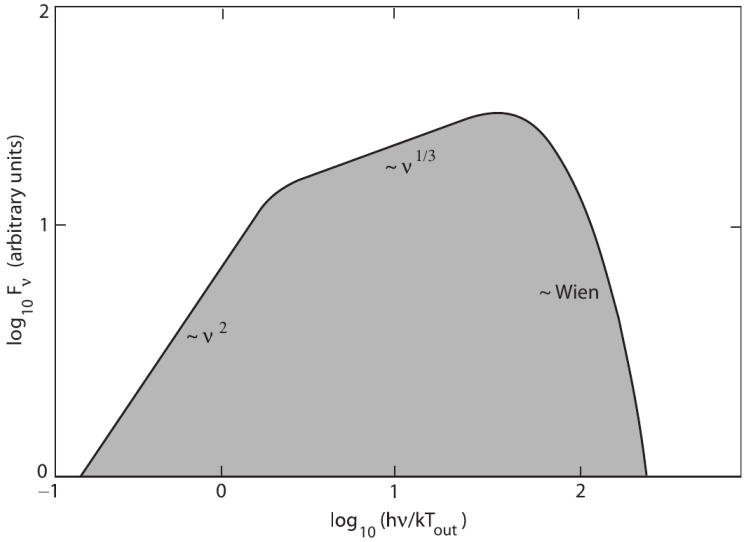

Figure 1.3: The spectrum of an accretion disc as a superposition of the blackbody spectra emitted from various annuli of the disc. The low-temperature disc (outer part) produces the low-frequency regime, while the hot (inner) region produces the high-frequency Wien regime. Credit: Melia (2009)

The Standard Disc Model successfully explains the optical-ultraviolet emission of dwarf novae, AGNs, and soft X-ray emission from XRBs. However, the observed spectrum at high-energy differs significantly from a blackbody, showing a non-thermal (powerlaw) nature with an occasional high-energy cut-off at around 80−300 keV (Sunyaev & Truemper, 1979).

Various accretion disc models were developed during the early nineties to understand the origin of high-energy emissions from XRBs. A standard accretion disc model assumes that the locally dissipated energy is radiated away from the disc efficiently since the model neglects the contribution of the advection term (VdV/dr) in the hydrodynamic equations. If a significant amount of heat is advected into the accretor, accretion flow is radiatively inefficient Begelman & Meier (1982); Abramowicz et al. (1988). The standard disc model fails to describe two regimes: (*i*) hot, optically thin, low accretion rate flows and (*ii*) optically thick flows with high luminosity and high accretion rate. Advection is the dominant cooling mechanism in both cases since the radiative cooling time is larger than the time for radial

infall towards the accretor. Here optically thin case-(*i*) is called Advection Dominated Accretion Flows (ADAF) (Narayan & Yi, 1994, 1995a,b) and the optically thick case-(*ii*) is called *slim disc* (Abramowicz et al., 1988). The slim discs are geometrically neither too thin nor too thick ($H/r \lesssim 1$), whereas the ADAF possesses a geometrically thick disc $H/r \sim 1$. In a geometrically *thick disc*, the inner region of the accretion disc 'puffs up', and the angular momentum involved is sub-Keplerian in nature. Both ADAF and slim disc solutions were self-similar. However, Chakrabarti and collaborators (Chakrabarti, 1990, 1996, 1997, and references therein) developed self-consistent transonic solutions for advective accretion flow having sub-Keplerian angular momentum.

The XRBs are classified into two, persistent and transient/outbursting sources. The persistent sources are always bright due to continuous accretion at a higher rate throughout their life. However, the transient sources exhibit *outbursts* (luminous phase) followed by an inactive period called *quiescence*. Further, we discuss the possible physical picture behind the outburst events, which is the subject of the current study.

1.5 Disc Instabilities and Outbursts

Even though steady disc solutions provide great insights into the behaviour of the accreting systems, a steady disc is far from reality. Instabilities triggered by small perturbations can disturb the equilibrium of these systems. Instabilities are associated with various timescales that appear in the accretion disc theory. The timescale needed to re-adjust the thermal equilibrium of the system is called the *thermal timescale*, t_{th} and the disc dynamics is governed by the *dynamical timescale*, t_{dyn}. The radial drift of matter is governed by the *viscous timescale*, t_{vis}. These timescales are related by the following relation (Pringle, 1981; Frank et al., 1992),

$$t_{dyn} \approx \alpha t_{th} \approx \alpha \left(\frac{H}{r}\right)^2 t_{vis}. \tag{1.19}$$

Therefore, $t_{dyn} \lesssim t_{th} \ll t_{vis}$ since $\alpha \lesssim 1$. The viscous timescale is typically on the order of days to weeks for XRBs, whereas the other two are on the order of minutes.

In the standard disc paradigm, two types of instabilities, thermal and viscous instability, are of prime importance. Thermal instability occurs if an imbalance exists between the local cooling rate (Q^-) and the heating rate (Q^+). For a system in equilibrium ($Q^+ = Q^-$), heating and cooling rates are enhanced if the local temperature increased by a small perturbation. However, a faster heating rate leads to an imbalance that grows over time. This happens over the timescale of t_{th} and is called thermal instability. Similarly, changes in the disc

structure due to external factors, for example, variations in the mass accretion rate, can lead to perturbation in the surface density of the disc. The dynamic viscosity, $\mu = \nu_k \Sigma$, leads to an imbalance, $\delta\mu$. If $\partial\mu/\partial\Sigma > 0$, we arrive at a situation governed by Equation 1.14. While if $\partial\mu/\partial\Sigma < 0$, the disc's denser regions will fill up with more matter, and its less dense regions will be cleared of matter. Eventually, the disc will break up into fragments of rings. This happens over the timescale of t_{vis} and is called viscous instability. These

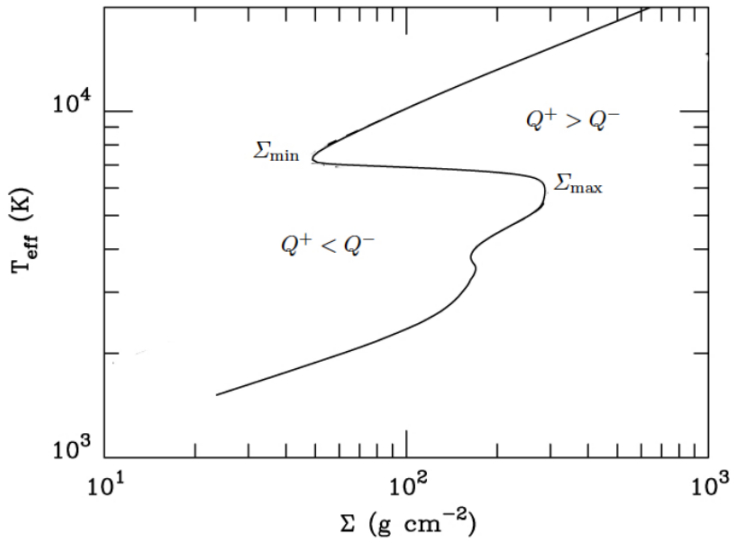

Figure 1.4: Surface density (Σ) vs effective temperature ($T_{\rm eff}$) plot representing local thermal equilibrium characteristics of accretion discs. See text for details. Credit: Lasota (2016)

instabilities are generally believed to be the reason for the outbursts in dwarf novae and soft X-ray transients. The former refers to binary systems with WDs, while the latter refers to systems containing BHs and NSs.

Osaki (1974) introduced the disc instability model (DIM) to explain the outburst triggering in dwarf novae. The DIM assumes a geometrically thin Keplerian accretion disc made of hydrogen. The viscosity is described by the α prescription. An outburst is caused by thermal instability developed in the disc when the local temperature of the disc is of the order of the hydrogen ionization temperature. The thermal equilibrium can be characterized by $T_{\rm eff}(\Sigma)$ or $\dot{M}(\Sigma)$ relation, where $T_{\rm eff}$ is the effective temperature of the disc. Fig. 1.4 represents the thermal equilibrium characteristics of a ring at 10^9 cm in an accretion disc around a WD of mass 1.2 $M_\odot$ using the $\Sigma - T_{\rm eff}$ plot. The solid 'S-curve' represents the thermal equilibrium ($Q^+ = Q^-$) in the figure. Σ_{min} and Σ_{max} indicate the minimum surface density for a hot stable equilibrium and the maximum surface density for a cold stable equilibrium, respec-

tively. Corresponding to Σ_{min} and Σ_{max} there exist two critical accretion rates $\dot{M}^{+}_{crit}(r)$ and $\dot{M}^{-}_{crit}(r)$ respectively. A disc is stable if the rate at which mass is transferred to its outer edge is larger than the $\dot{M}^{+}_{crit}$ at this radius. Cooling dominates the heating ($Q^{+} < Q^{-}$) on the left of the 'S-curve' where hydrogen is neutral. In contrast, heating dominates ($Q^{+} > Q^{-}$) on the right side, where hydrogen is fully ionized. More clearly, the curve's positive slope (upper hot and lower cold branches) represents stable solutions, whereas a negative slope (middle branch) represents instabilities. An annulus moves through the S-curve in viscous timescales and through the non-equilibrium paths in thermal timescale. This means that the surface density in the cold stable state must be lower than Σ_{max}, whereas the surface density in the hot stable state must be larger than Σ_{min}. Once Σ exceeds Σ_{max} at some radius, the disc transits to a hot state and an outburst is triggered. The high surface density and temperature cause the matter and heat to diffuse to the nearby annuli, thus propagating the heating fronts inward and outward around the annulus of instability. An outburst ends when $\Sigma < \Sigma_{min}$. The hot branch in the S-curve corresponds to the outburst maximum and the subsequent decay, while the cold band corresponds to quiescence. During quiescence, the Σ, temperature, and the accretion rate at every annulus are on the cold branch. The hot branch has more viscosity than the cold branch, hence the duration of the quiescence is much larger than the outburst duration (Lasota, 2016). The nature of the outburst depends on $\dot{M}$ from the companion star. If $\dot{M}$ is low, the viscosity gets enough time to affect the matter distribution significantly, and Σ exceeds Σ_{max} near the inner part of the disc. Such outbursts start at the inner part of the disc and propagate outside (*inside-out*). For a higher $\dot{M}$, matter gets less time to spread as the viscous timescale is larger. The condition ($\Sigma > \Sigma_{max}$) for outbursts is met at the outer edge of the disc, which causes the outburst to start and propagate inside (*outside-in*). The interval between outbursts is long in inside-out propagation, while outbursts are more frequent in outside-in propagation.

The DIM proposed for the dwarf-novae outburst is not a general model for thermal-viscous outbursts. Due to the large outburst duration, it cannot directly apply to XRBs. The major modification of DIM proposed for soft X-ray transients is the X-ray irradiation of the outer disc (van Paradijs, 1996). The irradiation increases the effective temperature of the disc. As a result, the hydrogen becomes fully ionized, and the disc remains in the hotter branch of the S-curve for a longer duration. When the effect of irradiation is taken into account, the critical accretion rate which separates transient and persistent systems agrees well with the model (Coriat et al., 2012). For transient XRBs, disc truncation must be considered in addition to the irradiation to modify the DIM (Menou et al., 2000).

1.6 Spectral and Timing Variability in BH-XRB: State Classification

Transient XRB systems exhibit repeated outbursts and quiescent states. The outbursting sources are the best targets to understand accretion physics. As XRBs exhibit significant spectral and temporal variations due to the complexity of accretion dynamics, spectro-temporal analysis opens up a window to study their behaviour.

1.6.1 Spectral Variability

The observed spectra of BH-XRBs consist of two distinct components; soft (low-energy X-ray) and hard (high-energy X-ray), respectively. In addition to the multicolour blackbody emission from the optically thick Keplerian disc, the non-thermal processes like Comptonization (Sunyaev & Truemper, 1979; Sunyaev & Titarchuk, 1980) in the optically thin media also contribute to the X-ray spectra. The soft component is believed to be originated from the optically thick disc. The comptonization of these soft photons by the hot electrons in the optically thin 'corona' efficiently radiates in the hard X-ray. The geometry of the corona has not been established, but several possible geometries are discussed in the literature; sandwich-corona (Haardt & Maraschi, 1991, 1993), slab-corona (Malzac et al., 2005), patchy-corona above the accretion disc (Galeev et al., 1979; Stern et al., 1995; Svensson, 1996) etc. A fraction of the Comptonized radiation may intercept the disc, increasing the disc temperature which further enhances the soft photon flux to the Comptonization region. As a result, the cooling rate will increase; consequently, the electron temperature ($k_B T_{\rm e}$) in the Comptonization region will decrease, leading to softer (steeper index) spectra. Given the typical accretion disc temperature, it is assumed that the hydrogen and helium are fully ionized and the heavy elements are neutral. The intercepted radiation may undergo Comptonization by free electrons of hydrogen and helium, and the dissipated heat will be absorbed by the heavy elements (photoabsorption), contributing to its energy balance. The rest of the energy will be reflected due to Compton scattering. A fraction of the photoabsorbed radiation will be re-emitted from the disc in the form of fluorescent lines of heavy elements. The combined effects of photoabsorption, Compton scattering, and fluorescence produce the *reflected spectrum*. It consists of fluorescent lines and K-edges of different elements superimposed on the broad *Compton hump* peaks at 20−50 keV (Basko et al., 1974; Lightman & White, 1988; George & Fabian, 1991). Fig. 1.5 shows the major components of the X-ray spectrum from an accreting BH (top) and a representation of the conceivable geometry of

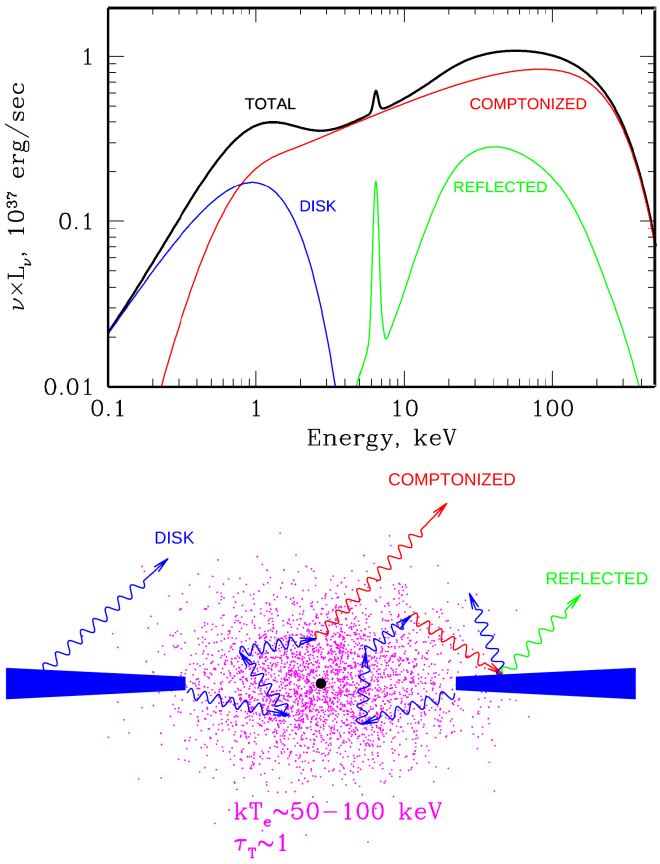

Figure 1.5: The major components of the X-ray spectrum from an accreting BH (top). Corresponding plausible geometry of the system with an accretion disc and a corona that fills the space between the disc and the horizon (bottom). Credit: Gilfanov (2010)

the system with a corona that fills the inner regions of the accretion disc around the BH (bottom). Physical changes in the disc-corona geometry, accretion rate, etc., can lead to spectral variability. Several models have been proposed to include these spectral features, which will be discussed in §2.3.1.

1.6.2 Timing Variability

In addition to spectral variability, BH-XRBs also possess variability in their lightcurves. The time series signals from astronomical sources are generally weak. On top of this, various forms of noise are embedded in the lightcurves. Therefore, identifying the true time variability in the lightcurves is extremely challenging. However, in the Fourier domain (frequency), either noise does not contribute or contributes to the known pattern, making it easier to detect variations of the source in different timescales. The root mean square (RMS)

amplitude variation in the flux is quantified by the power density spectrum (PDS). PDS often consists of narrow features superimposed on a broad continuum of aperiodic variability (van der Klis, 1989). Periodic variability is often associated with systems that have hard boundaries, such as Pulsars. In BH-XRB systems, aperiodic variabilities, including quasi-periodic oscillations (QPOs), are frequently observed. QPOs are characterized by narrow peaks of concentrated power at certain frequencies (*characteristic frequency*, ν_c). QPOs are classified into two groups based on their frequency range: low-frequency (0.01−30 Hz) QPOs (LFQPO: Remillard et al. (2002)) and high-frequency ($30-10^3$ Hz) QPOs (HFQPO: Morgan et al. (1997)). The LFQPOs are very common in BH-XRBs, which are further classified into type-A, B, and C based on their characteristic frequency, width, power in the PDS, etc. (Miyamoto & Kitamoto, 1991; Takizawa et al., 1997; van der Klis, 2006; Remillard & McClintock, 2006). The most common type of QPO in BH-XRBs is type-C QPOs. Their characteristic frequency, ν_c varies from a few mHz to 10 Hz (Motta, 2016). Occasionally, these QPOs are also detected in the soft state and the ultra-luminous state (ULS), reaching frequencies of $\sim$ 20−30 Hz (Motta et al., 2012). They are identified as having high-amplitude (RMS $\sim$20 %) feature with $\nu_c/\Delta\nu \geq$10 in the PDS (Motta, 2016). Type-B QPOs appear in a small range of frequencies, 1−6 Hz (Motta et al., 2011) and are characterized by relatively weaker (RMS $\sim$5%) broadband noise with $\nu_c/\Delta\nu \geq$6. Type-A is a less common type of QPO in BH-XRBs. They are identified by a very weak amplitude (RMS of a few percent), and broad ($\nu_c/\Delta\nu \leq$3) peak that appears between 6−8 Hz (Motta, 2016).

There are several studies in the literature to understand the origin of LFQPOs. Molteni et al. (1996); Chakrabarti et al. (2008) proposed that LFQPOs originated from the resonance between cooling and infall time in the *propagating oscillatory shock* model. Stella & Vietri (1998) introduced a *relativistic precession* model where nodal precession can explain type-C QPOs. Tagger & Pellat (1999) proposed an *accretion ejection instability* model where spiral density wave instability is responsible for LFQPOs.

Detection of a 67 Hz QPO in GRS 1915+105 is the first HFQPO in BH-XRBs (Morgan et al., 1997). In the literature, only a limited number of high-frequency quasi-periodic oscillation (HFQPO) detection, fewer than ten, have been reported for BH-XRBs (Belloni et al., 2012; Ingram & Motta, 2019). HFQPOs are assumed to be emitted from the innermost regions of the accretion disc, and therefore, they carry imprints of the effects of strong gravity. In the relativistic precession model (*Lense-Thirring precession*), the lower and upper HFQPOs are linked to the periastron precession and the orbital frequency (Stella & Vietri, 1998). However, Abramowicz & Kluźniak (2001) proposed that the HFQPO pair

can be addressed due to the resonance related to general relativistic frequencies for three spatial coordinates.

1.6.3 State Classification

Based on the characteristics of the X-ray spectrum and the PDS, various "states" have been identified for outbursting BH-XRBs (Homan & Belloni, 2005; Remillard & McClintock, 2006; McClintock & Remillard, 2006). The major criteria used for identification include the relative contribution of thermal and non-thermal radiations, the photon (or spectral) index Γ, total RMS variability in the PDS (over $0.1-10$ Hz), and QPO properties. The four states are low/hard state (LHS), hard intermediate state (HIMS), soft intermediate state (SIMS) and high/soft state (HSS). The intermediate states fall between LHS and HSS states.

The LHS is typically observed at the start and end stages of an outburst. This state is characterized by a hard spectrum with a spectral index of $\sim$1.7. The non-thermal component dominates (>80%) over the thermal component. High timing variability is a characteristic of this state with an RMS variability $\gtrsim$20%. PDS consists of broadband (flat-top) noise and type-C QPOs. Also, the frequency of the QPO increases with the source flux. Compact-steady radio jets are observed during this state. Also, a strong positive correlation exists between X-ray and radio flux in this state. The source enters the HIMS after leaving the initial LHS and before entering the final LHS. In the HIMS, the spectrum appears softer due to the increase of the thermal component from the disc, and hence the spectral index steepens ($2.4-2.5$). Similar to the LHS, type-C QPOs are present during this state, and the characteristic frequency of QPOs evolves with time. The total fractional RMS variability drops to $10-20$% with spectral softening. In the SIMS, the spectrum appears slightly softer than in the HIMS, and it does not show a significant high-energy cut-off, unlike the HIMS. The PDS no longer contains a band-limited noise component and is instead dominated by a powerlaw component. SIMS possess type-A or/and type-B QPOs and are less common (Belloni et al., 2005). Occasional relativistic jets (radio flare) are observed in this state. When the source transitions to HSS, the thermal disc component dominates the spectrum (>75%). The source appears brighter in this state, and the spectrum has a spectral index $\sim$3. Total fractional RMS variability is very low ($\lesssim$1%) during this state. PDS is almost featureless, and QPOs are absent in this state. The radio emission from the source completely stops during the HSS. Instead, wind outflows are often observed. Remillard & McClintock (2006) introduced one more state known as a steep powerlaw state (SPL), which is characterized by strong flaring at high-luminosity on a timescale of days. This

state is generally observed before the source enters the HSS. In the SPL state, the powerlaw component dominates ($> 80\%$), with a spectral index, $\Gamma \sim 2.4 - 3.0$. Timing properties reveal very low ($< 0.1\%$) fractional RMS and QPOs are observed in the PDS.

Transient systems spend most of their time in the quiescent state, where they have very low X-ray luminosity ($<10^{33}$ ergs/s) and a non-thermal hard spectrum (low-luminosity version of LHS). During a typical outburst, the following sequence of state transitions occurs in BH-XRBs: LHS $\rightarrow$ HIMS $\rightarrow$ SIMS $\rightarrow$ HSS $\rightarrow$ SIMS $\rightarrow$ HIMS $\rightarrow$ LHS. However, the intermediate states are short-lived and are not always observed. The outburst in which the system transitions from the LHS to the HSS is called a 'successful' outburst; while the outburst in which the system fails to make a transition to the HSS is called a 'failed-transition' outburst (Debnath et al., 2015; Radhika et al., 2016; García et al., 2019; Baby et al., 2020, 2021; Prabhakar et al., 2022).

The outburst nature varies among binary systems, and even different outbursts of the same system exhibit distinct evolutionary trends (Aneesha et al., 2019; Aneesha & Mandal, 2020). However, the outbursts of these systems show some universal behaviour (Homan & Belloni, 2005). One way of identifying the universal spectral behaviour of these systems

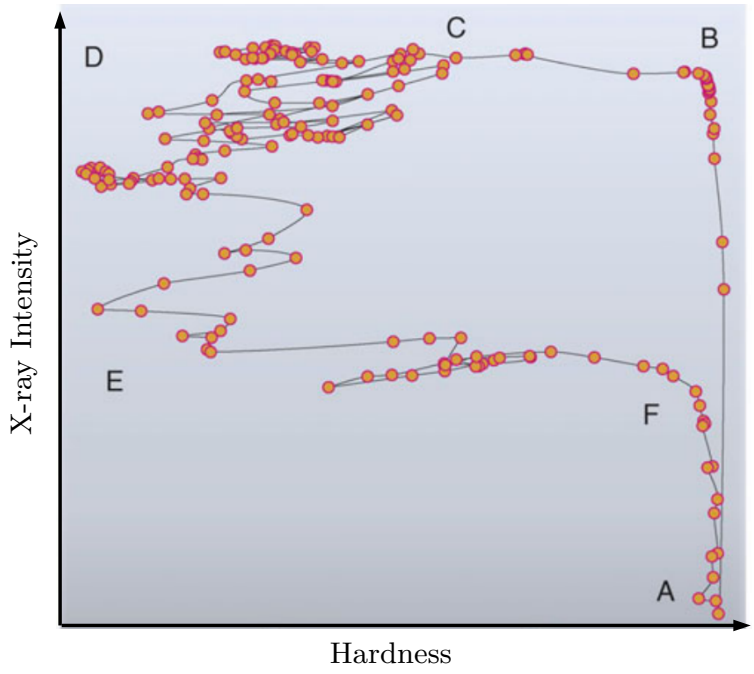

Figure 1.6: Sketch of the hardness-intensity diagram of a transient BH-XRB. The evolution of the outburst is indicated from A through F. Credit: Bambi (2016)

is by generating a hardness-intensity diagram (HID), that displays X-ray intensity versus

hardness. Here, the *hardness* or *hardness ratio* (HR) is the ratio of observed flux in a higher energy band to a lower energy band. A typical HID (Fig. 1.6) forms a 'q-shaped' diagram where the source evolves across the spectral states in a counterclockwise direction. The quiescent state is well below point A in Fig. 1.6 with a low-luminosity. The HID's two vertical branches (AB and DE) correspond to the two major states; LHS at the extreme right and HSS at the extreme left. Intermediate states fall on the middle horizontal branches. An outburst starts from the LHS with a high flux at the extreme right of HID, moves to HSS through intermediate states, and returns to the LHS, completing a hysteresis cycle (Miyamoto et al., 1995). The hard-to-soft transition occurs at a higher (by a factor $\gtrsim$5) flux than soft-to-hard transition (Maccarone & Coppi, 2003), which is responsible for the hysteresis behaviour of HID. The HIMS starts at point B, and the transition to SIMS happens during CD. The source appears extremely bright at point D (HSS). Further, the source luminosity gradually decreases (branch DE), and the outburst decay (branch EF) proceeds through the intermediate states.

The global timing behaviour of transients is expressed in the RMS–intensity diagram (RID), which tracks the evolution of the intensity and RMS (Muñoz-Darias et al., 2011; Heil et al., 2012). The hardness–RMS diagram (HRD, Belloni et al., 2005), where the fractional RMS is plotted against the hardness ratio, represents the combined spectro-temporal variation during the outburst.

1.7 Outflow and Disc Wind

Outflows/jets are associated with accretion as they cannot be formed without accretion. Jets are compact radially, whereas outflows are radially extended. The physical processes responsible for the origin of outflows/jets are poorly understood. However, the structured magnetic field in the accretion disc, thermal and radiation pressure in the inner disc, black hole spin, etc. (Blandford & Znajek, 1977; Blandford & Payne, 1982; Kumar et al., 2014; Vyas et al., 2015, and references therein) are thought to be responsible for the production of jets/outflows.

Generally, XRB jets are luminous in radio; however, they emit optical/IR sometimes. The first detection of a superluminal radio jet in our galaxy was reported in GRS 1915+105 (Mirabel & Rodríguez, 1994). The synchrotron radiation from outflowing plasma produces the radio emission in XRBs. The compact radio jets are usually associated with the hard state, and relativistic radio flares are seen during the hard-soft state transition (Fender et al., 2004, 2009). The hard X-ray states are associated with persistent radio flux with flat inverted

spectra ($S_\nu \propto \nu^\alpha$), extending to near IR. There exists a strong positive correlation (Corbel et al., 2003, 2013) between the radio and X-ray luminosity in the hard state. This trend is first observed in GX 339−4 (Corbel et al., 2003) and Cygnus X−1 (Stirling et al., 2001). As the source softens, the radio emission decreases (Gallo et al., 2003). No radio emission has been reported from XRBs during the HSS; disc winds are observed instead (Neilsen & Lee, 2009; Ponti et al., 2012; Neilsen et al., 2014).

Identifying accretion disc winds in XRBs is one of the most important findings made possible by high-resolution X-ray spectroscopy. Accretion disc wind is generally observed in the highly luminous disc-dominated HSS, though it can exist in other spectral states as well (Lee et al., 2002; Miller et al., 2008; Neilsen & Lee, 2009; Neilsen, 2013). Disc winds can remove matter from the accretion disc at a rate of the order of the system's inner accretion rate or higher (Ponti et al., 2012; Kosec et al., 2020). Therefore, it can suppress the launch of jets (Neilsen & Lee, 2009) in the HSS. Also, it may play a crucial role in regulating the accretion dynamics of the system. For example, Muñoz-Darias et al. (2016) showed how winds control the violent outburst of V404 Cygni by diminishing a significant fraction of the outer disc. The presence of disc winds is inferred by the appearance of strong absorption features in the spectra. The high-resolution X-ray spectrum reveals the presence of neutral/highly ionized absorbers in BH-XRBs. The absorption features may reveal the presence of highly ionized iron, such as Fe XXV and Fe XXVI, indicating photoionized plasma. The first detection of absorption lines in the spectra of BH-XRB was done by Ueda et al. (1998). They detected iron K_α and K_β absorption lines in GRO J1655−40 using *ASCA* data. Afterwards, Kotani et al. (2000) and Lee et al. (2002) detected similar features in GRS 1915 + 105. Since then, high-resolution X-ray spectroscopy has revealed that ionized absorbers in the form of disc winds are a common attribute of accreting systems (Parmar et al., 2002; Shidatsu et al., 2013). So far, the ionized absorbers are detected close to their characteristic transition energy (Parmar et al., 2002), inferring the non-relativistic nature of the disc winds. A relativistic nature of the disc wind can be inferred by the blueshifted absorption features in the X-ray spectrum (Ebisawa, 1997; Kotani et al., 1997). In general, absorption lines are absent in the LHS. Neilsen & Lee (2009) suggests that the wind gets photoionized completely in LHS, and the medium becomes transparent. This could be a possible reason for the absence of absorption lines in the LHS spectra. Usually, the disc winds are observed in high-inclination systems (Ponti et al., 2012) due to high column density along the line-of-sight.

1.8 Aim and Source Selection

This thesis investigates the accretion process in extremely bright BH-XRBs in our galaxy using broadband X-ray observations. The XRB sources can appear bright due to proximity, or they can be intrinsically luminous. For this study, we have selected two bright BH-XRBs, MAXI J1820+070 and 4U 1543−47, where MAXI J1820+070 belongs to the category of proximity sources, and 4U 1543−47 is intrinsically luminous. The study includes comprehensive spectral and timing analysis of the sources using data from four different instruments: *Swift/XRT, NICER, NuSTAR* and *AstroSat*.

MAXI J1820+070 is a galactic LMXB, discovered in 2018. It consists of a 'failed-transition' outburst followed by a successful one. It is one of the brightest X-ray transients, having a soft X-ray flux of ~ 4 Crab in $2 - 6$ keV (Shidatsu et al., 2019). There are many studies (Shidatsu et al., 2018; Buisson et al., 2019; Kara et al., 2019; Muñoz-Darias et al., 2019; Paice et al., 2019; Stiele & Kong, 2020; Mudambi et al., 2020; Wang et al., 2020; Tetarenko et al., 2021; Bhargava et al., 2021; Wang et al., 2021; Paice et al., 2021; Zdziarski et al., 2021a; Dziełak et al., 2021; Ma et al., 2021; Rodi et al., 2021; Marino et al., 2021; Mastroserio et al., 2021; Kawamura et al., 2022) that address various spectral and temporal properties of the source. But these works mainly focus on the LHS of the source. A comprehensive spectral study of the outburst, particularly in the HSS, has not been done. We aim to understand the spectral and timing properties of the 2018 double outbursts of the source in total using multi-instrument data. The reflection modelling of *NuSTAR* data alone has been performed for selected observations before but never throughout the outbursts. Here, we considered the entire 2018 outburst for reflection studies and extended it to the lower energy band using simultaneous observations of *NICER-NuSTAR, XRT-NuSTAR*, AstroSat. We attempt to understand the accretion scenario of the source during the outburst.

4U 1543−47 is a galactic LMXB that was first discovered in 1971 and has undergone five outbursts. The fifth outburst, which occurred in 2021 (Negoro et al., 2021a), marked the source as the brightest BH-XRB ever discovered with a peak X-ray intensity of ~ 11 Crab in $2 - 4$ keV with *MAXI/GSC* (Negoro et al., 2021b). There has been no comprehensive study in the literature based on the 2021 outburst of 4U $1543 - 47$. In this study, we aim to provide a detailed analysis of the wideband spectral and timing characteristics of the 2021 outburst using data from three different instruments: *NICER*, *NuSTAR* and *AstroSat*. We report the presence of strong and dynamic absorption features in the 2021 outburst spectra, which has not been observed in any previous outbursts of 4U $1543 - 47$. These absorption features are observed between 8−11 keV, which is in contrast to the absorption signatures

($\sim 6.4-7$ keV) generally observed in XRBs. We quantitatively examine these features using phenomenological modelling of NuSTAR data and attempt to determine the origin of this unique absorption feature.

Chapter 2

X-ray Telescopes, Data Reduction and Analysis

The first space X-ray telescope *Uhuru* (Giacconi et al., 1971) was launched in 1970 on December 12. Collimated proportional counters were used to carry out all-sky monitoring. The instrument detected hundreds of X-ray sources and determined the positions of sources Cyg X−1, Cyg X−2, Sco X−1, and Cas A (Tananbaum et al., 1971). It also detected X-ray emissions from several extragalactic sources including NGC 1275, NGC 4151 and NGC 1068 (Gursky et al., 1971). A new revolution in X-ray astronomy occurred with the launch of *Einstein* (Giacconi et al., 1979) observatory in 1979, which introduced the grazing incidence focusing optics with imaging proportional counters. Another big technological advance was the introduction of X-ray-sensitive charge-coupled devices (CCD) by the launch of *ASCA* (Tanaka et al., 1994). The current generation of X-ray telescopes, for example, *XMM-Newton* (Jansen et al., 2001), *Chandra X-ray observatory* (Weisskopf, 1999), *eROSITA* (Merloni et al., 2012; Predehl et al., 2021), are highly sensitive and provide high-resolution spectroscopic data.

In this thesis work, we used four X-ray instrument data for the broadband analysis: *Swift/XRT, NICER, NuSTAR* and *AstroSat*. The important features of these observatories and the data reduction techniques are covered in the following sections.

2.1 X-ray Observatories

An X-ray instrument's *spatial* (or *angular*) *resolution* refers to its ability to distinguish two nearby sources. It is determined by the point spread function (PSF), which indicates the photon distribution from a point source. The measure of spread is quantified either with the *half-power diameter* or with its *full width at half maximum* (FWHM). The *effective area*

of the instrument determines the photon collection rate. The detector cannot register any events during read-out, leading to a *dead time*. Therefore, the actual effective *exposure time* of an observation requires correction for dead time. The product of the *effective area* and effective *exposure time* determines the instrument's sensitivity. For extremely bright sources, multiple photons may be recorded as a single event with energy equal to the sum of individual photon energies. This effect is known as pile-up (Ballet, 1999) and can lead to inaccurate measurements of the source properties. It distorts the measured energy spectrum. Sometimes *pile-up* leads to the rejection of the event if the sum of energies exceeds a limiting value, resulting in a dip in the centre of the source PSF. Removing a few pixels from the central region of the detector can avoid the pile-up effect. It is much less of a problem with proportional counters than with CCD detectors.

2.1.1 Neil Gehrels Swift Observatory

Swift (Gehrels et al., 2004) mission was developed by an international collaboration led by NASA and launched in November 2004. Gamma-ray burst (GRB) astronomy is the primary

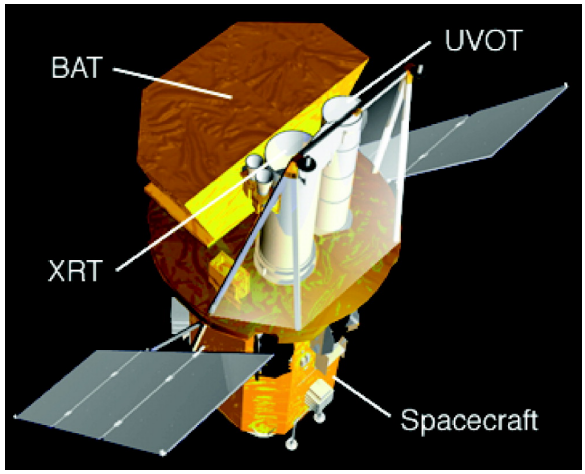

Figure 2.1: A schematic diagram of the *Swift* satellite. Credit: Gehrels et al. (2004)

objective of this mission, but it has also made significant contributions to the study of X-ray binaries. It consists of three instruments; Burst Alert Telescope (*BAT*), X-ray Telescope (*XRT*) and Ultraviolet/Optical Telescope (*UVOT*). A schematic picture of the *Swift* satellite with all its instruments is shown in Fig.. 2.1. For this study, we only use *XRT* (Burrows et al., 2005) telescope data, so other instruments' features are not discussed further.

Swift/XRT is a grazing incidence Wolter type I telescope, in which the X-rays undergo two reflections, first by a paraboloid mirror and then by a hyperboloid mirror, before being

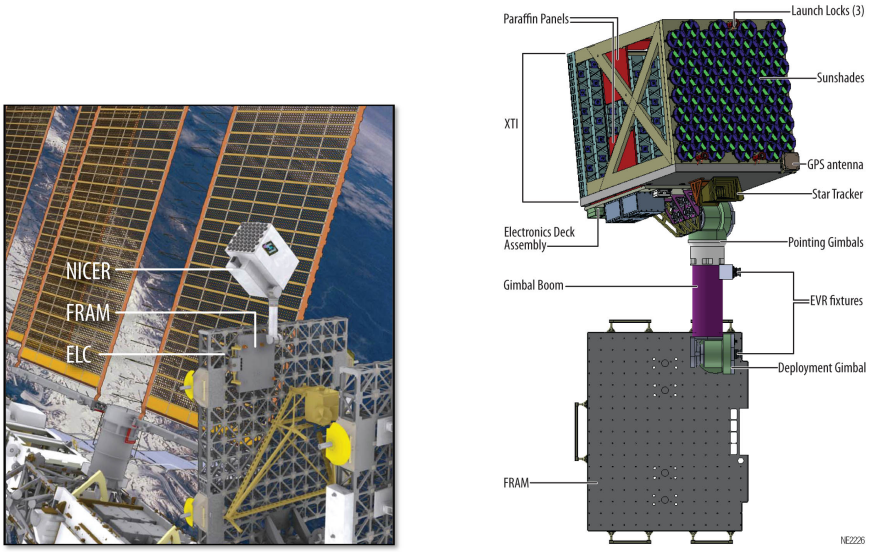

Figure 2.2: *NICER* onboard the International Space Station (left). Credit: *NICER* mission website.

focused. A CCD detector of 600×600 pixels is placed at the focal plane. The instrument operates in the energy range 0.2−10 keV with an energy resolution of about 140 eV at 6 keV. There are four operating modes available for *XRT*, namely Imaging mode (IM), Photo-Diode mode (PD), Windowed Timing mode (WT) and Photon Counting mode (PC). We have used observations in WT mode, which provides one-dimensional imaging of the source. In this mode, the CCD is continuously clocked in a parallel shift direction, resulting in an image of a vertical streak across the sensor. The time resolution of this mode is 1.7 ms. The pile-up in WT mode occurs when the source intensities reach ∼100 counts s^{-1}. A few pixels in the central streak can be removed in WT mode to eliminate the pileup problem.

2.1.2 NICER

The Neutron star Interior Composition Explorer (*NICER*) (Gendreau et al., 2016) was placed onboard the International Space Station (ISS) on 3 June 2017. Fig. 2.2 shows a schematic picture of *NICER*[1]. It's X-ray Timing Instrument (*XTI*) is a non-imaging telescope intended to obtain soft X-ray emissions from compact X-ray sources, particularly neutron stars, to probe their interior composition, dynamic processes, and radiation mechanisms. The focal plane of *XTI* consists of 56 Silicon Drift Detectors (SDD), each with its own set of compact X-ray focusing optics (X-ray concentrators, XRC) (Okajima et al., 2016). Each detector

[1] `https://heasarc.gsfc.nasa.gov/docs/nicer/`

package is called a Focal Plane Module (FPM). These FPMs are arranged into a 7 x 8 array with an effective area of 1900 cm^2 at 1.5 keV. Every 8 FPMs are part of a single Measurement and Power Unit (MPU). The labelling of the FPMs is done with two digits; the first digit corresponds to the MPU (0−6) it belongs to, and the second corresponds to the FPM slot (0−7) in the MPU. For instance, the first FPM on the first MPU is '00'. Out of the 56 focal plane modules, FPM 11, 20, 22 and 60 are not functional. The SDD detects individual photons and records their energies and times of arrival with an unprecedented resolution of 100 nanoseconds. It is suitable for the spectral and timing study of XRBs in the energy range 0.2−12 keV.

2.1.3 *NuSTAR*

The Nuclear Spectroscopic Telescope Array (*NuSTAR*) satellite (Harrison et al., 2013) is the first focusing optics X-ray telescope to detect hard X-rays with high sensitivity. NASA launched it on 13 June 2012. The mission employs advanced hard X-ray optics and solid-state detector technologies. It operates in the energy band 3−79 keV and is suitable for observing bright sources without pile-up. The mission's objectives include observing obscured AGN activity at a redshift of $\lesssim 2$, hard X-ray emission from compact objects, non-thermal radiations from supernova remnants, etc.

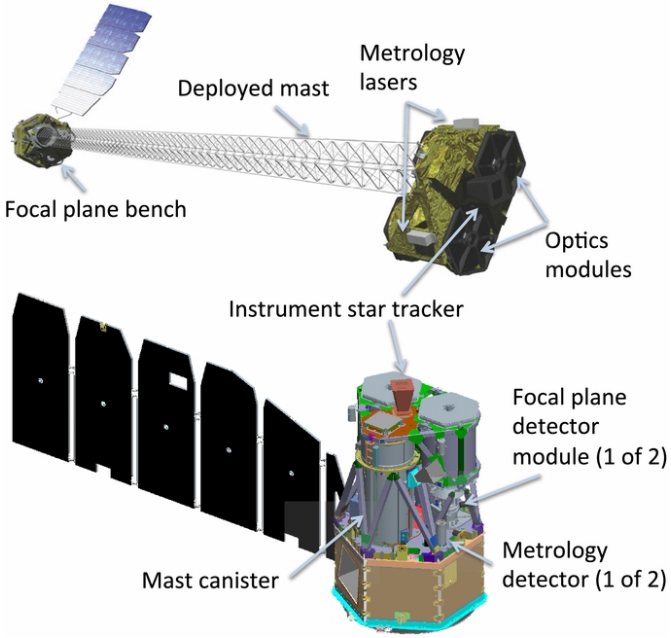

Figure 2.3: The obsolete (bottom) and deployed (top) configurations of the *NuSTAR* observatory. Credit: Harrison et al. (2013)

NuSTAR consists of two co-aligned grazing-incidence X-ray telescopes, named Focal Plane Modules A and B (*FPMA* and *FPMB*). The X-ray mirrors are multi-layer-coated and are arranged in Wolter-type I geometry with two independent focusing units. The two benches are separated by a mast deployed after the launch (see Fig. 2.3). The mast connects the optics and the focal plane modules. This setup provides a focal length of 10.14 m for the instrument. The low graze angle X-ray optics and the multi-layer coatings with a large collection area of around 850 cm^2, extend the X-ray detection capability up to an energy of $\sim$ 79 keV.

thereby extending the X-ray reflectivity at high energies, that is why NuSTAR is capable of providing X-ray focusing upto 79 keV. Its unprecedented combination of sensitivity and spatial and spectral resolution (400 eV at 10 keV) makes it the most suitable instrument for studying emission and absorption features in the spectra of XRBs.

2.1.4 *AstroSat*

AstroSat (Agrawal et al., 2017) is the first Indian multi-wavelength astronomy mission devoted to broadband studies. It was launched by Indian Space Research Organization (ISRO) on 28 September 2015. Fig. 2.4 shows a schematic diagram of *AstroSat*[2]. It consists

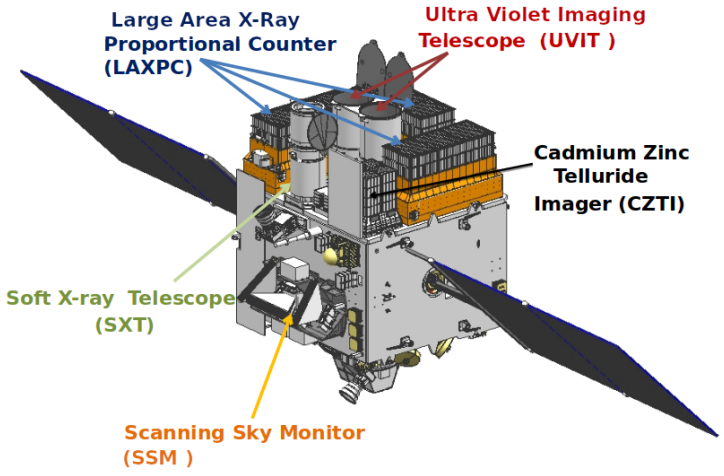

Figure 2.4: A schematic diagram of *AstroSat* with its five instruments, *SXT, LAXPC, CZTI, UVIT* and *SSM*. Credit: ISSDC, ISRO

of five instruments, namely, the Soft X-ray Telescope (*SXT*), Large Area X-ray Propor-

[2]https://www.issdc.gov.in/astro.html

tional Counters (*LAXPC*), Cadmium-Zinc-Telluride Imager (*CZTI*), Ultraviolet Imaging Telescope (*UVIT*) and Scanning Sky Monitor (*SSM*). Of these five, *SXT, LAXPC, CZTI* and *SSM* contribute to the X-ray regime. *SSM* is designed to continuously monitor the transient X-ray sky, enabling the detection and localization of X-ray sources. *LAXPC* is the only non-imaging telescope. In this work, we have used simultaneous *SXT* and *LAXPC* observations for broadband studies.

SXT (Singh et al., 2017) is a grazing incidence Wolter type I telescope operating in the energy range 0.3−8 keV. It focuses X-rays into a CCD detector of size 600 × 600 pixels. *SXT* has an effective area of about 120 cm^2 at 1 keV. It has four operational modes: Photon Counting (PC) mode, Fast Windowed (FW) mode, Bias Map (BM) mode, and Calibration Mode (CM). *SXT* is comparatively less affected by pile-up; hence it is ideal for observing bright sources.

LAXPC (Yadav et al., 2016) is operating in the energy range 3−80 keV. It consists of three identical proportional counters, namely *LAXPC10, LAXPC20* and *LAXPC30* with a total effective area of ∼6000 cm^2 at 5 keV. Each *LAXPC* detector operates independently with a time resolution of 10 μs, making it suitable for studying periodic and non-periodic variability of X-ray sources. The energy resolution of *LAXPC* is ∼18% at 6 keV. The detectors *LAXPC10* and *LAXPC20* are filled with a xenon-methane mixture and *LAXPC30* is filled with xenon-argon-methane (to improve the energy resolution) mixture at 2 atm pressure.

The characteristics of all the X-ray telescopes used in this work are summarized in Table 2.1.

Table 2.1: Characteristics of different X-ray telescopes used in this study.

Mission	Instrument	Energy range (keV)	Energy resolution	Time resolution	Effective area
Swift	*XRT*	0.2−10	140 eV @ 6 keV	1.7 ms (WT)	∼125 cm^2 @ 1.5 keV
NICER	*XTI*	0.2−12	137 eV @ 6 keV	< 300 ns	1900 cm^2 @ 1.5 keV
NuSTAR	*FPMA & FPMB*	3−79	400 eV @ 10 keV	2 μs	847 cm^2 @ 9 keV
AstroSat	*SXT*	0.3−8	90 eV @ 1.5 keV	2.4 s	90 cm^2 @ 1.5 keV
	LAXPC	3−80	18 % @ 6 keV	10 μs	6000 cm^2 @ 5 keV

2.2 Multi-instrument Data Reduction

The data recorded onboard (raw data) various instruments are transmitted to their ground stations for further processing. The initial data processing is instrument-specific and is performed by the instrument team. First, the raw data is converted to Level 1 data using different attributes of an event and housekeeping information. Further, it is processed to generate Level 2 data which contain more physical aspects like the position of the source in the sky, event rate, event time at Earth, events produced by high-energy cosmic particles, etc. These data are well organized and archived at the instrument website and common repositories like the High Energy Astrophysics Science Archive Research Center (*HEASARC*[3]) for scientific utilization by the astrophysics community.

Each instrument has specific data reduction packages called 'pipelines' to produce cleaned, calibrated event lists and standard high-level scientific products. The incoming photon (event) produces an amount of charge in the detector depending its energy. This is called Pulse Height Amplitude (PHA). Data processing uses the latest calibration information encoded in the detector response matrix to convert this PHA into PI (Pulse Invariant), which has a linear relationship with the energy of the incoming X-ray photon. The detector responses are of two types, Ancillary Response Files (ARF) and Response Matrix Files (RMF). ARF provides the effective area of the detector at each channel in units of cm^2, and RMF is a matrix containing information about the energy redistribution of the photon. Each mission provides response files for their respective instruments or can be generated as per their instructions.

We use NASA's *HEASARC software* or `HEAsoft`[4] for data reduction. We use the imaging software `ds9`[5] for visualizing the image and extracting the source and background *regions*. A selected region around the source contains both source and background events. Therefore, we need an additional background region near the source to subtract the background events from the source information. The data in the entire duration of observation are not useful due to the presence of the Sun and the Moon, the occultation of Earth, the belt of high-energy charge particles, and many other factors. Therefore, a *good time interval* (GTI) is chosen to filter out the science product. The useful events are selected by various aspects such as *regions*, GTIs, etc. Scientific products (spectra, lightcurves, etc.) are extracted from such events of interest using the respective pipelines of each instrument. These products

[3] `https://heasarc.gsfc.nasa.gov/`
[4] `https://heasarc.gsfc.nasa.gov/docs/software/lheasoft/`
[5] `https://sites.google.com/cfa.harvard.edu/saoimageds9?pli=1`

are used for further analysis to extract scientific outputs. In the next sections, we discuss the data reduction process of the instruments used in our study.

2.2.1 Reduction of *Swift/XRT* Data

We used *Swift/XRT* data for the spectral analysis of the source MAXI J1820+070. *XRT* observed the source in windowed timing mode. It covers a field of view of 8 arcmin and provides one-dimensional imaging information. Data reduction is performed using standard procedures according to the instrument website[6]. Level 2 products are generated from Level 1 data using *xrtpipeline* script. We select a circle of radius 30 pixels around the image centre (the brightest pixel) as the source region, and an annular region of 70 − 130 pixels radii is taken as the background region (see Fig. 2.5)). The pile-up limit for WT mode data is ∼ 100

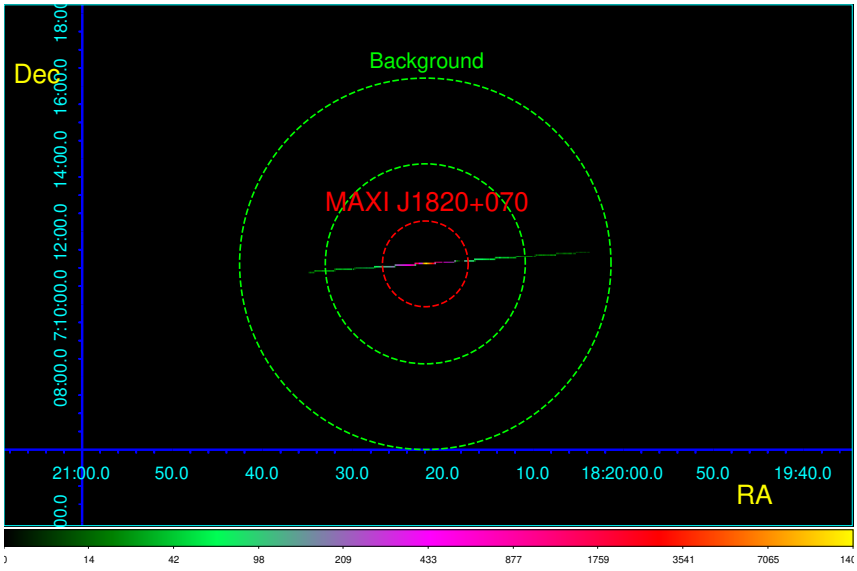

Figure 2.5: Image of the BH-XRB source MAXI J1820+070 using *Swift/XRT* in logarithmic scale. The red inner circle with a radius of 30 pixels represents the source region. The green annulus with an inner radius of 70 pixels and an outer radius of 130 pixels represents the background region.

counts s^{-1}. For pile-up data, we select an annular source region with an outer radius of 30 pixels and a varying inner radius for the analysis. The size of the inner radius is determined such that the data in the annular source region remain pile-up free. We use `XSELECT (V2.4g)` to produce standard spectra corresponding to the source and background regions. Then, we edit the `BACKSCAL` keyword in the source and background spectrum header files

[6] `https://www.swift.ac.uk/analysis/xrt/`

for each observation according to the size of the corresponding regions selected. ARF files are generated using the `xrtmkarf` tool with the source spectra and exposure map. We group the source spectra into 20 photons per bin, and no systematics are added. We use the RMF files from the CALDB version 20190910[7].

2.2.2 Reduction of *NICER* data

We used *NICER* data for spectral and timing analysis of MAXI J1820+070 and 4U 1543−47 since it has good coverage for both sources over the entire study period. We reduced the *NICER* data using the `NICERDAS`[8] tools in `HEAsoft v6.26.1` with the `20200722 caldb` version for MAXI J1820+070 and `HEAsoft v.6.29` with the `caldb` version `20210707` for 4U 1543−47. Out of the 56 focal plane modules of *NICER/XTI*, FPM 11, 20, 22, and 60 are not functional. In addition, we excluded FPM 14 and 34 due to their increased noise level. During the brightest phase of the outbursts, most detectors were turned off to avoid telemetry saturation. We checked the total number of active detectors in each observation to account for the reduction in the effective area. Level 2 standard calibration and filtering are done with the help of `nicerl2` task and applied barycenter corrections using task `barycorr` with `refframe="ICRS"`. The resulting event files are used to generate spectra and lightcurves with a time bin of 0.003 s using `XSELECT`. The ARF and RMF files are computed for each observation based on the number of active detectors. The background files are generated using `nibackgen3C50`[9] (Remillard et al., 2021). We grouped the source spectra of both sources with 25 photons per bin and added systematics of 1.5% (Fabian et al., 2020) for MAXI J1820+070 and 1% (as suggested by the instrument team) for 4U 1543−47.

2.2.3 Reduction of *NuSTAR* Data

We used *NuSTAR* observations for the simultaneous broadband spectral studies of the sources MAXI J1820+070 and 4U 1543−47. The data reduction is carried out using `NuSTARDAS`[10] software. The data processing involves three major stages: creating the calibrated event files, screening the files, and generating high-level scientific products. We used the `nupipeline` task for filtering event files with the keyword `saamode` set to

[7] `https://heasarc.gsfc.nasa.gov/docs/heasarc/caldb/data/swift/xrt/index/cif_swift_xrt_20190910.html`

[8] `https://heasarc.gsfc.nasa.gov/docs/nicer/nicer_analysis.html`

[9] `https://heasarc.gsfc.nasa.gov/docs/nicer/tools/nicer_bkg_est_tools.html`

[10] `https://heasarc.gsfc.nasa.gov/docs/nustar/analysis/`

strict, tentacle to yes and statusexpr="STATUS==b0000xxx00xxxx000" since we are dealing with extremely bright sources (Buisson et al., 2019). We used a circular region of radius 30 and 35 pixels, respectively, for MAXI J1820+070 and 4U 1543−47 centred to the brightest pixel as the source region to extract the science products for both telescopes, *FPMA* and *FPMB*. Background spectrum is extracted using a circular region of similar size away from the source position. The NUPRODUCTS task is used to generate science products such as lightcurves, energy spectra, RMF, and ARF for both *FPMA* and *FPMB*. The spectra of both sources are grouped with a minimum of 50 counts per bin without any systematics.

2.2.4 Reduction of *AstroSat* Data

We have used simultaneous *SXT* and *LAXPC* data for broadband spectral studies of MAXI J1820+070 and 4U 1543−47. Also, we used *LAXPC* data for timing studies of 4U 1543−47.

SXT observations of both sources are in the photon counting mode. The orbit-wise *SXT* cleaned Level 2 event files are merged to get a single event file for each observation using event merger python routine[11] based on *Julia v 1.1.1*. The merged event file is then loaded into XSELECT, where we select single-pixel events by applying a grade 0 filter to avoid optical data leakage (Singh et al., 2021; Prabhakar et al., 2022). The extracted *SXT* images for two observations (MJD 58309 and MJD 58355) of MAXI J1820+070 show no counts in the central region because of high pile-up[12]. Additionally, we observed a pile-up in the energy spectra beyond 4 keV. Therefore, for these two observations, we excluded the central dark patch through annular extraction with an inner radius of $3'$ and an outer radius of $16'$. In the case of 4U 1543−47, the first two offset observations have a count rate of < 40 counts s^{-1}; hence, the corresponding spectra wouldn't have pileup issues. We selected a circular region of radius $10'$ in the image to extract the source spectrum and lightcurves for two offset observations. However, in all the pointed observations of 4U 1543−47, we find the central region of the image to be very bright, which could cause a pile-up effect. Therefore, source files are extracted from an annular region of the outer radius of $15'$ and inner radius of $2'$ for these observations. The *AstroSat/SXT* image of the BH-XRB 4U 1543 − 47 in MJD 59457 is shown in Fig. 2.6 with source region marked. We used the standard *SXT* background spectrum and instrument RMF file provided by the instrument team[13]. ARF for the selected region is obtained from python-based tool sxtarfmodule provided by the *SXT* team. The final spectrum is grouped into 30 photons per bin for all the observations of

[11] https://www.tifr.res.in/~astrosat_sxt/dataanalysis.html
[12] http://www.iucaa.in/~astrosat/AstroSat_handbook.pdf
[13] https://www.tifr.res.in/~astrosat_sxt/dataanalysis.html

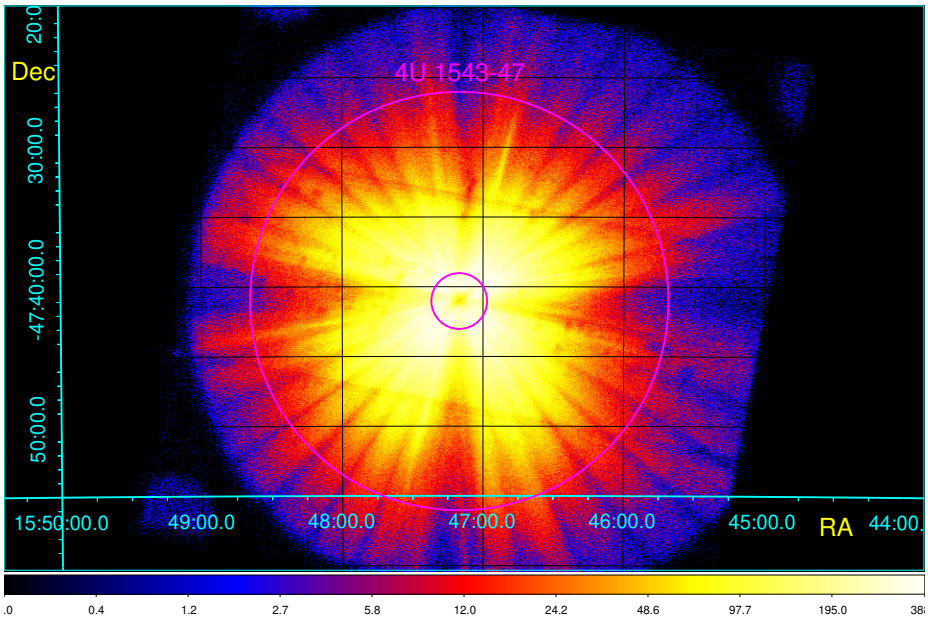

Figure 2.6: The *AstroSat/SXT* image of the source 4U 1543 − 47 during observation on MJD 59457 obtained using PC mode.

MAXI J1820+070 and the four pointed observations of 4U 1543−47. However, we chose 20 counts per bin based on the source brightness for the two offset observations of 4U 1543−47.

We utilized data from *LAXPC20* only, out of the three *LAXPC* proportional counters, due to its steady gain (see also Bhuvana et al. 2021; Baby et al. 2021; Bhuvana et al. 2022; Prabhakar et al. 2022). We make use of the latest version of single routine *LAXPC* software `LaxpcSoftversion 3.4.3`[14] (Antia et al., 2022) to extract the spectrum, lightcurve, and response files for source and background from Level 2 *LAXPC* data. We used only single events and the top layer of *LAXPC* unit to avoid the instrumental effects at high-energy. For 4U 1543−47, the software generated *LAXPC* response files are used for pointed observations, and a 40′ offset *LAXPC* response file provided by the instrument team is used for the offset observations (see also Baby et al. 2020; Katoch et al. 2021). The LAXPC spectra for MAXI J1820+070 and pointed observations of 4U 1543−47 are grouped into 30 photons per bin. However, the spectra of the offset observations of 4U 1543−47 are grouped with 20 photons per bin.

For both *SXT* and *LAXPC*, we used systematics of 2% as prescribed by the instrument team for both sources.

[14]`http://www.tifr.res.in/~astrosat_laxpc/LaxpcSoft.html`

2.3 X-ray Spectral Analysis

The standard method used for spectral analysis (modelling) involves fitting observed and model spectra. It is carried out using dedicated spectral fitting software. In such a platform, we can combine the observed spectra, detector response, and different astrophysical spectral models for estimating the spectral parameters.

The spectrum is nothing but the observed counts in different detector channels. The relationship between the source counts and the observed counts is given by

$$C(k) = T_{expo} \int R(k, E)\ A(E)\ S(E)\ dE, \tag{2.1}$$

where $C(k)$ is the observed counts in the detector channel number k, T_{expo} is the effective exposure time of the observation in seconds, $A(E)$ is the energy-dependent effective area (ARF) of the detector, $R(k, E)$ is the response matrix (RMF) and $S(E)$ is the source flux density in photons/cm^2/s/keV. Based on the physical processes taking place in the source, a model spectrum is presumptively assumed. The model flux is convolved with the spectral responses of the instrument to predict the flux from the instrument. It is now compared to the observed flux using any fitting statistics. Two statistics commonly used in data analysis are $C-$stat and χ^2, which correspond to Poisson and Gaussian probability distributions, respectively. For example, the χ^2 statistics is defined as:

$$\chi^2 = \sum_k \frac{(C(k) - M_k)^2}{\sigma_k^2}, \tag{2.2}$$

where M_k is the model predicted number of counts in the detector channel k and σ_k is the uncertainty (standard deviation) in $C(k)$. Minimizing the value of χ^2 is equivalent to maximizing the likelihood function. Also, the background contribution in the source region can be removed by subtracting the background spectrum from the source spectrum. The obtained (background-subtracted) spectrum is utilized for modelling, where the spectral parameters are adjusted until the best fit for the data is obtained by minimizing the statistics. If the model is inadequate for fitting the data, a new model is defined, and the process is repeated.

We carried out spectral fitting using the software *XSPEC*. It has a huge library of models that represent various physical phenomena. The models can be of different types: additive, multiplicative, convoluted, etc. Additive models represent various emissivity models associated with the source, such as thermal emission models, powerlaw, emission

lines, etc. In contrast, multiplicative models modify the spectrum produced by additive models by an energy-dependent multiplicative factor, and convolution models modify the spectrum as a whole. Different models can be combined according to their type to get a possible physical picture of the system.

2.3.1 Models used in Spectral Study

The X-ray continuum spectrum is produced by thermal, for example, blackbody radiation, and non-thermal, such as Comptonization. We have discussed different characteristic features in the spectrum of an XRB in §1.6.1. Spectral modelling involves understanding the observed spectral features and using appropriate physical models to address them. This section will briefly detail the various models employed in this work.

(a) Interstellar Absorption

In spectral modelling, first, we must take care of the X-ray foreground absorption by the interstellar medium (ISM), which attenuates the source signal. When X-ray photons from the source interact with atoms in the ISM, it can ionize them by ejecting an electron from it (*photoionization* or *photoelectric absorption*). The amount of absorbing material in the line of sight is quantified as *column density*, which is the number of absorbing particles per unit area within an absorption column extending from the source to the observer. The net absorption is caused by the superposition of absorption column densities of different elements, and it depends on their abundances. The spectral analysis software uses predefined abundance tables. In X-ray data analysis, the total interstellar absorption is quantified by the equivalent hydrogen column density (n_H), which gives the number of hydrogen atoms per unit cross-sectional area along the line of sight in cm^{-2}. The observed intensity of the radiation is given by

$$I(E) = I_s(E)\ e^{-a(E)n_H} \tag{2.3}$$

where I_s is the emitted source intensity and $a(E)$ is the *photoelectric* cross-section. The extent of absorption decreases with an increase in the photon energy. It is significant only in the low-energy ($\lesssim$ 2 keV) regime of the spectrum. There are several models in *XSPEC* for ISM absorption. We use the model `tbabs` (Tuebingen-Boulder ISM absorption model) (Wilms et al., 2000), which adopts the solar abundance table (executed by the comment `abund wilm` in *XSPEC*) given by Wilms et al. (2000).

(b) Thermal Continuum Models

The low-energy soft component in the spectrum that appears at $\lesssim 1$ keV is assumed to be emitted from the accretion disc. The disc spectrum appears as a multicolour blackbody, as discussed in §1.4.2. We can determine crucial features of accretion discs, such as the inner radius, temperature, and accretion rate by fitting the spectra with a multicolour blackbody model. There are several models for the X-ray spectrum of the accretion disc in *XSPEC*, such as `diskbb, kerrbb, bbody`, etc. The `diskbb` (Mitsuda et al., 1984; Makishima et al., 1986) is the most widely used multicolour disc blackbody model. It has two parameters: the temperature (T_{in} in keV) at the inner disc radius and the normalization given by *diskbb norm* = $(r_{in}/D_{10})^2 \cos\theta$, where r_{in} is the 'apparent' inner disc radius in km, D_{10} is the distance of the source in 10 kpc (kiloparsec) and θ is the inclination of the disc in degrees. The accretion rate ($\dot{M}$) is related to these parameters as, $T_{in} \propto \dot{M}^{1/4}\ r_{in}^{-3/4}$ (Frank et al., 1992). The `kerrbb` model provides the multicolour blackbody spectrum around a rotating black hole. It has several parameters such as *eta*, the ratio of the disc power produced by a torque at the inner disc to that arising from the accretion, the specific angular momentum of the black hole, the inclination angle of the disc, the mass of the black hole in units of solar mass ($M_\odot$), the effective mass accretion rate in units of 10^{18} g s^{-1}, and the distance of the black hole from the observer in kpc.

(c) Non-thermal Models

The powerlaw nature of the spectrum in the high-energy regime is thought to arise from the inverse-Compton scattering of the thermal photons emitted by the accretion disc by the 'hot' electrons present in the corona (Sunyaev & Titarchuk, 1980; Zdziarski et al., 1994; Sunyaev & Titarchuk, 1985; Titarchuk, 1994). In the Compton scattering process, a high-energy photon interacts with a free electron and transfers its energy to the electron. If the electron has large kinetic energy that exceeds the photon energy, the inverse of Comptonization scattering happens, i.e., the low-energy photon gains energy. This is the most efficient mechanism to generate the high-energy spectrum in XRBs. For non-relativistic electrons and low-energy photons where $\mathrm{h}\nu \ll 1/2\mathrm{m_e v_e^2}$, the average energy gained by the photon is $\Delta E/E = \mathrm{h}\nu/(\mathrm{m_e c^2})$, where m_e is the mass of the electron and v_e is the velocity of the electron. If $\mathrm{h}\nu \gg 1/2\mathrm{m_e v_e^2}$, the average energy gained by the electron per inverse Compton scattering is $\Delta E/E = \frac{4}{3}\left(\frac{\mathrm{v_e}}{c}\right)^2$. If this process happens in a thermal distribution of electrons, it is called thermal Comptonization. In this case, the average energy gain per scattering can be expressed as $\Delta E/E = 4k_B T_e/(m_e c^2)$, where T_e is the electron temperature. Therefore,

considering both cases, the average energy gain per Compton scattering is given by

$$\frac{\Delta E}{E} = \frac{4k_B T_e - \mathrm{h}\nu}{m_e c^2}. \tag{2.4}$$

The Compton y-parameter quantifies whether a photon's energy will be significantly changed while passing through a medium of free electrons. It is the product of the average fractional energy change ($\Delta E/E$) per scattering and the mean number of scatterings, $Max(\tau, \tau^2)$. Here, τ is the electron scattering optical depth of the medium and is given by

$$\tau = \int \sigma_T \, n_e \, dx, \tag{2.5}$$

where σ_T is the Thomson scattering cross-section and n_e is the electron density. If $\tau \gg 1$, the mean number of scattering is τ^2, and if $\tau \ll 1$, it is just τ itself. If $y \lesssim 1$, the Compton process is insignificant, and if $y \gtrsim 1$, the spectrum will be significantly modified by Comptonization. For multiple electron scatterings, the final photon energy can be amplified by a factor of e^y if the scattered photon energy is less than $4k_B T_e$.

The repeated electron scattering in an optically thin medium ($\tau \ll 1$) results in a powerlaw photon distribution. Assuming monoenergetic photons of initial energy e_i, after m number of scatterings, the mean energy of the final photon is $e_m \sim e_i A^m$, where A is the mean amplification of photon energy per inverse Compton scattering. In an optically thin medium, the intensity of the emergent radiation can be expressed as:

$$I(e_m) \sim I(e_i)\left(\frac{e_m}{e_i}\right)^{-\Gamma}, \tag{2.6}$$

where $\Gamma \equiv \dfrac{-\ln\tau}{\ln A}$ (Rybicki & Lightman, 1979). That is, the inverse-Comptonized spectrum has a powerlaw nature, and the parameter Γ is called the *spectral index* (or *photon index*).

In XRBs, it is believed that the high-energy electrons in the *corona* (Sunyaev & Truemper, 1979) surrounding the accretion disc inverse Comptonize the soft thermal photons from the disc, producing a non-thermal photon distribution. In *XSPEC*, the `powerlaw` is one of the models to fit the non-thermal spectrum, where the radiation intensity is given by $I(E) = KE^{-\Gamma}$. Here K represents the normalization (photons/keV/cm^2) and Γ (> 0) represents the spectral index. At higher photon energies, the electron scattering cross-section is low. Also, the electrons do not have enough energy to transfer to the incoming photons, leading to an exponential cut-off in the photon spectrum at higher energies. There are several models in *XSPEC* to account for the powerlaw spectrum with high-energy cut-off, such

as `cutoffpl, nthcomp, thcomp` etc. The intensity of radiation in the `cutoffpl` model describes as, $I(E) = KE^{-\Gamma}\exp(-E/E_{cut})$, where E_{cut} is the exponential cut-off energy. The thermally Comptonized continuum model, `nthcomp` (Zdziarski et al., 1996), uses `bbody` (blackbody) or `diskbb` (multicolour disc blackbody) as the seed photon population. In this model, the high-energy cut-off is parameterized by the electron temperature. It has four parameters: the photon index Γ, electron temperature (k_BT_e), seed photon temperature (k_BT_{bb}) and the normalization. The `thcomp` (Zdziarski et al., 2020) model is an updated form of `nthcomp` model. This convolution model allows a variable fraction (cov_frac) of seed photon to undergo up and down scattering through Comptonization. Other parameters are the photon index (Γ) and electron temperature (k_BT_e) of the corona.

(d) Models for Spectral Lines

A fraction of the high-energy photon emitted from the corona can irradiate the disc (mostly the inner disc), and it causes atomic transitions in the elements of the accretion disc. It can give rise to discrete emission or absorption lines at the characteristic energy of different elements. Generally, it is assumed that the disc material comprises ionised hydrogen, helium, and other neutral elements. The most dominant process in the interaction of X-rays and the neutral disc matter is *photoabsorption*. The de-excitation of the atom can happen in two ways: the vacancy in the inner shell is filled by another electron at a higher energy level by releasing radiation (*fluorescence* emission, and the process is called radiative de-excitation), or that energy is transferred to another electron (Auger electron) in the same atom. The fluorescence yield (probability of radiative de-excitation) is directly proportional to the atomic number Z.

The spectrum of XRBs occasionally shows an emission line at $\sim 6-7$ keV produced by the iron K_α fluorescence. This feature can be modelled using the *XSPEC* model `gauss` to some extend, which is the Gaussian profile given by

$$I(E) = \frac{K}{\sigma\sqrt{2\pi}} \exp\left[-\frac{(\mathrm{E}-\mathrm{E}_0)^2}{2\sigma^2} \right]. \tag{2.7}$$

Here, E_0 is the transition line energy (centroid energy of the Gaussian), σ is the line width, and K is the normalization in units of photons/cm^2/s.

Also, the X-ray spectrum sometimes shows the absorption lines, which can be modelled

by `gabs`[15]in *XSPEC*. It has the Gaussian absorption profile:

$$I(E) = \exp\left[- \frac{\mathrm{D}}{\sigma\sqrt{2\pi}} \exp\left(- \frac{(\mathrm{E} - \mathrm{E}_0)^2}{2\sigma^2} \right) \right] \tag{2.8}$$

where D is the line depth (*strength*).

K-shell has the largest photoabsorption cross-section at a particular photon energy. A sudden onset of absorption in a specific energy level of an atom happens when the photon energy exceeds this threshold value. This creates a sharp *absorption edge* feature in the spectrum. The `edge` and `smedge` models in *XSPEC* are generally used to represent the *absorption edge*. The `edge` model has the functional form,

$$I(E) = \begin{cases} 1 & \text{if } \mathrm{E} \leq \mathrm{E}_g \\ \exp[-\mathrm{D}\,(\mathrm{E}/\mathrm{E_g})^{-3}] & \text{if } \mathrm{E} \geq \mathrm{E}_g, \end{cases} \tag{2.9}$$

where E_g is the threshold energy. The smeared edge (`smedge`) (Ebisawa et al., 1994) model has three parameters: the threshold energy, the maximum absorption factor at the threshold, and the smearing width.

Besides emission and absorption features, the hard photons may also get Compton scattered by the free or bound electrons. The photons which are Compton back-scattered out of the disc produce the 'bump' like feature in the spectra between $\sim 20 - 30$ keV, called the *Compton hump* (shown in Fig.. 1.5). The process of modelling the reflected spectrum, which is generated by the combined effect of photoabsorption, fluorescence, and Compton scattering, is referred to as *reflection spectroscopy*. It is possible to probe the physical conditions of the inner accretion disc, which is very significant in studying strong gravity regions around the BH, through reflection spectroscopy. This thesis involves modelling reflection spectra, and I will discuss this briefly in the next section.

2.3.2 Reflection Spectroscopy

The advent of high-resolution spectroscopy reveals the presence of reflection features in the spectra of many BH-XRBs. Irrespective of the geometry of the corona, it is believed that the photons up-scattered by the corona, the primary photons, interact with the disc material and a part of which produces the reflection features, as we discussed in §2.3.1. Fig.. 2.7 represents the reflection spectrum produced by an incident powerlaw spectrum (dashed

[15]`https://heasarc.gsfc.nasa.gov/xanadu/xspec/manual/node246.html`

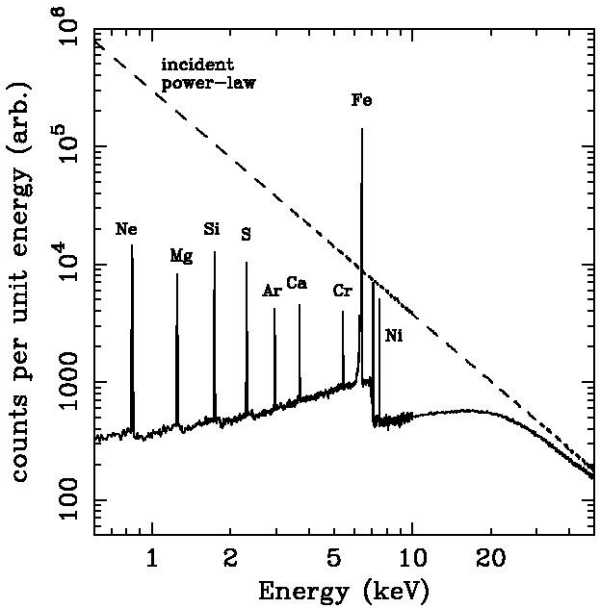

Figure 2.7: X-ray reflection spectrum (dashed line) produced by a powerlaw continuum of photon index 2, and the reprocessed spectrum (continuous line) contains the Kα emission lines from different elements. Credit: Reynolds (1999)

line) with photon index Γ =2, for an optically thick disc with a slab geometry (Reynolds, 1999). The reprocessed/reflected X-ray spectrum from the disc surface consists of a soft thermal continuum, fluorescent line emission from various elements, and a Compton hump. The strongest spectral features are the K-edge and fluorescent K_α line of iron as iron has the highest values for both the photoabsorption cross-section and fluorescent yield. For a neutral disc environment (temperature < 1 keV), the iron line peaks at 6.4 keV (Makishima, 1986). If the disc surface is photoionized, the absorbers are ionized, and the transition line energy is higher than their neutral ones. For example, the helium-like (Fe XXV) and hydrogen-like (Fe XXVI) iron species have transition energy at 6.68 keV and 6.97 keV, respectively[16]. The *ionization parameter*, ξ, measures the degree of ionization of the disc matter. It is defined as $\xi = 4\pi F(r)/n_e(r)$, where $F(r)$ is the incident X-ray flux at a radius r from the BH and $n_e(r)$ is the local electron number density.

For a distant observer, the reflection features appeared to be diluted/broadened and distorted (asymmetric) due to several reasons like the ionization state of the accretion disc surface (Fabian et al., 1989; Ross et al., 1999), Doppler effect and general relativistic effects of the strong gravity (Fabian et al., 1989, 2000). These effects are more pronounced for systems with high inclination, while in face-on systems only the transverse Doppler

[16]https://heasarc.gsfc.nasa.gov/docs/software/xstar/xstar.html

effect and gravitational redshift affect the spectrum. The relativistic reflection spectrum can give insights into the spin of the BH. The spin is strongly related to the radius of the last stable orbit (Equation 1.1) around the BH. The line emitted from the inner disc is broadened/distorted more as the disc gets closer to the BH. Also, for a rapidly spinning BH, the red wing of the line extends down to much lower energies. The reflection modelling may further provide a perception of the disc emissivity profile, which is the radial distribution of the illumination to the accretion disc by the primary photons (Wilkins & Fabian, 2011). It is parametrized as a powerlaw, $F \propto r^{-q}$, with emissivity index q. The steeper the emissivity profile, the broader the line feature. Small values of q correspond to the disc's outer region, whereas high values represent the inner regions.

Models for Reflection Spectroscopy

In our study, we performed reflection spectral modelling using a few different flavours of the relativistic reflection model *RELXILL*[17] (García et al., 2014). This is currently the most accurate model for addressing the reflection features. It combines the capabilities of the `xillver` (García & Kallman, 2010; García et al., 2013) reflection code and the `relline` (Dauser et al., 2010, 2013) ray tracing code. The remarkable aspect is that the `xillver` code calculates the reflection spectrum for each point on the disc by taking care of the proper emission angle at the disc surface instead of following an angle-averaged approach like many other reflection models. These individual spectra are then relativistically smeared by the model `relline` and then integrated to provide the total reflection spectrum. `relline` uses the *transfer function* method (Cunningham, 1975) to calculate the photon trajectory from the point of emission in the accretion disc to the observer.

In the *RELXILL* model, the primary photon source is assumed to be either an isotropic point-source at a height on the rotation axis (*lamp-post corona*) of the BH or an extended source at the inner part of the disc without any geometric assumption. Fig. 2.8 illustrates the lamp-post geometry, where the corona (blue dot) is located at a height h from the disc surface on the rotation axis of the BH. Strong light bending forces the radiation (red line) to illuminate the disc at a distance r from the BH at an angle δ_i to the surface normal.

The *RELXILL* model provides various flavours of models: `relxill, relxillCp, relxilllp, relxilllpCp, relxillD`, etc. The '*lp*' models assume a lamp-post corona. Other models lack a specific coronal geometry and assume a broken powerlaw radial emissivity profile of the corona: $F \propto r^{-q_1}$ for $r < r_{\rm break}$ and $F \propto r^{-q_2}$ for $r > r_{\rm break}$ where $r_{\rm break}$ is called the breaking radius, and q_1 and q_2 are the emissivity indices. All

[17] `http://www.sternwarte.uni-erlangen.de/~dauser/research/relxill/index.html`

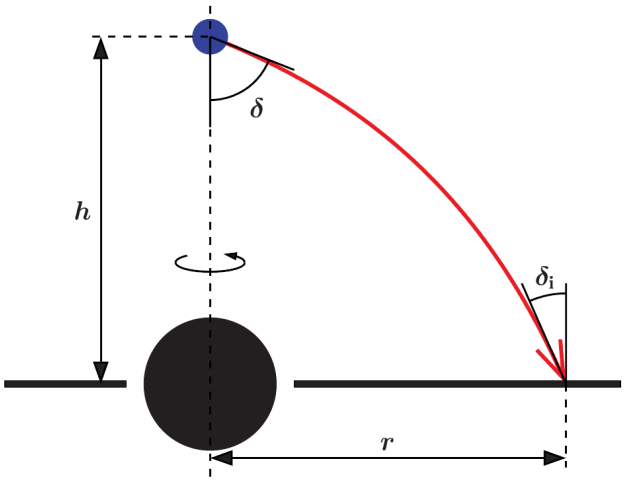

Figure 2.8: An illustration of the lamp-post geometry; where the corona (blue dot) is located at a height h from the disc surface on the rotation axis of the BH. The illumination of the disc at a radius r is shown in red. Credit: Dauser et al. (2013)

models assume a cut-off-powerlaw (photon index Γ and cut-off energy E_{cut}) as the incident primary radiation. However, the '*Cp*' models consider a thermal Comptonization continuum (`nthcomp`) as the primary photon source. Both Γ and E_{cut} (or equivalently $k_B T_e$ for 'Cp' flavour) are free parameters; however, the 'D' flavour of models (`relxillD, relxilllpD`, etc.) assumes a fixed E_{cut} at 300 keV. The density of the accretion disc is frozen at $n = 10^{15} cm^{-3}$ except for the 'D' models, which allows even higher values of disc density. The geometry of the accretion disc is constrained through its inner and outer radius (R_{in} and R_{out}), and the inclination (θ) of the inner accretion disc surface normal to the line-of-sight. The iron abundance (A_{Fe}) of the disc surface is measured in units of the solar abundance (Anders & Grevesse, 1989). The ionization parameter ($\log \xi$) is a measure of the degree of ionization of the disc surface. Furthermore, the model includes the reflection fraction (R_f) and model normalization as additional parameters. Reflection fraction is the ratio of the intensity of the primary photons illuminating the disc to that reach the observer (Dauser et al., 2016). The model output is the direct coronal emission and reflected radiation for a positive value of R_f, whereas a negative R_f provides only the reflected radiation.

2.4 X-ray Timing Analysis

As discussed in §1.6.2, XRB lightcurves show time variability, best characterised by the PDS. It generally carries the signature of the variation in the source flux and the Poisson

counting noise. An approximately flat PDS, since it does not depend on frequency, is called 'white noise', and that with a powerlaw nature is called 'red noise'. The Poisson power component must be removed from the PDS for scientific studies.

Let **x(t)** be the lightcurve that measures the photon flux continuously. In practice, X-ray the instrument records photons in discrete time intervals or bins (Δt), resulting in the measurement of the number of events (x_m) that occur within each bin. If a lightcurve segment of length T consists of N successive bins ($T = N\Delta t$), the discrete Fourier transform of x_m gives the spectral density,

$$X_k = \sum_{m=0}^{N-1} x_m e^{-2\pi i k m/N}. \tag{2.10}$$

If segment length $N = 2^m$, the PDS computation becomes easier using the fast Fourier transform. In general the Fourier frequency $f_k = \frac{k}{T} = \frac{k}{N\Delta t}$, is defined over $k \in [-N/2, N/2]$. Therefore, the minimum possible frequency will be the length of the lightcurve segment, i.e., $f_{min} = 1/T$, and the maximum frequency (Nyquist frequency) will be $f_{max} = 1/2\Delta t$. The usual practice is to divide the total lightcurve into multiple segments and compute the spectral density (periodograms) for each segment and average the periodograms. Finally, the PDS is a squared Fourier amplitude with a normalization,

$$P_k = (\text{Normalization}) \mid X_k \mid^2 . \tag{2.11}$$

There are mainly two types of normalization for the periodogram; Leahy normalization (Leahy et al., 1983) and root-mean-square (RMS) normalization. The Leahy normalization of PDS for pure Poissonian data gives a constant value of 2 (χ^2 distribution with 2 degrees of freedom). The RMS normalization expresses the PDS in units of (RMS variability/mean)^2/Hz. In X-ray timing analysis, we first compute the PDS using Leahy normalization, then subtract the Poisson power component and apply RMS normalization to obtain the intrinsic source PDS.

2.4.1 Modelling the Power Density Spectrum

The variability in power density spectra of XRBs is generally aperiodic since the accretion process is turbulent. Modelling the aperiodic variability helps to understand the dynamics of the system. We use the tool `powspec` to generate PDS from lightcurves. The `powspec` task with normalization = -2 gives the Poisson noise subtracted RMS variability. The integrated

amplitude of the continuum gives the 'fractional RMS amplitude'. We generated a flat response and used *XSPEC* to model the PDS using different models such as `powerlaw`, `cut-off powerlaw` or a combination of several `Lorentzian` functions. The broad noise features in the PDS are modelled with zero-centred `Lorentzians`. While a combination of Lorentzian is used to identify the QPOs or QPO-like features in the PDS. The functional form of Lorentzian in *XSPEC* is written as,

$$L(\nu) = \frac{L_0}{\pi} \frac{\Delta}{(\nu - \nu_c)^2 + \Delta^2}, \tag{2.12}$$

where ν is the frequency, and ν_c (characteristic frequency of QPO) is the line centre. Here, Δ is the line's half-width at half maximum (HWHM), and L_0 is the normalization. The coherence of the QPO feature is expressed using a quantity called the *Q-factor*, $Q = \nu_c/2\Delta$ (van der Klis, 2000). The *significance* of the QPO feature is the ratio of Lorentzian normalization (L_0) to its negative error (Alam et al., 2014; Sreehari et al., 2019). The area under a Lorentzian is given by

$$L_T = \frac{L_0}{2} \left[1 + \frac{2}{\pi} \tan^{-1} \left(\frac{\nu_c}{\Delta} \right) \right], \tag{2.13}$$

and the fractional RMS amplitude is calculated as $\sqrt{L_T}$.

Chapter 3

Accretion Scenario of MAXI J1820+070 during 2018 Outbursts with Multimission Observations

We are investigating the spectral and timing properties of the source MAXI J1820+070 during its 2018 outbursts. Our analysis involves utilizing data from multiple instruments, including *Swift/XRT, NICER, NuSTAR*, and *AstroSat*. Throughout the outburst, a total of 15 epochs of wideband simultaneous observations (five *XRT-NuSTAR*, seven *NICER-NuSTAR* and three *AstroSat* pairs) were identified. We perform phenomenological and reflection modelling of these observations. *Swift/XRT* and *NICER* have good coverage over the entire outburst; hence we perform phenomenological modelling of all the data available from these instruments. Also, we carry out timing analysis, using *NICER* observations of the entire outburst. The findings of this work have been published in the journal *Monthly Notices of the Royal Astronomical Society (MNRAS)* (Prabhakar et al., 2022).

3.1 MAXI J1820+070: Properties

MAXI J1820+070 (ASASSN-18ey) is a galactic low-mass X-ray binary discovered in optical by *All-Sky Automated Survey for SuperNovae* (*ASAS-SN*, Shappee et al., 2014) on 3 March 2018. A week later, on 11 March 2018, it was discovered as an X-ray transient by *Monitor of All-sky X-ray Image/Gas Slit Camera* (*MAXI/GCS*, Kawamuro et al., 2018; Denisenko, 2018; Tucker et al., 2018). It is located at $RA = 18^h20^m21^s.9$, $DEC = +07^\circ11'07''.3$ (J2000) (Kawamuro et al., 2018). MAXI J1820+070 is one of the brightest X-ray transients ever discovered, having a soft X-ray flux of ~ 4 Crab in $2-6$ keV (Shidatsu et al., 2019). There are several follow-up observations by various X-ray missions such as *Swift, NICER,*

NuSTAR, HXMT, etc. The source is also observed in radio (Bright et al., 2018). Tetarenko et al. (2021) detected highly relativistic and confined jet emission from the system in the hard state. An optical disc wind has been discovered (Muñoz-Darias et al., 2019) in the hard state, whereas Sánchez-Sierras & Muñoz-Darias (2020) reported the presence of near-infrared winds in the soft state of MAXI J1820+070.

Studies of the optical counterpart of MAXI J1820+070 by Torres et al. (2019) derived a mass function $f(M)$ of $5.18 \pm 0.15 M_{\odot}$, which is the dynamical confirmation of the black hole nature of the source. The estimated mass of the BH is in the range of $7 - 8 M_{\odot}$. The distance to the source is obtained as 2.96 ± 0.33 kpc (Atri et al., 2020) by radio parallax method using VLBA (Very Long Baseline Array). The VLBI (Very Long Baseline Interferometry) observation provides an inclination angle (θ) of 63 ± 3^0 and mass of $9.2 \pm 1.3 M_{\odot}$ (Atri et al., 2020). Later, Torres et al. (2020) did a more accurate calculation of the mass ratio $q = 0.072 \pm 0.012$, which leads to $M = 8.48^{+0.79}_{-0.72} M_{\odot}$ using $\theta = 63 \pm 3^0$ (Atri et al., 2020). Buisson et al. (2019) estimated the inner radius of the accretion disc using *NuSTAR* observations in the hard state and suggested a low-spinning BH. Guan et al. (2021) reported a spin of $0.2^{+0.2}_{-0.3}$ by continuum fitting method in the soft state data of MAXI J1820+070 using *Insight-HXMT* observations. Bhargava et al. (2021) carried out the spin measurement using the Relativistic Precession Model (RPM) on *NICER* observations, and the estimated value of the spin as $0.799^{+0.016}_{-0.015}$ under the assumption of a BH mass of $8.48 M_{\odot}$.

3.1.1 Observations

We carry out the present study using four different instrument data, i.e., *Swift/XRT, NICER, NuSTAR*, and *AstroSat*, from 12 March 2018 to 21 November 2018. Table 3.1 gives an observation summary for various instruments. We analyze and model all the data from *Swift/XRT, NICER* and *AstroSat* observations in this period and consider *NuSTAR* data only for simultaneous observations with *NICER* or *XRT*.

3.2 Spectral Modelling of MAXI J1820+070

MAXI J1820+070 underwent two successive outbursts (Outburst-I & Outburst-II) in 2018. Near the peak of Outburst-II, the source became extremely luminous, and *XRT* data suffered from a huge pile-up. A large area of the source region needs to be removed for pile-up correction, possibly severely affecting the instrument's overall PSF. Therefore, we ignore all *Swift/XRT* observations between MJD 58298 and MJD 58386 from the spectral analysis.

Table 3.1: Summary of observations of MAXI J1820+070 under study.

Mission	Start date (MJD)	End date (MJD)
Swift/XRT†	12-03-2018 (58189.02)	12-11-2018 (58434.35)
NICER	12-03-2018 (58189.58)	21-11-2018 (58443.82)
NuSTAR††	14-03-2018 (58191.90)	29-10-2018 (58420.00)
AstroSat‡	31-03-2018 (58208)	
	10-07-2018 (58309)	
	25-08-2018 (58355)	

† *Swift/XRT* observations from MJD 58298 to MJD 58386 are ignored due to a huge pile-up.
†† Only the *NuSTAR* observations simultaneous to *NICER* or *XRT* during this period are considered.
‡ There are only three *AstroSat* observations throughout our study.

Similarly, the *NICER* instrument suffers from telemetry saturation due to a high count rate during this bright phase. Several detectors were switched off to reduce the issue of telemetry saturation. Hence we used the data with a reduced number of active detectors and properly took care of the reduction of effective area in each observation. The data reduction procedure of various instruments to extract the scientific products is discussed in §2.2. The source is very bright, and we find residual in the *NICER* data below 0.8 keV (Fabian et al., 2020), therefore, we ignore the data below 0.8 keV for *NICER* as well as for *XRT* to keep a common energy range for the spectral analysis.

3.2.1 Phenomenological Modelling of *Swift/XRT* and *NICER*

We independently performed the spectral analysis using *Swift/XRT* and *NICER* (though both operate in a similar energy range) data to consider all the available observations in this energy range and scan the entire parameter space during both outbursts. Also, we aim for a comparative study of the spectral parameters estimated between these two instruments. The data analysis methodology and the description of various models used for data modelling are presented in §2.3. The *XSPEC* absorption model `tbabs` accounts for interstellar absorption. We fixed $n_H = 1.5 \times 10^{21} \mathrm{cm}^{-2}$ (Uttley et al., 2018) for the line of sight column density throughout the study.

We consider MJD 58189.02 as day 0 of the analysis; henceforth, all results are presented with respect to this reference date. At the very beginning of the Outburst-I and end

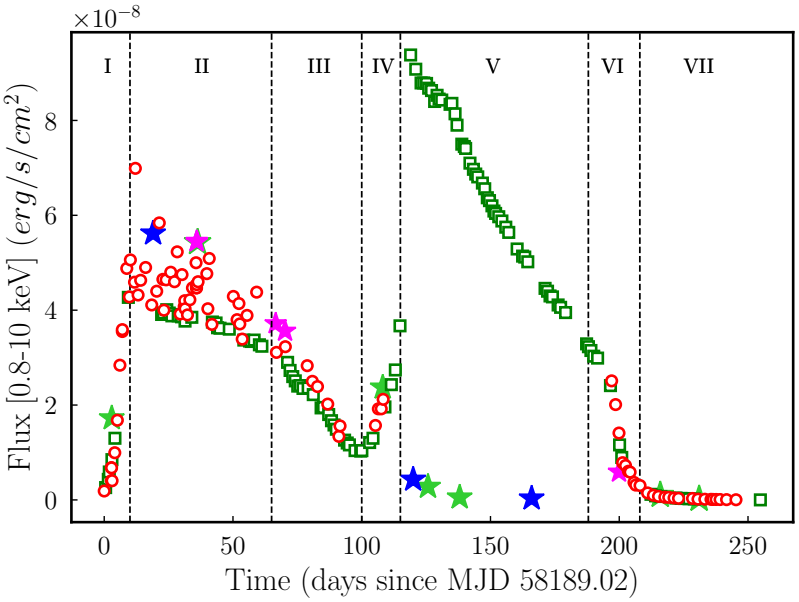

Figure 3.1: Lightcurve in the energy range 0.8 – 10 keV generated using the *NICER* and *XRT* observations of MAXI J1820+070. The red circles represent the *XRT* data, and the green squares represent the *NICER* data. The flux in the 10 – 60 keV band for the simultaneous pairs for *XRT-NuSTAR*, *NICER-NuSTAR* and *AstroSat* observations are marked with magenta, green and blue stars, respectively. Different evolutionary phases of the outbursts are marked from I to VII (see text for details).

stages of the Outburst-II, only a `powerlaw` component and the ISM absorption component (`tbabs` × `powerlaw`) are enough to model the *XRT* data. However, an additional `diskbb` component is required to model the *XRT* data in-between (`tbabs(diskbb+powerlaw)`). *NICER* data show a line signature at around 6–7 keV throughout Outburst-I. Therefore, we used an additional `gauss` component to represent the line, and the overall model is `tbabs(diskbb+powerlaw+gauss)`. For Outburst-II, the model `tbabs(diskbb+powerlaw)` is adequate for fitting the *NICER* data. We use χ^2 statistics to represent the goodness of the fit. The χ^2/dof varies in the range 0.79 – 1.38 and 0.72 – 1.33, respectively, for *XRT* and *NICER* analysis. The uncertainties in the spectral fitting parameters are calculated within the 90% confidence range using the modified Levenberg-Marquardt (`leven`) algorithm.

3.2.2 Outburst Profile and HID

We estimated the flux in 0.8 – 10 keV for individual *NICER* and *XRT* observations from MJD 58189 to MJD 58443, and plotted the lightcurve in Fig. 3.1. The red circles represent the *XRT* data, and the green squares represent the *NICER* data. We notice that the overall

fluxes of both instruments are comparable. However, as discussed in Appendix-A, there may be (10 – 20%) discrepancies in the estimated source flux due to calibration uncertainties between both instruments. Also, a slight deviation may result due to the variation of the source itself, as the *XRT* and *NICER* observations are not simultaneous. Furthermore, we suspect that a small discrepancy may be attributed to the high pile-up observed in the *XRT* data, despite our meticulous removal of the pile-up effect. Therefore, most of our conclusions are based on *NICER* data, and we present *XRT* results for comparison.

We marked different phases (I to VII) in the lightcurve to identify the evolution of the outburst. At the beginning of the outburst, MAXI J1820+070 showed an increase in flux with a short rise time (Phase-I) of $\sim$ 10 days to reach the peak and then started to decay slowly (Phase-II, also referred to as plateau phase) between $\sim 10 - 60$ days followed by a much steeper decline (Phase-III) till 100 days. After this phase, Outburst-II is triggered, with a rapid increase in flux (Phase-IV), and at around day 110, the X-ray flux reached the second peak ($9.38 \pm 0.01 \times 10^{-8}$ erg/s/cm^2), with flux approximately 1.5 times higher than the peak flux value of Outburst-I in 0.8 – 10 keV band. Then the source flux decays linearly (Phase-V) for the next 80 days, followed by an exponential decline of flux (Phase-VI). Finally, at around day 220, the source reached the quiescence (Phase-VII). We noticed that the peak flux of Outburst-I in the $2 - 10$ keV bands is larger (a factor of 2.4 for *NICER* and 3 for *XRT*) than the flux in the $0.8 - 2$ keV band, whereas the same for Outburst-II is lower by a factor of 1.2 (*NICER*). A similar trend is observed in $10 - 60$ keV band, represented by star symbols in Fig. 3.1, obtained from broadband spectral studies (see also *Swift/BAT* lightcurve in Fabian et al. (2020); Buisson et al. (2019) and *Insight-HXMT* lightcurve in You et al. (2021); Ma et al. (2021)) discussed in §3.3.1. Here magenta, green, and blue stars represent simultaneous pairs for *XRT-NuSTAR, NICER-NuSTAR* and *AstroSat* observations, respectively. It indicates that Outburst-I is harder than Outburst-II, and we explore the details in §3.2.3.

We also separately estimate the flux in $0.8 - 2$ keV (low) and $2 - 10$ keV (high) for all *XRT* and *NICER* observations. We define the hardness as the ratio of flux in $2 - 10$ keV band to that in $0.8 - 2$ keV band. The hardness-intensity diagram (HID) for the outburst is plotted in Fig. 3.2. Here also, the red circles represent the *XRT* data points, and green squares represent the *NICER* data points. The HID of the two instruments shows an offset in HR, particularly when the source is bright during Outburst-I. Compared with *XRT*, the *NICER* flux is $\sim$ 10% higher in the low-energy band but $\sim$ 10% lower in the hard energy band, maintaining a comparable total flux (see Appendix-A). This results in a $\sim$ 22% lower HR for *NICER* data than *XRT*. Enhancing the *NICER* HR by this factor makes both HID

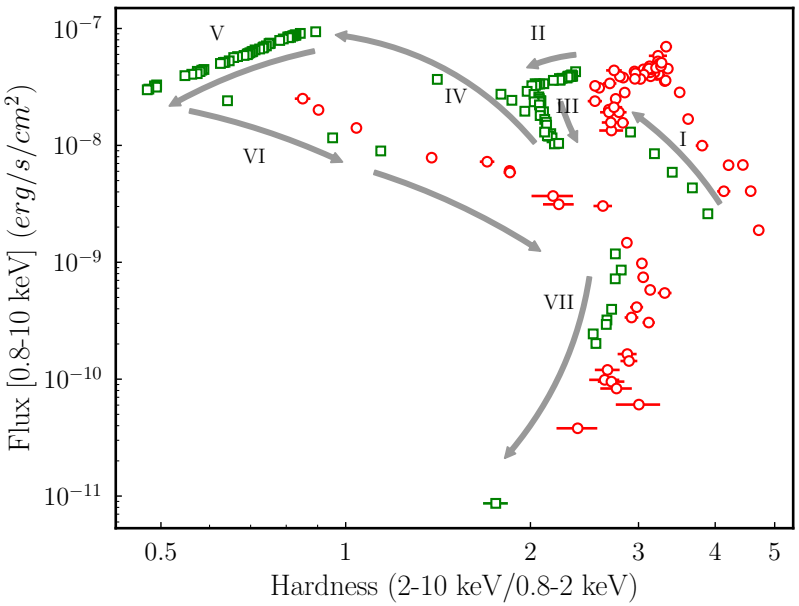

Figure 3.2: The Hardness-Intensity diagram of the source MAXI J1820+070 during the 2018 outburst. The hardness is calculated as the ratio of fluxes in 2 – 10 keV to 0.8 – 2 keV for both *NICER* and *XRT*. The red circles represent the *XRT* data, and the green squares represent the *NICER* data. Various phases (I-VII) of the lightcurve are marked. See text for details.

comparable. Various phases are marked from I-VII to indicate the evolution of the source in the HID. The outburst starts with low-luminosity LHS (Phase-I) with the highest HR and then evolves approximately at a constant flux level (Phase-II) with a significant change in HR. The source flux decreases roughly at a constant HR (Phase-III) between $\sim 60 - 100$ days. During Outburst-I, the source remains only in the LHS (Phase-I to III in Fig. 3.2), and is identified as a 'failed-transition' outburst. Outburst-II is triggered through Phase-IV (very short intermediate state) with an enhancement of flux, and the source reaches the HSS (Phase V). The source transitions back to the LHS (Phase-VII) during the decline phase through an intermediate state (Phase-VI), completing a q-shaped hysteresis cycle since the hard-to-soft transition occurs at a higher flux than soft-to-hard. It is a complete outburst since it covers all the spectral states.

3.2.3 Evolution of Spectral Parameters

The aim is to study the evolution of the spectral parameters during the progress of the outbursts to understand the accretion geometry and the associated physical process. We modelled all the *XRT* and *NICER* data using a combination of the phenomenological models

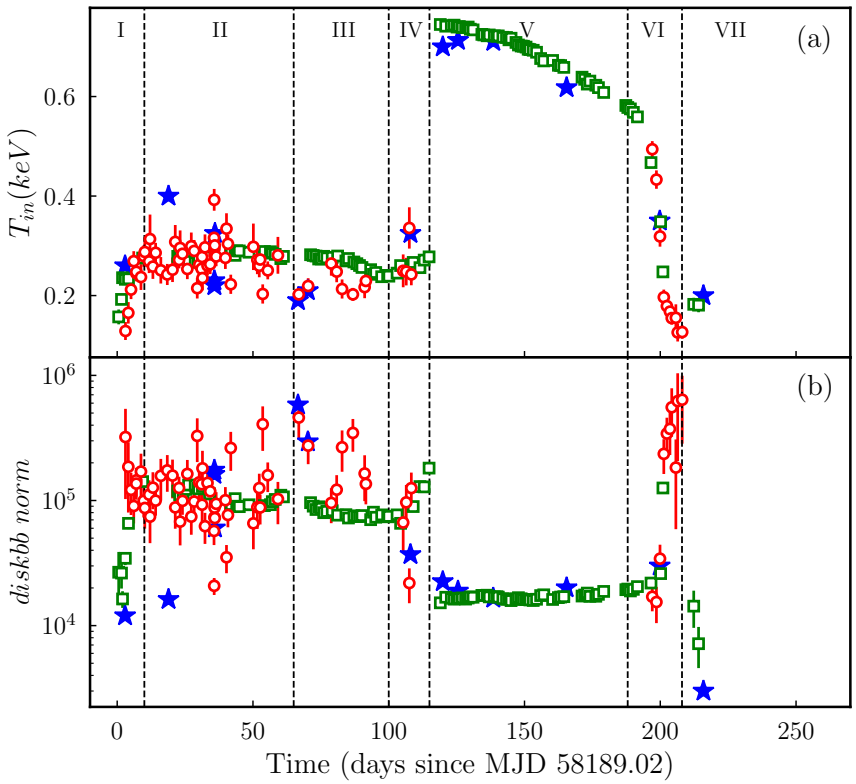

Figure 3.3: Evolution of **(a)** inner accretion disc temperature (T_{in}) and **(b)** disc normalization for *XRT* and *NICER* data. The red circles represent the *XRT* data, and the green squares represent the *NICER* data. The uncertainties are within the 90% confidence range. Different evolutionary phases are marked from I to VII. The star marks represent the values estimated from the wideband spectral analysis using phenomenological models discussed in §3.3.1.

`powerlaw`, `diskbb` and `gauss` (required only for *NICER* data).

The evolution of the `diskbb` parameters, T_{in} and `diskbb norm` are presented in Fig. 3.3a and Fig. 3.3b respectively, estimated from both *XRT* and *NICER* observations. Here, *XRT* data points are marked by red circles and *NICER* by green squares. The uncertainties are within the 90% confidence range. The star marks represent the values estimated from the wideband spectral analysis using phenomenological models discussed in §3.3.1. We see that the `diskbb` component is required to model all observations of Outburst-I (first $\sim$ 100 days). T_{in} is low at the beginning of the outburst and subsequently increases with the accretion of matter in the brief rising phase ($\sim$ 10 days). Both T_{in} and `diskbb norm` remain almost constant (though two parameters from *XRT* data show some random variation) during Phase-II. However, a slow decline (Phase-III) is observed towards the end of Outburst-I. It means that the thermal component does not change much in Phase-II while it is decreasing slowly

(Phase-III) in the decline part of Outburst-I. The `diskbb norm` is directly proportional to the inner radius of the accretion disc, R_{in}. The source is in the LHS during Outburst-I, and the high value of `diskbb norm` indicates that the disc is truncated at a large radius (see also, Zdziarski et al. (2021a,b)).

Around day 100 (MJD 58290), the Outburst-II is triggered, and the source becomes extremely luminous with a very sharp increase of T_{in} ($\sim$ factor of 3) and an order of magnitude decrease in the `diskbb norm`. The source transits to the HSS via a very brief intermediate state. The large value of T_{in} signifies strong accretion activity, and the low value of `diskbb norm` reveals that the inner edge of the accretion disc extends close to the central object. Also, the nearly constant value of the `diskbb norm` during the HSS indicates that R_{in} does not evolve during this period. However, T_{in} gradually decreases along with the decline of the source flux, and the thermal radiation regulates the evolution of the source in this phase. As mentioned earlier, we have ignored the *XRT* observations during this period due to huge pile-up issues and have used only *NICER* data for spectral modelling. As the source returns to the LHS, T_{in} declines to a low value, and eventually, the contribution from the disc becomes insignificant after $\sim$ 210 days (MJD 58400). The outburst ends with the disc truncated again at a large distance, and `diskbb norm` becomes large.

We use a `powerlaw` model to quantify the contribution of the non-thermal component, which is believed to be produced by the inverse-Compton scattering of the disc photons. The evolution of the `powerlaw` model components is shown in Fig. 3.4. The *XRT* and *NICER* data are shown in red circles and green squares, respectively, as before. Fig. 3.4a represents the evolution of photon index (Γ) with time, whereas Fig. 3.4b shows the evolution of `powerlaw` normalization (`norm`). Again the star marks represent the same quantities estimated from the wideband spectral analysis using phenomenological models (see §3.3.1). In LHS, the contribution of Comptonized hard photons is larger than the soft disc photons and therefore, Γ is low (harder spectrum) with a high value of `powerlaw norm`. We noticed two distinct patterns of evolution of the powerlaw component in the LHS. Phase-II shows a gradual increase in Γ (Fig. 3.4a) with a constant `powerlaw norm` (Fig. 3.4b) such that the lightcurve appears as a *plateau* (Fig. 3.1). However, Γ remains constant and a gradual decline of `powerlaw norm` is observed in Phase-III. In both cases, there is a gradual decrease in the non-thermal flux. In the former case, the non-thermal flux is reduced due to the steepening of the spectral index caused by a steady thermal photon flux. In contrast, in the latter case, the non-thermal flux is decreased due to the reduction of thermal photon flux without changing the nature of the non-thermal spectrum. Therefore,

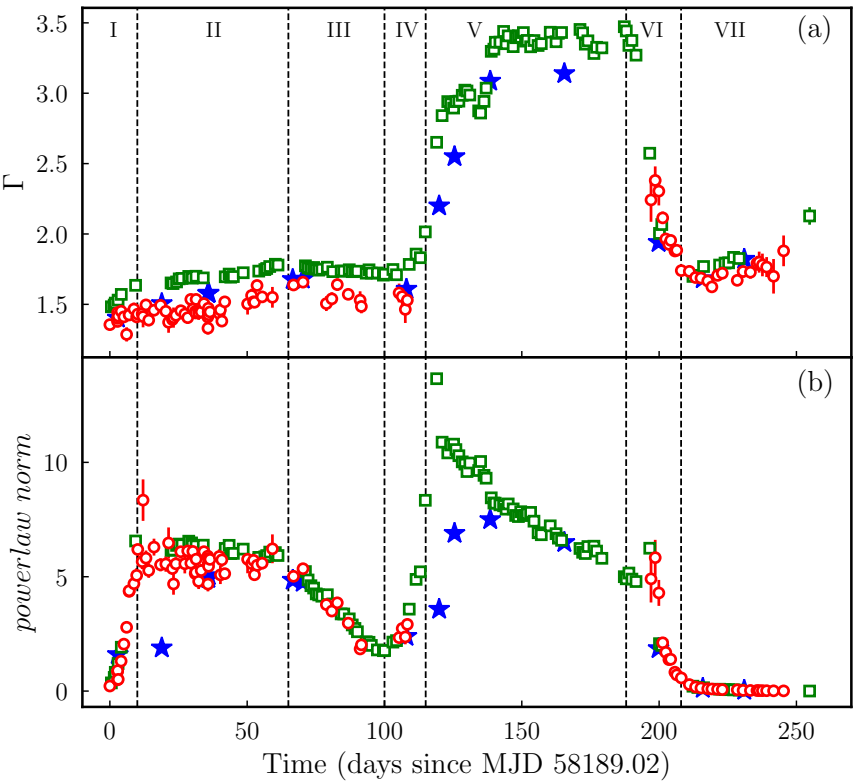

Figure 3.4: The time evolution of **(a)** photon index and **(b)** `powerlaw` normalization for *XRT* and *NICER* data. The red circles represent the *XRT* data, and the green squares represent the *NICER* data. The uncertainties are within the 90% confidence range. Different evolutionary phases are marked from I to VII. The star marks represent the same estimated from the wideband spectral analysis (§3.3.1).

the non-thermal radiation regulates the dynamics in Phase-II, while in Phase-III, both the non-thermal and thermal fluxes change slowly. We noticed that Γ (Fig. 3.4a) measured from *NICER* is higher (∼ 0.24) than that of *XRT* during the LHS (Outburst-I), possibly due to the reasons mentioned in §3.2.2. In Outburst-II, spectrum becomes very soft (Γ > 3) as the source rapidly enters the HSS, and this characteristic is maintained throughout the entire HSS (Phase-V), despite a reduction in the non-thermal flux (`powerlaw norm` reduces) over time. In the declining phase, the source moves through the intermediate state (Γ ∼ 2) and finally reaches the LHS (Phase-VII) with a hard spectrum.

The spectral modelling of *NICER* data shows an excess residual in the 6 – 7 keV range, which is generally assumed to be Fe K_α feature produced due to the reflection of hard photons onto the cold accretion disc. We used a Gaussian profile wherever this feature is visible. The evolution of Fe K_α line energy and the Gaussian normalization estimated using *NICER* data are shown in Fig. 3.5a and Fig. 3.5b, respectively. The star marks show the

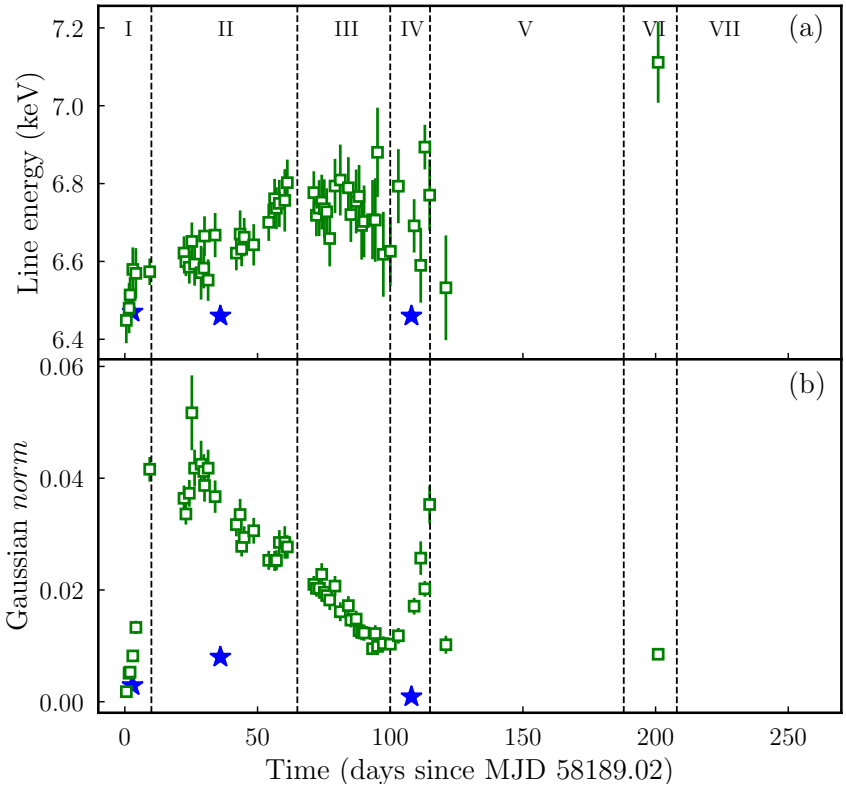

Figure 3.5: Time evolution of **(a)** Gaussian line energy and **(b)** Gaussian line normalization obtained from *NICER* data. The uncertainties are within the 90% confidence range. Different evolutionary phases are marked from I to VII. The star marks represent the parameters estimated from the wideband spectral analysis (§3.3.1).

same quantity obtained from the broadband spectral modelling. The Gaussian line width is frozen at 0.6 keV for some observations, which otherwise give very high values. At the beginning of the outburst, the source is in LHS, and more hard `powerlaw` photons from the corona illuminate the accretion disc surface. We notice an increasing line contribution during the rising phase. Afterwards, a gradual decrease of `powerlaw` photons reduces the amount of reflected radiation. This trend can be visible in Fig. 3.5b. Other factors, such as the slope of the hard photon spectrum from the corona, the ionization of the disc surface, and so on, may also contribute to the observed changes in the iron line profile (Buisson et al., 2019; Kara et al., 2019; Axelsson & Veledina, 2021). The Fe K_α line emission energy is 6.4 keV, but it can vary slightly due to the relativistic effects. Fig. 3.5a displays a systematic increase in the Gaussian line energy, which lies in the range 6.53 – 6.89 keV. In Outburst-II, the source immediately enters the HSS, the disc photons dominate, and no more line features are visible in the spectra. However, the *NICER* observation around ~ 200 day shows a reflection feature at ~ 7.1 keV.

Table 3.2: Simultaneous broadband (*XRT-NuSTAR, NICER-NuSTAR* and *AstroSat*) observations of the source MAXI J1820+070.

Epoch	Obs. ID			
	NuSTAR (MJD)	*XRT* (MJD)	*NICER* (MJD)	*AstroSat* (MJD)
1	90401309002 (58191.94)		1200120103 (58190.99)	
2				9000001994 (58208)
3	90401309013 (58224.95)	00010627042 (58224.87)		
4	90401309013 (58224.95)	00010627043 (58224.95)		
5	90401309014 (58225.28)		1200120131 (58225.03)	
6	90401309019 (58255.60)	00088657004 (58255.90)		
7	90401324002 (58259.24)	00010627062 (58259.35)		
8	90401309021 (58297.17)		1200120189 (58297.19)	
9				9000002216 (58309)
10	90401309025 (58314.75)		1200120207 (58314.19)	
11	90401309027 (58327.05)		1200120220 (58327.89)	
12				9000002324 (58355)
13	90401309033 (58388.91)	00088657010 (58388.92)		
14	90401309037 (58404.95)		1200120277 (58405.20)	
15	90401309039 (58420.05)		1200120290 (58420.05)	

3.3 Simultaneous Wideband Spectral Modelling

To understand the spectral characteristics over a broad range, we performed simultaneous wideband spectral analysis using data from four instruments: *Swift/XRT, NICER, NuSTAR*, and *AstroSat*. We considered all simultaneous or quasi-simultaneous (with a time difference not exceeding 1 hour) observations (*XRT-NuSTAR, NICER-NuSTAR* and *AstroSat SXT-LAXPC*) which are listed in Table 3.2. For each pair, either *XRT* or *NICER* data contributes to the low-energy regime (0.8 – 10 keV), and *NuSTAR* data (4 – 75 keV) contributes to the high-energy regime. For *AstroSat*, we used *SXT* (0.7 – 8 keV) and *LAXPC* (3 – 60 keV) data, respectively for low and high-energy bands. The *SXT* data below 1.3 keV for Obs. ID 9000001994 (Epoch 2 in Table 3.2) shows a high systematic residual, which has also been reported by Chakraborty et al. (2020). Therefore, we used *SXT* data between 1.3 - 7.0 keV for this observation. A temporal filter is applied to extract the spectrum from the *NuSTAR*

data according to the exposure time of the corresponding simultaneous *NICER* or *XRT* data to ensure they are strictly simultaneous. The spectra from both focal plane modules (*FPMA* and *FPMB*) of *NuSTAR* data are fitted together. A normalization constant accounts for the calibration difference, if any, between *FPMA* and *FPMB*.

We consider 15 epochs (5 pairs of *XRT-NuSTAR*, 3 pairs of *AstroSat* and 7 pairs of *NICER-NuSTAR*) of simultaneous observations (Table 3.2) and model them using a combination of phenomenological models and compare the parameters obtained from the spectral modelling of individual *NICER/XRT* data. Also, we modelled the broadband data using reflection models to estimate various parameters such as the BH spin, inclination of the system, accretion disc characteristics, etc. The n_H value is fixed at $1.5{\times}10^{21}\mathrm{cm}^{-2}$, same as the *NICER/XRT* spectral modelling (§3.2.1). *AstroSat/LAXPC* data show an instrumental feature $\sim$ 30 keV due to Xe K fluorescence X-rays since the detector is filled with a mixture of xenon and methane (Antia et al., 2017, 2021; Sreehari et al., 2019). Additional absorption `edges` address this instrumental feature of *LAXPC*. Brief descriptions of various models used for data modeling in *XSPEC* are discussed in §2.3.

3.3.1 Wideband Phenomenological Spectral Modelling

We attempted to model the *XRT-NuSTAR, NICER-NuSTAR* and *AstroSat* observations using a combination of the phenomenological models `diskbb` and `nthcomp` with a motivation to estimate the temperature of the corona and exponential cut-off, if any. But we could neither constrain the electron temperature nor the cut-off energy. Therefore, we continue to model the broadband data with `diskbb` and `powerlaw` to maintain consistency with the spectral modelling of individual *NICER/XRT* data. We also used components like `gauss` and `smedge` if required. The estimated parameters are presented in Table 3.3 and marked with star symbol in Fig. 3.3,3.4,3.5.

The `diskbb` parameters are consistent with *NICER/XRT*, though Epoch 2 (*AstroSat*) records a higher T_{in} and lower `diskbb norm` than *NICER/XRT*. Epoch 1 – 8 and Epoch 14 – 15 in Table 3.3 belong to the LHS, and the estimated `powerlaw` index is consistent with the same from *XRT* data alone (Fig. 3.4a). Epoch 9 – 12 corresponds to the HSS, and the estimated Γ ($\lesssim 3$) is significantly harder than that estimated from the *NICER* data (Fig. 3.4a). During Epoch 13, the source possibly transited through an intermediate state with $\Gamma = 1.94^{+0.01}_{-0.02}$. Additional *Gaussian* component is required for three broadband (Epoch 1, 5 & 8 in Table 3.3) observations and the line parameters differ significantly from that of *NICER* data (Fig. 3.5).

Table 3.3: Spectral parameters of simultaneous broadband X-ray data (*XRT-NuSTAR, NICER-NuSTAR* and *AstroSat*) fitted with phenomenological models. The *XRT-NuSTAR* pairs and *AstroSat* observations are highlighted with dark-grey and pale-grey colours, respectively; others are *NICER-NuSTAR* pairs. The uncertainties are within the 90% confidence range.

Epoch	diskbb		gauss			smedge		powerlaw		χ^2_{red}
	T_{in} (*keV*)	*norm* ($\times 10^4$)	*line E* (*keV*)	*sigma* (*keV*)	*norm* (*photons/cm^2/s*)	*edge E* (*keV*)	*width* (*keV*)	Γ	*norm* (*photons/keV/cm^2/s*)	
1	$0.26^{+0.01}_{-0.01}$	$1.2^{+0.3}_{-0.3}$	$6.47^{+0.04}_{-0.04}$	$0.25^{+0.05}_{-0.05}$	$0.0029^{+0.0006}_{-0.0005}$	$6.57^{+0.08}_{-0.09}$	$8.9^{+2.4}_{-1.7}$	$1.403^{+0.002}_{-0.002}$	$1.6^{+0.4}_{-0.3}$	1.17
2	$0.391^{+0.003}_{-0.002}$	$1.62^{+0.09}_{-0.13}$	—	—	—	$8.1^{+0.3}_{-0.3}$	$3.8^{+0.4}_{-0.9}$	$1.506^{+0.009}_{-0.001}$	$4.37^{+0.06}_{-0.06}$	1.43
3	$0.23^{+0.01}_{-0.01}$	$17.5^{+6.9}_{-4.8}$	—	—	—	$7.24^{+0.09}_{-0.09}$	$3.7^{+0.8}_{-0.6}$	$1.578^{+0.003}_{-0.003}$	$4.93^{+0.03}_{-0.03}$	1.33
4	$0.22^{+0.02}_{-0.02}$	$16.2^{+8.3}_{-5.3}$	—	—	—	$7.2^{+0.1}_{-0.1}$	$3.7^{+0.8}_{-0.6}$	$1.578^{+0.003}_{-0.003}$	$4.94^{+0.03}_{-0.03}$	1.28
5	$0.325^{+0.003}_{-0.003}$	$6.04^{+0.2}_{-0.2}$	$6.46^{+0.03}_{-0.03}$	$0.28^{+0.03}_{-0.03}$	$0.0083^{+0.0008}_{-0.0008}$	$7.33^{+0.06}_{-0.06}$	$3.2^{+0.4}_{-0.3}$	$1.580^{+0.001}_{-0.001}$	$5.05^{+0.01}_{-0.01}$	1.89
6	$0.19^{+0.01}_{-0.01}$	$58.2^{+28.9}_{-18.6}$	—	—	—	$7.2^{+0.1}_{-0.1}$	$4.4^{+1.6}_{-1.1}$	$1.677^{+0.004}_{-0.004}$	$4.85^{+0.04}_{-0.04}$	1.06
7	$0.21^{+0.01}_{-0.01}$	$29.5^{+10.7}_{-7.6}$	—	—	—	$7.2^{+0.2}_{-0.2}$	$4.8^{+2.4}_{-1.5}$	$1.68^{+0.01}_{-0.01}$	$4.76^{+0.04}_{-0.04}$	1.10
8	$0.325^{+0.002}_{-0.002}$	$3.7^{+0.1}_{-0.1}$	$6.46^{+0.04}_{-0.04}$	$0.12^{+0.05}_{-0.05}$	$0.0009^{+0.0002}_{-0.0002}$	$7.33^{+0.04}_{-0.04}$	$5.1^{+0.5}_{-0.4}$	$1.608^{+0.001}_{-0.001}$	$2.395^{+0.006}_{-0.006}$	1.55
9	$0.7^{+0.6}_{-1.1}$	$2.25^{+0.03}_{-0.02}$	—	—	—	$7.58^{+0.07}_{-0.07}$	$16.5^{+0.6}_{-1.1}$	$2.20^{+0.01}_{-0.01}$	$3.58^{+0.09}_{-0.08}$	1.7
10	$0.713^{+0.001}_{-0.001}$	$1.89^{+0.02}_{-0.02}$	—	—	—	$6.87^{+0.06}_{-0.05}$	$14.3^{+3.2}_{-3.1}$	$2.55^{+0.02}_{-0.01}$	$6.9^{+0.2}_{-0.2}$	1.42
11	$0.711^{+0.001}_{-0.001}$	$1.66^{+0.02}_{-0.02}$	—	—	—	$6.76^{+0.08}_{-0.08}$	$13.9^{+0.9}_{-0.4}$	$3.086^{+0.006}_{-0.017}$	$7.5^{+0.2}_{-0.2}$	1.09
12	$0.618^{+0.002}_{-0.002}$	$2.01^{+0.04}_{-0.04}$	—	—	—	$8.9^{+0.4}_{-0.3}$	$8.84^{\dagger}$	$3.14^{+0.02}_{-0.02}$	$6.5^{+0.2}_{-0.2}$	1.80
13	$0.35^{+0.01}_{-0.01}$	$3.0^{+0.4}_{-0.3}$	—	—	—	$7.8^{+0.2}_{-0.2}$	$13.87^{\dagger}$	$1.94^{+0.01}_{-0.02}$	$1.86^{+0.05}_{-0.05}$	1.03
14	$0.20^{+0.02}_{-0.02}$	$0.3^{+0.2}_{-0.1}$	—	—	—	—	—	$1.683^{+0.009}_{-0.009}$	$0.124^{+0.003}_{-0.003}$	0.97
15	—	—	—	—	—	—	—	$1.821^{+0.006}_{-0.006}$	$0.0383^{+0.0006}_{-0.0005}$	1.00

†Parameter uncertainty can't be estimated.

This is because *NuSTAR* has a broad coverage to capture the reflection features and has a better energy resolution in this range. Inclusion of *NuSTAR* data results in constraining the `gauss` line energy and width (Table 3.3). We also notice an absorption edge (6.75 – 9.3 keV) in all the simultaneous data except Epochs 14 and 15 (towards the quiescent state). It possibly indicates a significant amount of hard X-ray irradiation during the outbursts.

3.3.2 Spectral Modelling for Reflection Features

There are studies related to the reflection features in the spectra of MAXI J1820+070 on a selected number of observations using various flavours of reflection models (Buisson et al., 2019; Chakraborty et al., 2020; Buisson et al., 2021; Marino et al., 2021; You et al., 2021; Kawamura et al., 2022). We performed broadband spectral modelling using a few flavours of the relativistic reflection model *RELXILL*, discussed in §2.3.2.

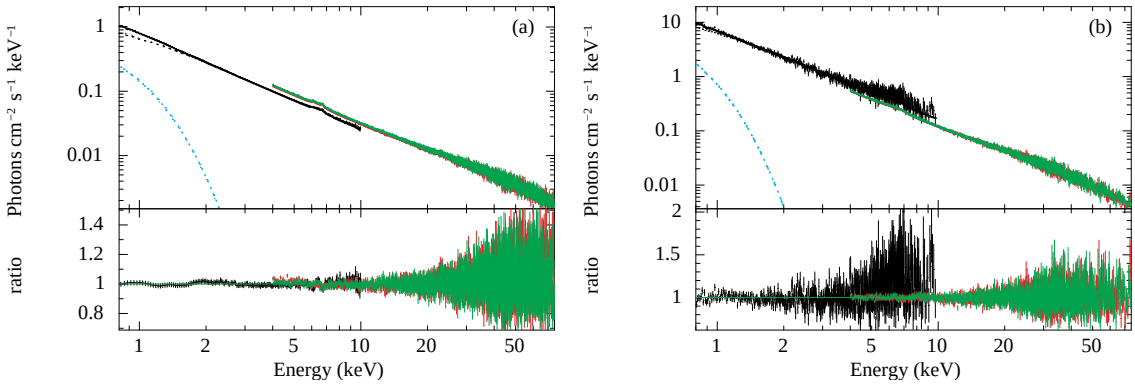

Figure 3.6: **(a)** Simultaneous *NICER-NuSTAR* observation on MJD 58191 (Epoch 1 in Table 3.2) fitted using the model `tbabs(diskbb+relxilllpCp)`. Black represents *NICER* data, and red and green for *NuSTAR FPMA* and *FPMB*, respectively. **(b)** Quasi-Simultaneous *XRT-NuSTAR* observation on MJD 58224 (Epoch 3 in Table 3.2) fitted using the model `tbabs(diskbb+relxilllpCp)`. Black represents *XRT* data, and red and green for *NuSTAR FPMA* and *FPMB*, respectively. The `diskbb` and reflection components are shown in light blue and black dotted lines, respectively.

We used a combination of `diskbb` and `relxilllpCp` models to fit the data except for Epoch 9 – 12. During these four epochs in the HSS, `relxilllpCp` model did not produce a good fit, and the value of a few parameters became unphysical. However, `relxilllp` provided a better spectral fitting. The fitted broadband spectra of simultaneous *NICER-NuSTAR* (Epoch 1) and *XRT-NuSTAR* (Epoch 3) observations using reflection modelling are shown in Fig. 3.6a and Fig. 3.6b, respectively. We used the model `tbabs(diskbb+relxilllpCp)` to fit the data for both cases. Black represents the *XRT*

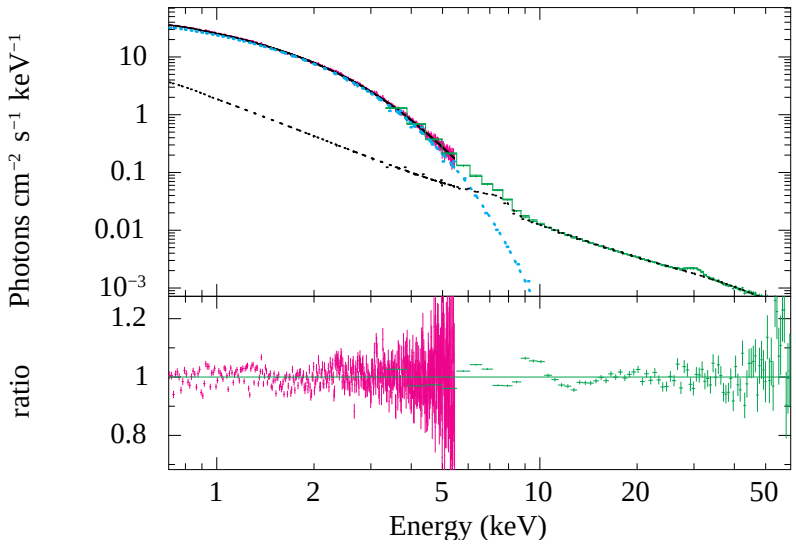

Figure 3.7: Broadband energy spectrum of *AstroSat* observation (Epoch 9) is best fitted with the model `tbabs(diskbb+relxilllp)`. The *SXT* and *LAXPC* data are plotted in magenta and green, respectively. The `diskbb` and reflection components are shown in light blue and black dotted lines, respectively.

data in Fig. 3.6a and *NICER* data in Fig. 3.6b, whereas red and green represent *NuSTAR FPMA* and *FPMB*, respectively. Fig. 3.7 represents the *AstroSat* observation (Epoch 9) fitted with the model `tbabs(diskbb+relxilllp)`. *SXT* and *LAXPC* data are shown in magenta and green, respectively. A thermal disc component is needed for the low-energy data. Note that in phenomenological modelling (§3.3.1), the reflection features are managed by a `gauss` component at $\sim$ 6.4 keV and `smedge` component at $\sim$ 7 keV for most of the epochs. On the other hand, reflection features such as the iron line, edge and Compton hump are self-consistently calculated in the `RELXILL` model.

Similarly, all the pairs in Table 3.2 are fitted with RELXILL models. The important parameters are estimated and summarised in Table 3.4, while other parameters are frozen at their default values. The uncertainties are within the 90% confidence range. The inner disc temperature, T_{in} and photon index, Γ estimated for each epoch from phenomenological (Table 3.3) and reflection modelling (Table 3.4) are generally agreed well. However, T_{in} estimated from reflection modelling is marginally lower, and Γ is slightly higher. A possible reason could be that the soft excess from the reflection model contributes to lower energy, reducing the temperature of the `diskbb` component. Also, the primary spectrum may become marginally softer since the reflection reduces the number of hard X-ray primary photons.

Table 3.4: Spectral parameters of simultaneous broadband *XRT-NuSTAR, NICER-NuSTAR* and *AstroSat* observations fitted using RELXILL group of models. The highlighted rows indicate the same as in Table 3.3. The uncertainties are within 90% confidence range.

Epoch	`diskbb`		`relxilllpCp`								χ^2_{red}
	T_{in} (*keV*)	*norm* ($\times 10^4$)	h (GM/c^2)	θ (*deg*)	Γ	$\log \xi$ ($erg\ cm\ s^{-1}$)	A_{Fe} ($A_{Fe,\odot}$)	R_f	kT_e (*keV*)	*norm* ($\times 10^{-2}$)	
1	$0.237^{+0.007}_{-0.002}$	$1.59^{+0.2}_{-0.2}$	$202.25^{+159.01}_{-64.2}$	$63.0^{\dagger\dagger}$	$1.553^{+0.003}_{-0.001}$	$2.01^{+0.08}_{-0.06}$	$2.4^{+0.1}_{-0.1}$	$0.39^{+0.01}_{-0.01}$	$100.0^{\dagger\dagger}$	$5.9^{+0.1}_{-0.1}$	1.09
2	$0.33^{+0.02}_{-0.02}$	$2.3^{+0.6}_{-0.5}$	$100.0^{\dagger\dagger}$	$63.0^{\dagger\dagger}$	$1.54^{+0.01}_{-0.01}$	$3.70^{+0.07}_{-0.04}$	$4.4^{+2.5}_{-0.8}$	$0.7^{+0.2}_{-0.3}$	$100.0^{\dagger\dagger}$	$16.5^{+2.8}_{-1.7}$	1.46
3	$0.17^{+0.02}_{-0.02}$	$44.6^{+51.8}_{-22.5}$	$29.46^{+10.36}_{-9.55}$	$56.9^{+9.6}_{-7.0}$	$1.72^{+0.01}_{-0.01}$	$1.69^{\dagger}$	$2.4^{+0.3}_{-0.3}$	$0.6^{+0.2}_{-0.1}$	$116.67^{\dagger}$	$18.2^{+1.5}_{-0.9}$	1.20
4	$0.17^{+0.02}_{-0.02}$	$47.1^{+53.6}_{-27.0}$	$30.44^{+6.88}_{-4.84}$	$59.8^{+4.3}_{-3.7}$	$1.73^{+0.01}_{-0.01}$	$1.70^{+0.05}_{-0.09}$	$2.3^{+0.4}_{-0.1}$	$0.61^{+0.14}_{-0.09}$	$100.0^{\dagger\dagger}$	$17.6^{+0.8}_{-0.7}$	1.14
5	$0.296^{+0.002}_{-0.003}$	$7.02^{+0.5}_{-0.4}$	$30^{\dagger}$	$63.0^{\dagger\dagger}$	$1.729^{+0.002}_{-0.003}$	$1.70^{+0.01}_{-0.02}$	$2.14^{+0.09}_{-0.06}$	$0.67^{+0.01}_{-0.01}$	$100.0^{\dagger\dagger}$	$18.0^{+0.1}_{-0.1}$	1.13
6	$0.16^{+0.01}_{-0.01}$	$105.9^{+100.4}_{-53.7}$	$23.1^{+4.5}_{-3.3}$	$63.0^{\dagger\dagger}$	$1.808^{+0.004}_{-0.004}$	$1.70^{+0.02}_{-0.03}$	$2.7^{+0.4}_{-0.2}$	$0.65^{+0.02}_{-0.03}$	$100.0^{\dagger\dagger}$	$13.7^{+0.2}_{-0.3}$	1.08
7	$0.17^{+0.01}_{-0.01}$	$58.4^{+22.9}_{-21.6}$	$23.1^{+5.5}_{-4.6}$	$63.0^{\dagger\dagger}$	$1.82^{+0.01}_{-0.01}$	$1.70^{+0.02}_{-0.04}$	$2.7^{+0.5}_{-0.2}$	$0.67^{+0.06}_{-0.03}$	$100.0^{\dagger\dagger}$	$13.2^{+0.3}_{-0.2}$	1.11
8	$0.306^{+0.003}_{-0.001}$	$4.0^{+0.2}_{-0.1}$	$20.3^{+0.6}_{-1.2}$	$63.0^{+0.4}_{-0.6}$	$1.741^{+0.001}_{-0.001}$	$1.699^{+0.003}_{-0.003}$	$2.81^{+0.05}_{-0.07}$	$0.59^{+0.03}_{-0.02}$	$100.0^{\dagger\dagger}$	$8.57^{+0.05}_{-0.03}$	1.52
9*	$0.710^{+0.002}_{-0.002}$	$1.91^{+0.04}_{-0.03}$	$3.0^{+0.5}_{-0.5}$	$63.0^{\dagger\dagger}$	$2.32^{+0.02}_{-0.03}$	$3.09^{+0.04}_{-0.03}$	$10.0^{\ddagger}$	$3.6^{+0.3}_{-0.2}$	—	$14.8^{+8.8}_{-4.4}$	1.58
10*	$0.7398^{+0.001}_{-0.001}$	$1.67^{+0.02}_{-0.02}$	$2.0^{\ddagger}$	$63.0^{\dagger\dagger}$	$2.57^{+0.01}_{-0.01}$	$3.31^{+0.02}_{-0.01}$	$7.9^{+1.1}_{-1.5}$	$3.10^{+0.27}_{-0.03}$	—	$125.3^{+9.0}_{-1.1}$	1.19
11*	$0.7198^{+0.001}_{-0.001}$	$1.67^{+0.003}_{-0.003}$	$2.23^{+0.04}_{-0.02}$	$59.9^{+0.3}_{-0.4}$	$3.273^{+0.003}_{-0.050}$	$2.70^{+0.01}_{-0.02}$	$10.0^{\ddagger}$	$3.8^{+0.1}_{-0.1}$	—	$424.5^{+126}_{-4.6}$	1.28
12*	$0.691^{+0.002}_{-0.002}$	$0.55^{+0.01}_{-0.01}$	$2.69^{+0.45}_{-0.45}$	$63.0^{\dagger\dagger}$	$3.12^{+0.01}_{-0.01}$	$4.3^{+0.06}_{-0.06}$	$10.0^{\ddagger}$	$3.59^{+0.37}_{-0.37}$	—	$15.8^{+1.0}_{-1.0}$	1.37
13	$0.35^{+0.01}_{-0.01}$	$2.38^{+0.4}_{-0.4}$	$11.25^{+3.65}_{-2.26}$	$63.0^{\dagger\dagger}$	$2.07^{+0.02}_{-0.02}$	$1.7^{+0.2}_{-0.1}$	$4.7^{+0.4}_{-0.7}$	$0.8^{+0.1}_{-0.1}$	$100.0^{\dagger\dagger}$	$3.9^{+0.5}_{-0.2}$	1.10
14	—	—	$8.6^{\dagger}$	$63.0^{\dagger\dagger}$	$1.73^{+0.01}_{-0.01}$	$2.8^{+0.1}_{-0.1}$	$1.4^{+0.7}_{-0.5}$	$0.38^{+0.05}_{-0.04}$	$54.34^{\dagger}$	$0.5^{+0.2}_{-0.1}$	1.0
15	—	—	$3.03^{\dagger}$	$63.0^{\dagger\dagger}$	$1.84^{+0.01}_{-0.01}$	$1.7^{+0.2}_{-0.6}$	$5.0^{+2.4}_{-1.2}$	$0.38^{+0.07}_{-0.07}$	$100.0^{\dagger\dagger}$	$0.38^{+0.003}_{-0.004}$	0.98

* HSS where `relxilllp` model is used instead of `relxilllpCp`. Here, kT_e is not a parameter and `norm` is the `relxilllp` normalization.

†Parameter uncertainty can't be estimated. ††Frozen parameter. ‡Parameter hits the boundary.

The spin parameter a_* is found to be pegged near the highest allowed limit. Therefore we freeze $a_* = 0.998$. Bhargava et al. (2021) predicted the BH spin of MAXI J1820+070 as $0.799^{+0.016}_{-0.015}$ using timing study, but they expected an underestimation in the calculation, and this value should be regarded as a lower limit. Therefore, the high-spin approximation used in our study is justified. The inclination angle, θ, of the system has been estimated to be 63° (Atri et al., 2020). Through reflection modeling, we were able to estimate the inclination angle for a few observations (Epoch 3, 4, 8, and 11). For the remaining observations, we freeze $\theta = 63°$ since we were unable to constrain it from the fitting. The inner radius of the accretion disc R_{in} is frozen at R_{ISCO} and the outer radius R_{out} is frozen at the default value (400 r_g). In most cases, the electron temperature in the corona $k_B T_e$ is hitting the upper boundary. Therefore, in such cases, we freeze it to a more reasonable value of 100 keV. We used lamp-post height h, inclination angle θ, photon index of the incident radiation Γ, ionization parameter log ξ, iron abundance (A_{Fe}) of the accretion disc, and reflection fraction R_f as the free parameters.

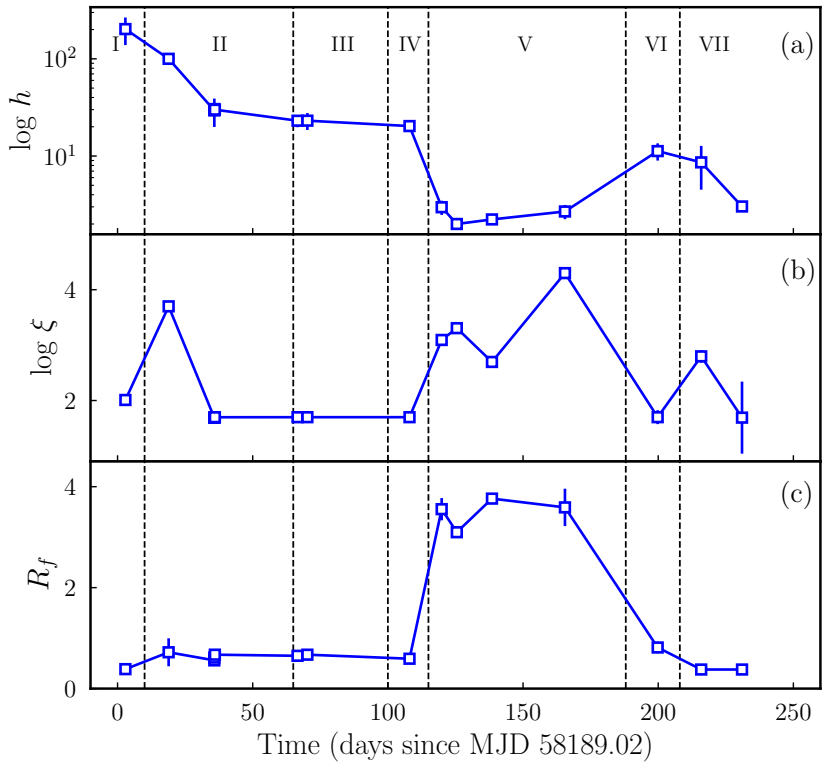

Figure 3.8: Evolution of the reflection parameters: **(a)** lamp-post height (h), **(b)** ionization parameter (log ξ) and **(c)** reflection fraction (R_f) obtained from simultaneous wideband spectral study. Different evolutionary phases are marked from I to VII.

The evolution of the reflection parameters is shown in Fig. 3.8. The number of primary

source photons illuminating the disc increases in the rising phase of the outburst, and hence the ionization (log ξ) (Fig. 3.8b) of the disc material increases. As a result, the amount of reflection, R_f, increases during the rising phase of Outburst-I. Therefore, R_f shows a positive correlation with the luminosity of the source in the hard state (Atri et al., 2020). During Phase-II, the lamp-post height, log ξ, and R_f decrease from the rising phase, whereas these parameters remain steady in Phase-III. R_f shows a slight decrease for Epoch 8 (Phase-IV), which is the very beginning of the second outburst and has a lower flux. However, You et al. (2021) considered a lamp-post corona for the hard state of MAXI J1820+070 and reported an unusual decreasing trend in the reflection fraction due to the effect of the bulk motion of the corona. We are considering a point-like static lamp-post corona, where this effect is not coming into the picture. Thermal reverberation lags (De Marco et al., 2021) showed that the relative distance between the primary photon source and the disc decreases as the source softens.

Dauser et al. (2016) found that reflection is strong for low source height (h) and high inclination angle. In the HSS (Phase-V in Fig. 3.8), we observed that the corona is close to the central object with a high reflection fraction $R_f \sim 3.5$, a high ionization parameter (log $\xi \sim 4$) and an over-abundance of iron (A_{Fe}). Buisson et al. (2019) and Bharali et al. (2019) also reported the chances of overestimation of A_{Fe}. The decline phase (Epoch $13 - 15$) shows a reduction of ionization and reflection fraction. The lamp-post height shows a momentary increase (Epoch 13) when the hard flux takes over the soft flux and then declines as the source becomes faint. Thus, the broadband reflection modelling indicates the presence of a dynamically evolving corona (with the lamp-post height changing) during both outbursts except in the HSS.

3.4 Timing Analysis of MAXI J1820+070

For the timing analysis (see §2.4) of MAXI J1820+070, we consider all the *NICER* data of the source and the three available *AstroSat/LAXPC* observations during the period of study. We generated lightcurves for *NICER* observations with more than 1 ks exposure, with a bin size of 3 ms in the full energy range. We did not subtract any background from the lightcurve and we generated PDS using the tool `powspec`. The PDS are Poisson noise subtracted (Zhang et al., 1995) and normalized to squared RMS fractional variability. For Outburst-I, we rebinned the *NICER* data such that f_{min} = 0.01 Hz and f_{max} = 55.55 Hz. A geometrical rebinning factor of -1.09 is applied. For Outburst-II, particularly for the soft state data, we prefer a larger bin size to get good statistics, therefore, we have f_{min} = 0.001

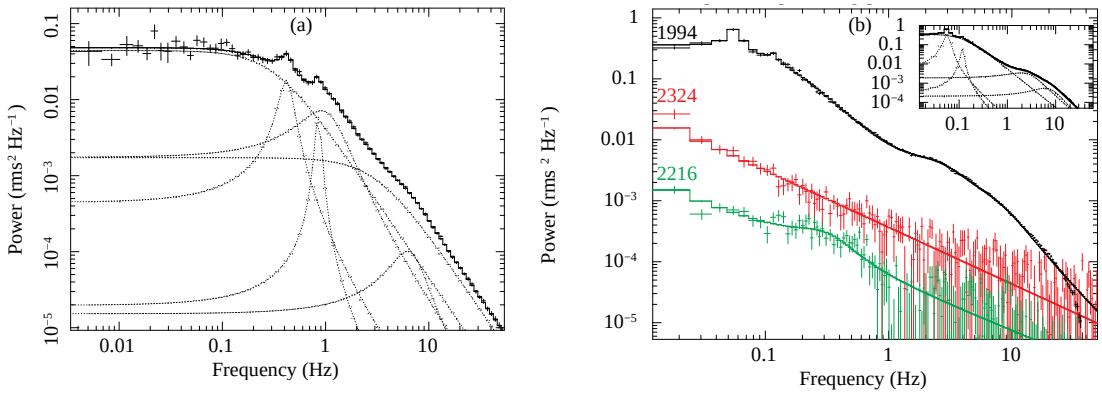

Figure 3.9: Representation of PDS for (a) *NICER* observation on day 56.43, fitted using multiple Lorentzian components, and (b) *AstroSat* observations are shown. Three *AstroSat* observations on Epochs 2, 9, 12 (Table 3.2) are plotted in black, green, and red colours, respectively. The Lorentzian components for Epoch 2 are shown in the inset.

Hz and f_{max} = 2.564 Hz. Here, we rebin the PDS with a geometrical rebinning factor of -1.2. For *AstroSat/LAXPC* data, we created lightcurves with a time resolution of 0.1 s in the 3 – 60 keV energy band. The PDS is geometrically rebinned by a factor of -1.03. For the observation ID 9000002216 (Epoch 2, in Table 3.2), the PDS is generated only from segments 10-19 since the other segments have low exposure time.

We used XSPEC to model the PDS, as discussed in §2.4.1. The broadband noise features in the PDS are modelled with zero-centred `Lorentzian` and a combination of `Lorentzian` to identify the QPOs or QPO-like features. We also used powerlaw components for fitting the PDS in the HSS observations since the PDS are almost featureless. A typical example of fitted PDS for *NICER* observations on day 56.43 is shown in Fig. 3.9a. The feature at ν_c=$0.42^{+0.01}_{-0.02}$ Hz is a QPO with Q-factor 3.19 ± 1.4, significance 2.3 and fractional RMS (in percentage) is 5.9 ± 0.6. In Fig. 3.9b, we present PDS of the *AstroSat* observation IDs 9000001994 (Epoch 2), 9000002216 (Epoch 9), and 9000002324 (Epoch 12) in black, green, and red colours respectively. Various Lorentzian components for ID 9000001994 are shown in the inset. A QPO is detected at $0.05^{+0.002}_{-0.001}$ Hz with a Q-factor of 4.1 ± 0.7, the significance of 9.1 and fractional RMS of 9.1 ± 0.3 (in percentage) only during Epoch 2 of *AstroSat* observations.

The detection of QPOs in this source in X-rays has been investigated in previous literature (Buisson et al., 2019; Mudambi et al., 2020; Homan et al., 2020; Stiele & Kong, 2020; Ma et al., 2021). Buisson et al. (2018) reported QPOs with evolving frequency ($0.036^{+0.002}_{-0.002}$ to $0.428^{+0.004}_{-0.036}$ Hz) in the LHS of MAXI J1820+070. Homan et al. (2020) reported a QPO type switching, from type-C to type-B (rapidly became 4.5 Hz then decreased to 3 Hz) during

(MJD 58305.67 to MJD 58305.81) the LHS to HSS transition followed by a strong radio flare detection which provides the connection between them. Ma et al. (2021) observed LFQPOs above 200 keV in the LHS using *Insight-HXMT* observations, and such a high-energy LFQPO has not been observed before in black hole binaries. They found an increase in frequency from 0.02 Hz (MJD 58194) to 0.51 Hz (MJD 58257) was observed, followed by a decrease to 0.22 Hz (MJD 58286). Here, we study the evolution of the total fractional

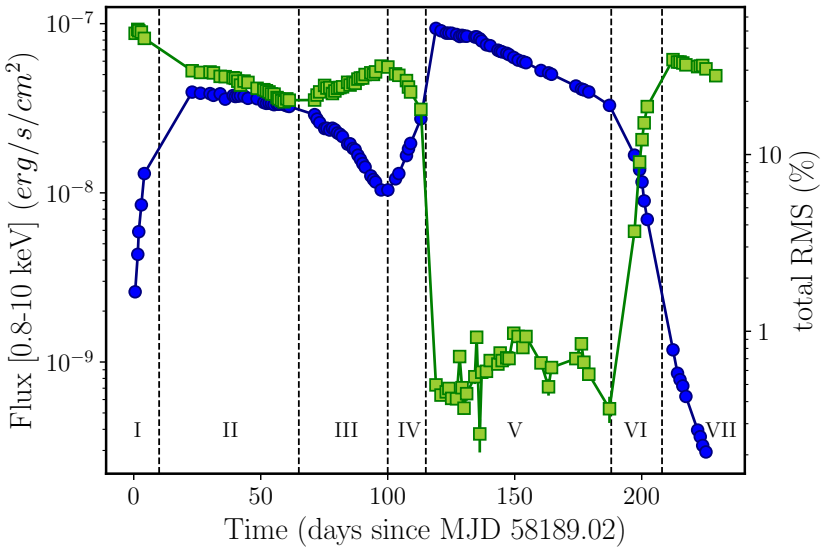

Figure 3.10: The time evolution of the total RMS (green square) and the flux in 0.8−10 keV (blue dot) is shown for all the *NICER* observations. Different evolutionary phases are denoted from I through VII.

RMS power in the PDS and the characteristic frequency (ν_c), and the RMS of QPO or QPO-like features. Also, we study the dependency of RMS with the QPO characteristic frequency. Finally, we present the RID and HRD, which can be used to track the behaviour of the BH transient throughout the outburst and provide fundamental information regarding the system.

3.4.1 Evolution of total RMS and Characteristic Frequency

We calculate the total RMS (in percentage) in the PDS and present their variation (green squares) over the outbursts in Fig. 3.10. We also plot the evolution of *NICER* 0.8−10 keV flux in blue dots. Different evolutionary phases of the system are denoted from I through VII. Both quantities show an anti-correlation throughout the period, except for Phase-II.

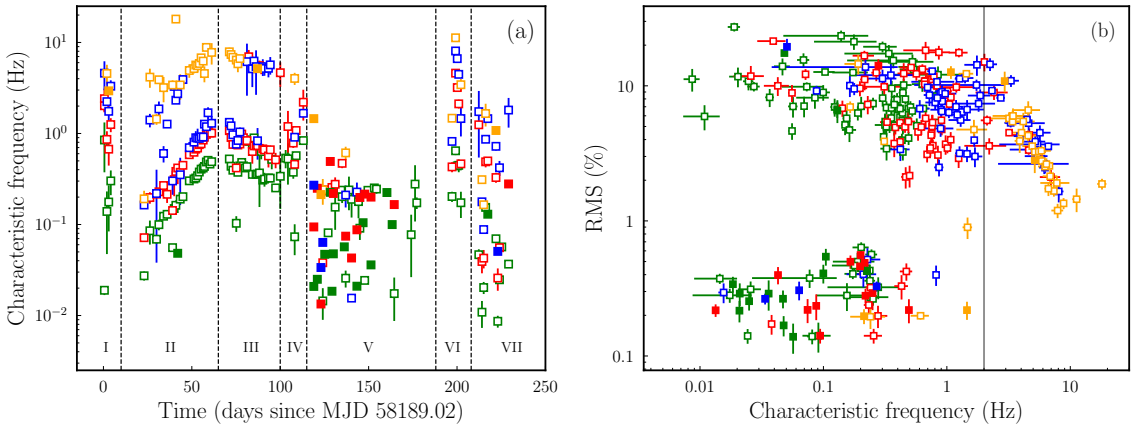

Figure 3.11: (a) Time evolution of the characteristic frequency (ν_c) of different Lorentzian features corresponding to each *NICER* observation. The first four Lorentzian of each PDS, in the increasing order of ν_c, are indicated using green, red, blue and orange colours, respectively. Different evolutionary phases are marked from I to VII. **(b)** The variation of fractional RMS (in percentage) under Lorentzian with the characteristic frequency for the first four Lorentzian of *NICER* observations are presented with the colour scheme. The ν_c whose uncertainty can't be estimated are shown using filled boxes.

The evolution of ν_c for different `Lorentzian` features (say, QPO-like features) used in each *NICER* observation is shown in Fig. 3.11a. We have plotted the first four `Lorentzian` of each observation in the increasing order of the value of ν_c, indicated using green, red, blue, and orange colours, respectively. We could not estimate the uncertainty in ν_c for a few observations, shown using filled squares. The characteristic frequency of all these `Lorentzian` features increases with time in Phase-II though the overall flux decreases (Fig. 3.1). This is contrary to the general understanding that as the source moves in the LHS, the changes in ν_c of the `Lorentzian` features are correlated with the source flux (Belloni, 2010). However, the behaviour of ν_c in Phase-III is expected as the source flux gradually declines in the LHS. The presence of type-C QPO is observed in both Phase-II and Phase-III. We discuss the possible physical scenarios to understand the evolution of ν_c in §3.5. In the HSS (Phase-V), the PDS is almost featureless and is fitted using weak `Lorentzian` and `powerlaw` components. In this state, the `Lorentzian` components have lower ν_c than the previous state and no QPO is observed. During the decay towards the LHS (Phase-VII) in Outburst-II, ν_c shows a similar trend as in Phase-III, which is expected in the LHS.

The fractional RMS (%) under each QPO-like feature is calculated and plotted against ν_c in Fig. 3.11b. The same colour scheme (as in Fig. 3.11a) is followed. The figure shows some interesting characteristics. Two clustering can be distinguished here; one is at the

top-right, corresponding to the LHS with higher values of RMS, and the other is at the bottom-left, representing the HSS with very low RMS. The fractional RMS shows a clear anti-correlation with QPO frequency $\nu_c > 2$ Hz (marked with a vertical line), generally observed in the LHS. However, no clear correlation is observed at the lower frequency.

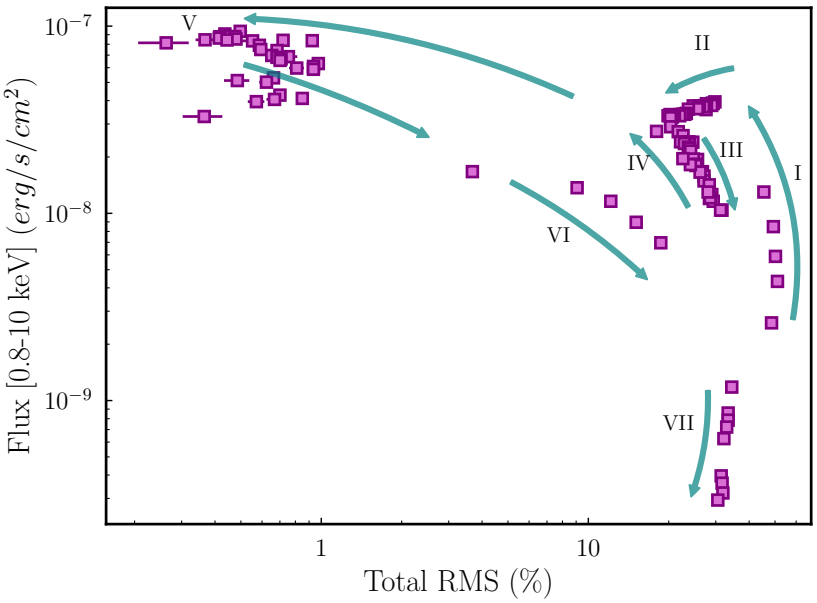

Figure 3.12: RID: The flux versus total RMS (in percentage) is presented with various phases identified as in Fig. 3.1 to understand the trend of evolution.

3.4.2 RMS-Intensity Diagram (RID)

Fig. 3.12 shows the flux ($0.8-10$ keV) versus total fractional RMS with various evolutionary phases marked (I−VII). The arrow marks indicate the evolution track of the system. We can see the anti-correlation between the flux and RMS throughout this plot except in Phase-II, where RMS decreases with a decrease in flux. However, in Phase-VII, flux decreases at a constant RMS. It shares a similar pattern as in HID (Fig. 3.2).

The flux is very low at the beginning of the outburst (Phase-I), and the total fractional RMS is greater than 40%. The flux then increases suddenly and reaches Phase-II. In this phase, RMS decreases to 20% due to spectral softening. Therefore, the hard photons contribute to both the reduction of RMS and flux. The RMS increases to $\sim 30\%$ in Phase-III since there is no spectral softening due to the reduction in thermal flux. The spectral state transition to HSS (Phase-V) takes place very fast, and RMS drops to the lowest possible value. The flux declines gradually (Phase-V), and the source has a low RMS ($< 1\%$) in this

state. The flux then decreases faster (Phase-VI) and reaches the quiescent state (VII) as the outburst ends. At the same time, RMS increases quickly and stays constant.

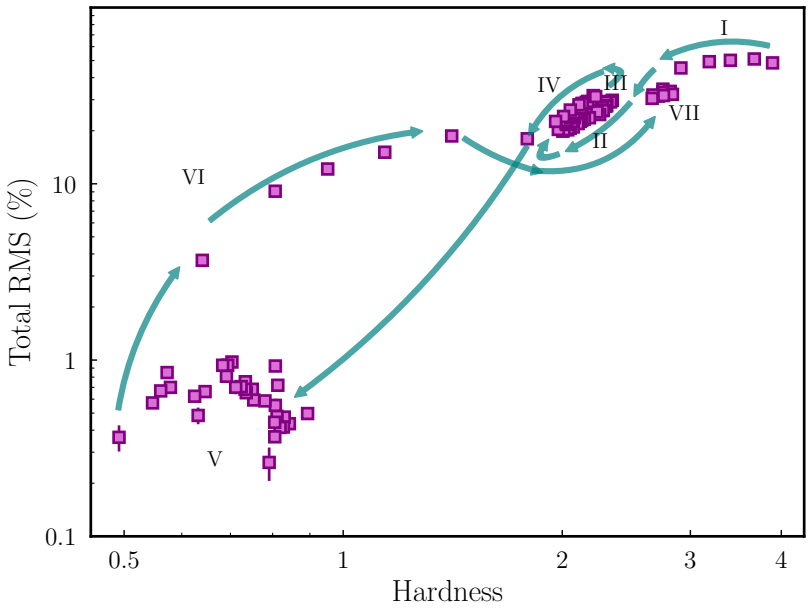

Figure 3.13: Hardness-RMS diagram (HRD) for the *NICER* observations. Total fractional RMS corresponds to the frequency range 0.02 – 40 Hz in the full energy range and is plotted against hardness.

3.4.3 Hardness-RMS Diagram (HRD)

Total fractional RMS versus hardness (*Hardness-RMS diagram*) is shown in Fig. 3.13. This figure represents an overall combination of spectral and temporal characteristics. The evolutionary track is marked from I to VII as before.

The outburst starts (Phase-I) with a high value of hardness and the total fractional RMS $> 40\%$, but as it proceeds, hardness decreases along with the RMS, and the source enters into Phase-II where RMS decreases to 20%. Here, both quantities are correlated due to the spectral softening. Then RMS increases slightly in Phase-III with a very little change in the hardness. Outburst-I ends here, spanning almost a linear region with higher values of HR and RMS. During the HSS (Phase-V), there is a significant variation in the hardness with approximate constant ($< 1\%$) RMS. Phase-VI possibly shows a transition in the intermediate state as there are significant variations in HR and RMS. Still, no high-frequency variability in the lightcurve is observed to confirm it. Finally, the source returns to the quiescence with high HR and RMS. The Outburst-II spans a wider parameter space in HRD and completes

a figure-eight shaped hysteresis loop.

3.5 A Possible Accretion Scenario

We attempt to understand the accretion scenario of MAXI J1820+070 during the 2018 outburst using standard accretion disc (Shakura & Sunyaev, 1973) picture. We find from the spectral modelling of *NICER* data (Fig. 3.3b) that the minimum value of `diskbb norm` is, $N_d \sim 1.5 \times 10^4$ during the HSS of Outburst-II. The corresponding inner disc radius of the `diskbb` model is $r_{in} = D_{10}\sqrt{N_d/\cos(\theta)}$ (§2.3.1b), where, D_{10} is the distance to the source in 10 kpc, θ is the inclination of the system in degree and r_{in} is in km. By setting $\theta = 63^\circ$ and $D_{10} = 2.96$ kpc (Atri et al., 2020), the value of r_{in} is calculated as 122 km and it is consistent with the true inner radius $R_{in} \sim R_{ISCO} = 0.44\,\kappa^2\,r_{in}$ (Kubota et al., 1998) of a Schwarzschild BH of mass $8.5 M_\odot$ (Torres et al., 2020) with $\kappa = 1.7$. This shows that the accretion disc has reached close to the ISCO during the HSS of Outburst-II. Outburst-I starts with low $T_{in} \sim 0.15$ keV (Fig. 3.3a) and $N_d \sim 1.6 \times 10^4$ (Fig. 3.3b). The flux reaches its peak just in 10 days. Notice that N_d is very similar to the value during the HSS, and hence R_{in} is close to the ISCO. Therefore, both outbursts start close to the central object and have a shorter rise time.

The generally accepted disc instability model (Osaki, 1974; van Paradijs & McClintock, 1994; Lasota, 2001) suggests that an outburst can be triggered due to the thermal-viscous instability when the temperature of the disc crosses the hydrogen ionization temperature (see §1.5). The instability raises the disc's temperature, forming a hot propagating ionizing front which enhances the accretion of matter. An outburst can be triggered either at the outer part of the accretion disc (outside-in) or the inner part (inside-out). Since the accretion happens at the viscous timescale, the outside-in trigger will have a longer rise time ($\sim 50-100$ days), whereas the inside-out trigger produces an outburst of shorter rise time ($\sim 10-20$ days). Most of the outbursts of GX 339-4 are examples of the former category (Aneesha et al., 2019) whereas that of GRO J1655-40 and H1743-322 belong to the second class (Aneesha & Mandal, 2020) of outbursts.

The observed short rise time and low R_{in} are indicative of an inside-out triggering mechanism for the source MAXI J1820+070. Therefore, the hot ionizing front moves outward, pushing the disc outward (N_d increases sharply, Fig. 3.3b) with an enhancement of T_{in} (Fig. 3.3a) due to a surge in accretion rate, $T_{in} \propto \dot{M}^{1/4} R_{in}^{-3/4}$ (Equation 1.17). During the decay phases (Phase-II, III), the accretion rate continues to decline with a very slow inward movement of the disc, keeping the disc temperature approximately constant. The

disc is truncated in the range $13 - 18\ r_g$ and a similar conclusion is drawn by Zdziarski et al. (2021a) using *Insight-HXMT, NuSTAR* and *INTEGRAL* data.

At around $\sim$ 100 days (Phase-IV), one more inside-out triggering (Outburst-II) takes place, and the subsequent 20 days are a repetition of the rising phase of Outburst-I. But the difference is that Outburst-I has been triggered from quiescence (low T_{in}), whereas the second triggering has happened when the disc is sufficiently hot ($T_{in} = 0.28$ keV). Therefore, the accretion process is more dramatic, particularly in the last 5 days of the rising phase. The disc becomes so hot (T_{in} increase by a factor of 2.6) that the viscous timescale is reduced and the R_{in} approaches (reduce by a factor of 3.5) R_{ISCO} in just 5 days. The soft flux under the `diskbb` component at the peak of the Outburst-II is 5×10^{-8} erg/cm^2/s, and it corresponds to a luminosity of 5.3×10^{37} erg/s for an assumed distance of 2.96 kpc (Atri et al., 2020). It means the source is accreting only at the 5% of its Eddington accretion rate ($\dot{M}_{Edd} = 1.2 \times 10^{19}$ gm/s) with an assumed mass of $8.5 M_{\odot}$ (Torres et al., 2020) and 10% accretion efficiency. Even though the source has a low accretion rate, the system appears very bright due to proximity and low column density along the line of sight. An inside-out triggering is expected to result in a low-luminosity outburst due to the limited size of the disc in the hot state, as predicted by Lasota (2001). The source continues to be in the HSS with approximately no change in R_{in}, whereas T_{in} continues to decrease due to the decline of the accretion rate. Finally, the disc becomes cooler once the accretion of hot matter is over and the source reaches the quiescence.

The broadband spectral study using reflection modelling (§3.3.2) reveals the presence of a dynamical corona in the LHS (Phase-II and Phase-III), while the inner disc remains truncated and evolves marginally. Therefore, the evolution of spectral and timing properties in this state are regulated by the dynamical evolution of the corona. Fig. 3.11a shows that the characteristic frequency of QPOs, ν_c, increases with time in Phase-II but decreases with time in Phase-III. Among the few possible physical scenarios for the origin of LFQPOs, Stella et al. (1999); Motta et al. (2018) and Ingram & Motta (2019) proposed Lense-Thirring precession of inner accretion can be an effective mechanism. The lense-Thirring precession mechanism required a misalignment of $\gtrsim 5^{\circ}$ between the BH spin axis and the binary orbital plane (Ingram & Motta, 2019; Miller-Jones et al., 2019). Poutanen et al. (2021) recently reported a misalignment of at least 40° between the black hole spin and the orbital angular momentum of MAXI J1820+070. Also, the inner radius of the disc needs to be dynamic to produce the QPO evolution with time. That means R_{in} has to move inward and outward during Phase-II and Phase-III, respectively. However, we understand from the spectral modelling (§3.2.1 and §3.3) that the R_{in} decreases marginally ($R_{in} \sim 13 - 18 r_g$) during the

LHS (Phase-II and III). Done et al. (2007) suggested that R_{in} derived from `diskbb norm` using simple spectral models such as `diskbb + powerlaw` may not always be reliable. This is because the standard disc theory demands a zero-torque boundary condition at the inner edges of the accretion disc (Shakura & Sunyaev, 1973). On the other hand, the `diskbb` model assumes a non-zero torque at the inner edge of the disc. However, other studies in the literature support the truncated disc geometry and dynamic corona in the LHS of this source. For example, Kara et al. (2019) and Wang et al. (2020) used reverberation time lags between the emission from the corona and the irradiated accretion disc and suggested a contracting corona in the LHS rather than a changing inner radius of the accretion disc. Buisson et al. (2019) and You et al. (2021) also arrived at a similar conclusion using reflection modelling of the *NuSTAR* data. Similarly, Zdziarski et al. (2021a) performed reflection modelling of *HXMT, NuSTAR* and *INTEGRAL* data and suggested $R_{in} > 10\ r_g$ in the LHS. Also, Zdziarski et al. (2021b) supported the presence of a truncated disc using thermal Comptonization and reflection modelling of *NuSTAR* and *INTEGRAL* data. Therefore, the Lense-Thirring precession of inner accretion flow cannot explain the evolution of the QPO frequency of the source completely.

However, the other competing picture for the origin of LFQPO is the propagation of shock oscillation model (Molteni et al., 1996; Chakrabarti et al., 2004, and reference therein). Here, oscillation of the 'hot' corona due to the resonance between the cooling timescale and the local dynamical timescale can produce LFQPOs. During Phase-II, the supply of soft photons remains steady as the disc is not evolving. Therefore, the photon number in the corona is approximately constant (`powerlaw norm` remains constant, Fig. 3.4b). The soft photons will cool the electrons in the corona, and a slow but steady spectral softening takes place. It reduces the cooling timescale of the electrons in the corona. If the LFQPOs are produced due to the resonance between the cooling timescale and the local dynamical timescale, the QPO frequency will increase with time. On the other hand, in Phase-III, the number of thermal photons decreases gradually, increasing the cooling timescale, and hence a reverse evolution is observed. Note that in Phase-II, the inverse-Comptonization of soft photons in the 'hot' corona is significantly high as the soft photon source remains steady. The hard photons lag behind the soft photons due to the inverse-Comptonization effect. The reflection modelling (Fig. 3.8a) shows that the corona is dynamic and moving closer to the central source in Phase-II. It means that the size of the corona becomes smaller, and optical depth decreases in this phase. In an optically thin medium, the inverse-Compton spectral index is $\Gamma = -\ln \tau / \ln A$ (Rybicki & Lightman, 1979), where τ is the optical depth and A is the mean amplification factor per scattering. The decrease of optical depth or/and reduction

of amplification factor due to cooling can cause spectral softening observed in Phase-II. In the former case, considering A to be constant, the number of scatterings required to produce a high-energy photon remains constant. The soft photon stays longer inside the corona due to an increased mean free path. In the second case, assuming a constant mean free path, the number of scatterings required to produce a high-energy photon increases as A reduces, and the soft photon spends a longer time inside the corona. The physical situation is possibly a combination of both effects mentioned above. Therefore, spectral softening is associated with the increase of hard lag in Phase-II, as Wang et al. (2020) reported. However, in Phase-III, the soft photons flux decreases gradually, spectra become slightly harder due to a reduction of cooling, and the hard lag decreases (Wang et al., 2020). Also, we have seen in Phase-II, the size of the corona decreases (Fig. 3.8a) as the local dynamical timescale decreases and a reverse trend is expected in Phase-III. However, it is difficult to determine if the corona moves outward based on only two closely spaced simultaneous data points in Phase-III (Fig. 3.8a).

The geometry of the corona is generally described either as vertically elongated (Martocchia & Matt, 1996; Uttley et al., 2014; Niedźwiecki et al., 2016) or radially extended (Chakrabarti & Titarchuk, 1995; Wilkins & Gallo, 2015; Poutanen et al., 2018). We understand that the reflection modelling of the broadband spectral data supports a vertically elongated corona. In contrast, the evolution of LFQPO caused by the propagation of the shock oscillation model suggests a radially extended corona inside the truncated disc. The comprehensive spectral and timing studies suggest a complex geometry of the corona (Fürst et al., 2015; Niedźwiecki et al., 2016; Wilkins et al., 2016; Gonzalez et al., 2017; Zoghbi et al., 2020) in the LHS of the source. It demands further investigation of the coronal geometry, which is beyond the scope of the present work.

3.6 Summary and Conclusion

We independently performed spectral analysis of *NICER* and *Swift/XRT* data (§3.2.1) during Outburst-I and Outburst-II. The lightcurve of the source obtained from the *NICER* and *XRT* data shown in Fig. 3.1, reveals two successive outbursts during the period of study. The Outburst-I is dominated by the non-thermal photons (peak flux in $2-10$ keV is 2.4 times higher than that in the in $0.8-2$ keV), whereas the Outburst-II is very bright and soft. The same trend from simultaneous broadband spectral modelling is found in $10-60$ keV (filled star in Fig. 3.1). The HID with different spectral states is presented in Fig. 3.2. The Outburst-I is evolved only in the LHS and classified as a 'failed-transition' outburst,

whereas the Outburst-II shows a transition from LHS to HSS via a very brief intermediate state. There is an overall offset ($\sim$ 22%) in the HR between *XRT* and *NICER* due to the difference in the spectral responses (discussed in Appendix-A). We have done broadband spectral modelling of all available simultaneous data of *NICER-NuSTAR, XRT-NuSTAR* and *AstroSat* (*SXT-LAXPC*) to understand the presence of various model components (§3.3.1) in the spectra. Also, the broadband reflection modelling (§3.3.2) shows the presence of a strong reflection signature during both outbursts and an evolving corona in the LHS. The timing analysis shows multiple QPO-like features, and we have studied the time evolution of their characteristic frequency (Fig. 3.11a). We find a clear anti-correlation between the fractional RMS and ν_c (Fig. 3.11b) for $\nu_c > 2$ Hz. This is a signature of type-C QPO and is commonly observed in LHS (Belloni, 2010; Athulya et al., 2022). However, no clear correlation is observed at the lower frequency. Below, we summarise the important findings of this work, combining the spectral and timing studies during various phases of the evolution of the source.

- **Phase-I (Rising phase, Outburst-I)**
  Fig. 3.3 and Fig. 3.4 show that both thermal and non-thermal flux increases in the rising phase with an increase of T_{in} and `powerlaw norm` with a hard spectrum ($\Gamma \sim 1.5$). The *NICER* and *NuSTAR* data show the presence of Fe K_α line (Fig. 3.5 and Epoch 1 in Table 3.3) and the presence of significant reflection. The lamp-post height is significantly large ($\sim 200 r_g$) with a high ionization parameter ($\log \xi = 2.01^{+0.08}_{-0.06}$) and iron abundance $A_{Fe} = 2.4 \pm 0.1$. PDS show the presence of QPO-like features in $0.1 - 5$ Hz (Fig. 3.11a) and the fractional RMS $\sim$ 40% (Fig 3.12).

- **Phase-II**
  In this phase, the thermal disc component is very steady with $T_{in} \sim 0.27$ keV (Fig. 3.3a) and R_{in} evolves very little ($15 - 18 r_g$). The non-thermal photon flux remains steady with the gradual spectral softening (Fig. 3.4a). We observe the reflection signature of Fe K_α line (Fig. 3.5) with an increasing trend in the line energy and absorption edge (Epoch $2 - 5$ in Table 3.3). The reflection modelling (Epoch $2 - 5$ in Table 3.4) of broadband data shows a gradual decrease of lamp-post height to $\sim 30 r_g$ with an enhancement in the reflection fraction $R_f \sim 0.6$. The disc iron abundance remains similar to the rising phase, but there is a reduction in the ionization parameter ($\log \xi \sim 1.7$). The timing results show that the characteristic frequency (ν_c) increases with time from $\sim$ 0.1 to 10 Hz (Fig. 3.11a) as the flux decreases. This is generally not

observed in outbursting sources. As discussed in §3.5, one possible reason could be the spectral softening due to the reduction of the cooling timescale of electrons in the corona as the thermal component remains steady. And the resonance oscillation between the cooling timescale and dynamical timescale produces the LFQPOs (Molteni et al., 1996; Chakrabarti et al., 2004). The spectral softening leads to a correlated reduction of the fractional RMS (Phase-II in Fig. 3.12) with the observed flux. The RMS lies in the 30 – 20% range with a reduction in HR in this phase (Fig. 3.13).

- **Phase-III**

  A steady decrease in the thermal and non-thermal components of flux is observed in this phase. A steady decrease in T_{in} (Fig. 3.3a) and `powerlaw norm` (Fig. 3.4b) is observed without any spectral softening ($\Gamma \sim 1.7$). The *NICER* data possess a reflection signature of Fe K_α line (Fig. 3.5). The wideband spectral study shows the presence of Fe absorption edge (Epoch 6-7 in Table 3.3). The reflection parameters (Fig. 3.8) are similar to the previous phase. We observed that the characteristic frequencies (ν_c) in the PDS decreases (Fig. 3.11a) with time. The total fractional RMS increases with the decrease in flux (Phase-III in Fig. 3.12), which is consistent with the general characteristics in the LHS. This is due to the overall decrease in the number of photons in the corona, and it becomes difficult to cool it further. The RMS increases to 30% with almost constant HR (Fig. 3.13) since thermal and non-thermal flux decrease similarly.

  After this, the source moves to Outburst-II through a rising phase (Phase-IV) similar to Outburst-I. The simultaneous broadband data show the reflection signature (Fig. 3.8) with similar parameters as in Phase-II. The characteristic frequency, ν_c, increases with time (Fig. 3.11a) as flux increases. Both fractional RMS and HR reduce, and the source moves to the HSS very fast.

- **Phase-V (HSS, Outburst-II)**

  The thermal emission flux dominates the spectrum in this state. The disc moves close to the inner edge with $T_{in} \sim 0.7$ keV (Fig. 3.3a), and the spectrum becomes very soft, $\Gamma > 3.0$ (Fig. 3.4a), though simultaneous spectral modelling (Epoch 9-12) in Table 3.3 and Table 3.4 provide a relatively lower index. The *NICER* data do not show any Fe line signature though simultaneous broadband data show high reflection fraction $R_f \sim 3.5$, high ionization parameter ($\log \xi \sim 4$), and over-abundance of iron. The

timing properties show featureless PDS with very low RMS (Phase-V in Fig. 3.12) and HR varies between $\sim 0.5 - 0.7$ (Fig. 3.13).

- **Phase-VI & VII (Decay towards quiescence)**
  The lightcurve in the decline phase of Outburst-II is initially linear and becomes exponential towards the end. T_{in} decreases (Fig. 3.3a), R_{in} gradually move outward and the spectrum becomes harder (Fig. 3.4a). The reflection modelling (Fig. 3.8) shows that the reflection fraction and the lamp-post height decrease gradually. Fig. 3.11a shows that ν_c increases at the end of the HSS and decreases with the declination of the flux. The spectro-temporal properties indicate that this phase passes through the intermediate state (Phase-VI in Fig. 3.13) with a fractional RMS of 10% and HR ~ 1. In the end, the source returns to the LHS (Phase- VII in Fig. 3.13) with RMS of $\sim$ 30% and HR of ~ 3.

Finally, we discuss the possible accretion scenario during the 2018 outburst in §3.5. We propose that both outbursts are triggered as inside-out propagation of thermo-viscous instability, producing outbursts with a short rise time. The spectral modelling shows that the Outburst-I has been triggered close to the inner edge, and the disc remains truncated. The rise of flux in Outburst-II is dramatic since the outburst triggering has happened when the disc is sufficiently hot, and the viscous timescale becomes short enough that the inner disc moves close to ISCO very fast and produce bright HSS. The accretion disc remains truncated ($\sim 10\ r_g$) once the source reaches the quiescence. The comprehensive spectral and timing studies reveal that a lamp-post corona or a radially extended corona is inadequate to interpret the observed data. The results suggest a complex corona geometry in the LHS of MAXI J1820+070. The outcome of this study challenges the present understanding of coronal geometry and suggests further investigation of disc-jet geometry around black holes.

Chapter 4

Wideband Study of the Brightest Black Hole X-ray Binary 4U 1543−47 in the 2021 Outburst

We aim for a detailed analysis of the wideband spectral and timing characteristics of the 2021 outburst using three instruments *NICER*, *NuSTAR* and *AstroSat*. We carry out wideband phenomenological and reflection modelling of the data and attempt to understand the accretion scenario of the source during this period. Also, we perform a timing analysis using all three instruments. This chapter is based on our publication in *MNRAS* Prabhakar et al. (2023).

4.1 4U 1543−47: Properties

4U 1543 − 47 is a BH-XRB, discovered by *Uhuru* satellite in 1971 (Matilsky et al., 1972). Since its discovery, the source has undergone five outbursts; the first four are in an interval of ∼ 10 years, in 1984 (Kitamoto et al., 1984), in 1992 (Harmon et al., 1992), and in 2002 (Park et al., 2004). After a gap of 19 years, the fifth outburst happened in 2021 (Negoro et al., 2021a), which marks the source as the brightest BH-XRB with a peak X-ray intensity of 11 Crab in 2 − 4 keV of *MAXI/GSC* (Negoro et al., 2021b). The 2002 outburst was also brighter (4 Crab in 2 − 12 keV), while the previous three outbursts have comparable intensities (Park et al., 2004). Its optical counterpart, IL Lupi, was discovered by Pedersen (1983). The central engine is a dynamically confirmed BH with a mass of 9.4 ± 1.0 $M_{\odot}$, and the companion is an A2V star of mass 2.45 ± 0.15 $M_{\odot}$ (Russell et al., 2006). It is located at at a distance of 7.5 ± 0.5 kpc (Jonker & Nelemans, 2004), its coordinates are RA=$15^h47^m8^s.27$, Dec=$-47°40'10''.8$ (J2000) (Park et al., 2004). Orosz (2003) estimated

the orbital inclination of the system as 20.7° ± 1.5°. Multiple attempts were made to estimate the BH's spin (a_*) in 4U 1543 − 47 using *RXTE* observations of the 2002 outburst. Shafee et al. (2006) estimated a spin of ∼ 0.75 − 0.85 using continuum-fitting of *RXTE* data. Miller et al. (2009) and Morningstar & Miller (2014) estimated the spin value as 0.3 ± 0.1 and $0.43^{+0.22}_{-0.31}$ respectively using relativistic disc reflection and disc continuum modelling. These three estimations are based on a BH mass of 9.4 ± 1.0 $M_\odot$ and a distance of 7.5 ± 0.5 kpc. Shafee et al. (2006) and Morningstar & Miller (2014) used the binary inclination (θ) of 20.7 ± 1.5 degree, while Miller et al. (2009) used a θ of 32^{+3}_{-4} degree for the spin estimation. Dong et al. (2020) reported a spin of $0.67^{+0.15}_{-0.08}$ and θ of $36.3^{+5.3}_{-3.4}$ degree by reflection modelling of *RXTE* data using the model RELXILL. However a recent study by Draghis et al. (2022) determined the spin of the BH to be $0.98^{+0.01}_{-0.02}$ and θ to be 68^{+3}_{-4} degrees by reflection modelling of *NuSTAR* data from the 2021 outburst.

The Giant Metrewave Radio Telescope (*GMRT*) detected radio flares from the source in 2002 outburst (Park et al., 2004). Multiple flaring occasions are reported at different phases of the outburst. Russell et al. (2020) reported the presence of a compact jet in the SIMS of the 2002 outburst of 4U 1543 − 47 using multiwavelength observations (X-ray, optical, IR, and radio). Russell et al. (2020) tested the chances of jet contribution to the luminosity of the system and renounced that possibility.

4.2 Observations

We perform the present study based on the 2021 outburst of 4U 1543 − 47 using *NuSTAR, NICER* and *AstroSat* observations over a period from 17 June 2021 (MJD 59382) to 14 September 2021 (MJD 59471). We consider simultaneous *NICER-NuSTAR* and *AstroSat* observations in this period. The list of observations is given in Table 4.1, which comprises 10 *NuSTAR* and 6 *AstroSat* observations. Seven *NICER* epochs with simultaneous *NuSTAR* coverage are also listed. Therefore, total of 13 simultaneous observations (7 *NICER-NuSTAR* and 6 *AstroSat*) are studied. The first two *AstroSat* observations are having an offset of 40′ since the source was too bright to have pointed observation (Garg et al., 2021), while the other four are pointed observations. Also, we perform timing studies using all the *AstroSat/LAXPC*, *NuSTAR*, and *NICER* observations with exposure time > 500 sec.

Table 4.1: The list of observations (*NuSTAR*, *NICER* and *AstroSat*) of 4U 1543 – 47 considered in this study.

Epoch	Obs. ID			Exposure
	NuSTAR (MJD)	*NICER* (MJD)	*AstroSat* (MJD)	ksec
1	80702317002 (59382.42)	4655060101 (59382.44)		1.15(Nu), 5.25(Ni)
2	80702317004 (59389.47)	4655060201 (59389.47)		2.95(Nu), 1.55(Ni)
3			T04_018T01_9000004494[b] (59396.04)	39.2
4	80702317006 (59396.18)	4655060301 (59396.19)		3.88(Nu), 2.42(Ni)
5	80702317008 (59403.02)	4655060401 (59403.04)		3.71(Nu), 6.11(Ni)
6			T04_021T01_9000004526[b] (59405.36)	36.6
7			T04_030T01_9000004588[c] (59421.19)	17.9
8[a]	90702326002 (59421.67)			3.94
9	90702326004 (59428.18)	4202230143 (59428.13)		6.73(Nu), 0.89(Ni)
10			T04_035T01_9000004622[c] (59430.59)	69.1
11[a]	90702326006 (59450.19)			7.79
12[a]	90702326008 (59455.55)			3.63
13			T04_046T01_9000004680[c] (59457.06)	117.9
14			T04_051T01_9000004686[c] (59461.05)	55.2
15	90702326010 (59465.67)	4202230166 (59466.07)		6.00(Nu), 1.72(Ni)
16	90702326012 (59471.51)	4202230171 (59471.43)		5.34(Nu), 1.02(Ni)

[a] Standalone *NuSTAR* observations.
[b] Offset observations.
[c] Pointed observations.

4.3 Outburst Profile and Hardness ratio

During the 2021 outburst of 4U 1543 – 47, the flux reached the peak value within a few days of the commencement of the outburst, which is monitored by multiple X-ray instruments. The *MAXI/GSC*[1] daily lightcurve of the outburst is generated for two different energy bands, 2 – 10 keV and 10 – 20 keV and are plotted in Fig. 4.1. The MJD 59370 (05 June 2021) is defined as day 0 throughout the study, and according to this, the outburst continued for

[1] `http://maxi.riken.jp/mxondem/`

a duration of ∼175 days. The lightcurve reveals that the source is extremely luminous in low-energies with a very high count rate (Fig. 4.1a). In contrast, the contribution to the luminosity in the high-energy band (Fig. 4.1b) is an order of magnitude lower. The highest flux value in the 2 – 10 keV band is 32.67 photons/s/cm^2 (∼ 10 Crab) on day 9, whereas the same in 10 – 20 keV is just 0.19 photons/s/cm^2 (∼ 0.5 Crab). The source flux reached 11.65 Crab in 2 – 4 keV, the highest value observed among the BH-XRBs. We define hardness

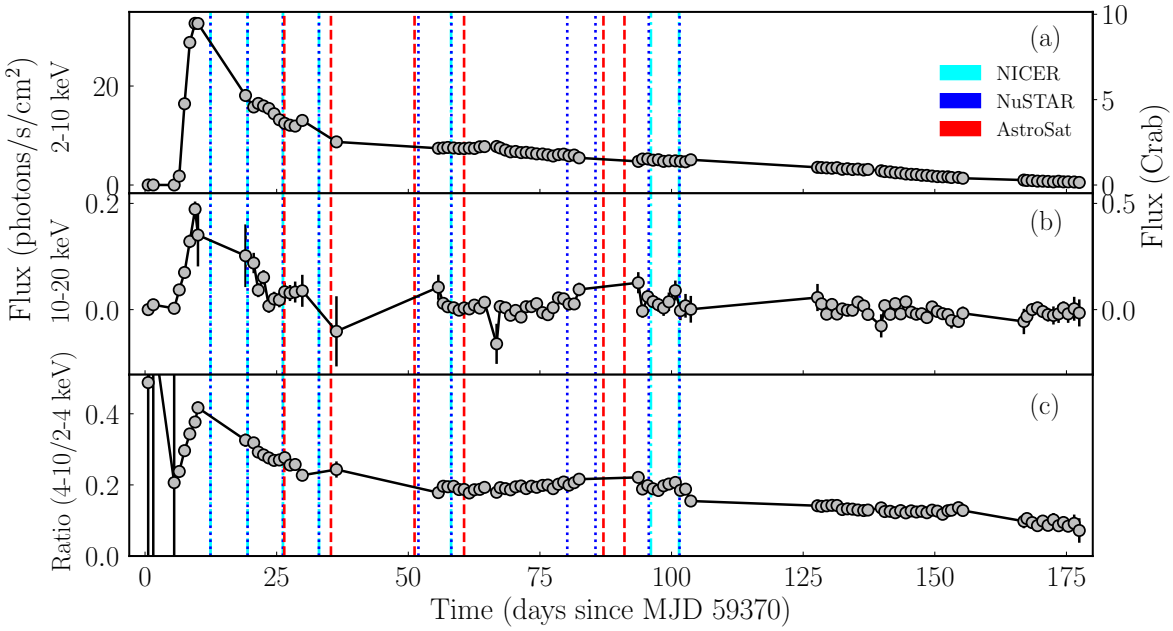

Figure 4.1: *MAXI/GSC* daily average lightcurve in the energy bands **(a)** 2 – 10 keV and **(b)** 10 – 20 keV with flux in units of photons/s/cm^2 and Crab in the left and right Y-axes respectively. The hardness ratio **(c)** is defined by the flux in 4 – 10 keV to 2 – 4 keV. The *NICER, NuSTAR* and *AstroSat* observations are marked using lines with cyan, blue and red, respectively.

(HR) as the ratio of flux in 4 – 10 keV to 2 – 4 keV since beyond 10 keV, the contribution is significantly low. The HR evolution (Fig. 4.1c) shows that the source mostly remains in the soft state during the outburst. The *NICER, NuSTAR* and *AstroSat* observations are marked with dashed lines in cyan, blue and red, respectively. There are no simultaneous broadband observations in the rising phase of the outburst.

4.4 Wideband Spectral Study

The data reduction methodology, the grouping of spectra, and instrumental systematics are discussed in §2.2. This outburst was extremely bright, and *NICER* suffered telemetry

saturation. Therefore, the number of active detectors were reduced, and we corrected the effective area while extracting the scientific products. Similarly, *AstroSat/SXT* data also suffers pileup issues as discussed in §2.2. We studied the spectral properties of the 2021 outburst of 4U 1543−47 from day 12 (MJD 59382) to day 101 (MJD 59471). We carried out phenomenological and reflection modelling of simultaneous observations (*NICER-NuSTAR* and *AstroSat*) listed in Table 4.1 to understand the nature of the broadband spectrum. The *NICER* data below 0.8 keV shows large residuals; hence we ignored it. Therefore, we used the spectra in the energy range 0.8 – 10 keV for *NICER* and 4 – 60 keV for *NuSTAR*. Spectra from both *FPMA* and *FPMB* telescopes of *NuSTAR* give similar results. Hence we present only the *FPMA* spectra throughout the study. We used *SXT* spectra in the energy range 0.5 – 7 keV, and *LAXPC* spectra in 3 – 30 keV as significant data is unavailable for *LAXPC* beyond this range.

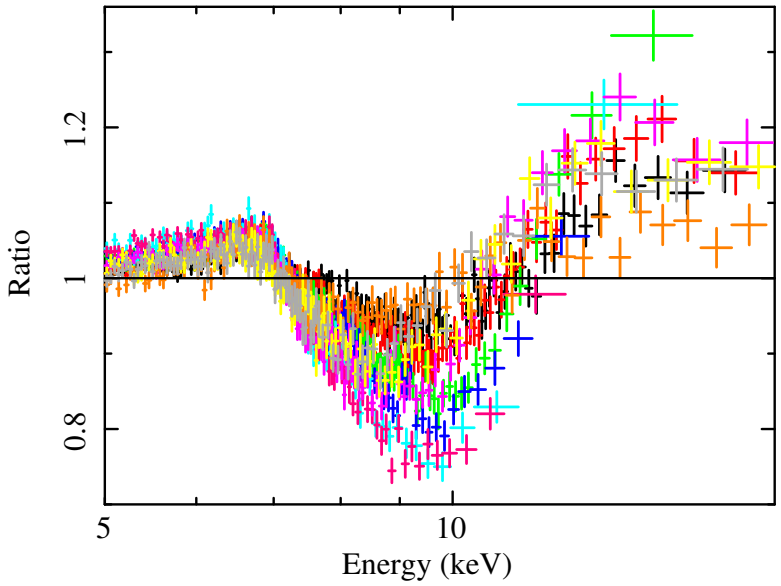

Figure 4.2: The ratios (model to data) of the spectral fitting of *NuSTAR* observations (Table 4.1) using `tbabs(diskbb+powerlaw)` model. The colours black, red, green, blue, cyan, pink, magenta, orange, yellow and grey represent the *NuSTAR* epochs in ascending order (Table 4.1). For all the epochs, a strong absorption feature exists between ∼ 8 – 11 keV. The absorption depth increases till Epoch 9 (pink in colour) and then decreases as the outburst progresses. The figure is zoomed around the absorption feature for better clarity.

4.4.1 Phenomenological Modelling and Evolution of Parameters

We performed wideband spectral modelling using phenomenological models in *XSPEC*. A brief description of various models and their parameters is provided in §2.3.1. To

accommodate the interstellar absorption, we used the `tbabs` model where line of sight column density, n_H, is a free parameter. We initially modelled the *NuSTAR* observations with `tbabs(diskbb+powerlaw)` model. A broad absorption feature at $\sim 8 - 11$ keV is detected in all the epochs of *NuSTAR*. The ratio of data to the model of all *NuSTAR* observations are shown in Fig. 4.2. The different *NuSTAR* epochs are shown in black, red, green, blue, cyan, pink, magenta, orange, yellow and grey colours in ascending order. It shows that the depth of absorption feature starts with a low value (black) and then keeps on increasing as the outburst progress, reaching the maximum on Epoch 9 (pink in colour). Finally, the absorption depth decreases towards the end (grey) of our study. We also found a similar absorption feature in the *AstroSat/LAXPC* data.

We tried several other models, for example, the thermal Comptonization model `nthcomp` (Zdziarski et al., 1996) or `thcomp` (Zdziarski et al., 2020) in place of `powerlaw`, and the `diskbb` was replaced by `kerrbb` (Li et al., 2005). The model combination with `kerrbb` as the seed photon source did not provide a good fit; moreover, it failed to constrain the BH mass and spin. So, we prefer to use the `diskbb` model in combination with `thcomp`, which is an improved version of `nthcomp`. Fitting using various combinations of these models also retains the absorption feature at $\sim 8 - 11$ keV.

Since the observed absorption feature has a symmetrical profile, the inclusion of a Gaussian absorption model, `gabs`, fits the absorption feature well. The parameters of `gabs` component are line energy (*line E*, E_0), line width (σ) and line depth (*strength*). We have attempted to apply a smeared absorption edge model, *smedge* (Ebisawa et al., 1994), in order to account for the absorption feature. However, this resulted in an unusually high value of absorption width due to the asymmetric nature of the model. Consequently, we chose to exclude this approach. In addition to the strong absorption feature, the *NuSTAR* data show a weak presence of a Fe K_α absorption edge at ~ 7.1 keV. Therefore, we also used an `edge` component to improve the fit residual for *NuSTAR*. The model parameters for the `edge` component are the threshold energy of the absorption edge (*line E*, E_g) and the corresponding absorption depth (D). Therefore, the final model combination for the phenomenological modelling is `tbabs(thcomp×diskbb)edge×gabs` (model M1, hereafter). The parameters of `diskbb` models are T_{in} and *diskbb norm*. Similarly, parameters of `thcomp` are Γ, electron temperature (k_BT_e), seed photon temperature (k_BT_{bb}) and the covering fraction (*cov_frac*). We tie the parameter k_BT_{bb} with T_{in} in the spectral fitting. In contrast, the neutral absorption feature ~ 7.1 keV was not visible in the *AstroSat/LAXPC* data, possibly due to the low spectral resolution of *LAXPC*. Therefore, the model M1 for *AstroSat* data becomes `tbabs(thcomp×diskbb)gabs`. However, the *AstroSat* data of Epoch 3 & 6 show

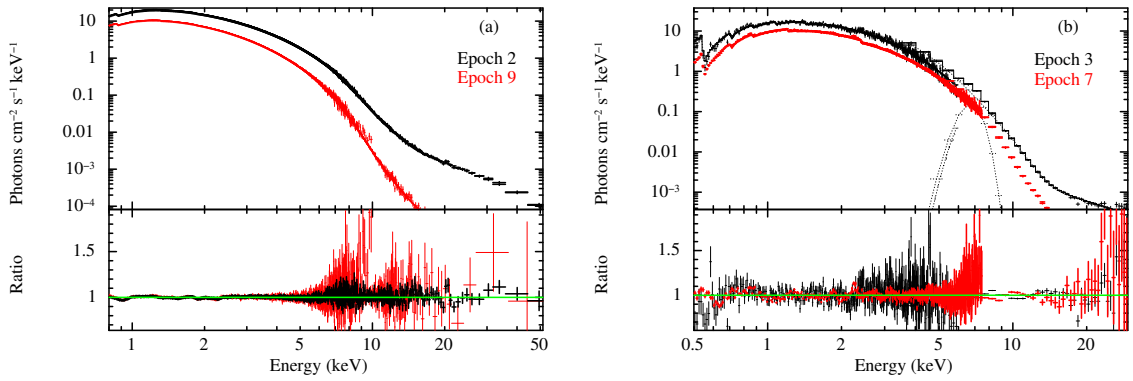

Figure 4.3: **(a)** Simultaneous *NICER-NuSTAR* pair on Epoch 2 (black) and Epoch 9 (red) fitted with the model `tbabs(thcomp×diskbb)edge×gabs`. Epoch 2 spectrum is harder compared to that of Epoch 9. **(b)** The *AstroSat* spectra on Epoch 3 (black) and 7 (red) respectively modelled using `tbabs(thcomp×diskbb)gabs`. We include an additional `gauss` component for *AstroSat* (Epoch 3) data. Both instruments show spectral changes during the outburst.

the presence of a weak Fe K_α emission line feature in the residual, and we include a `gauss` component for these two epochs of *AstroSat* data. The parameters of `gauss` model are *line E*, width (σ) and normalization (*norm*). All the seven *NICER-NuSTAR* simultaneous pairs and six *AstroSat* observations are fitted with the model M1. Fig. 4.3a and Fig. 4.3b show the wideband spectra of *NICER-NuSTAR* (Epoch 2 & 9) and *AstroSat* (Epoch 3 & 7) respectively modelled using M1. In each case, the spectrum in the red colour is relatively softer than that in the black colour; therefore, both figures illustrate moderate spectral changes during the outburst decay.

The goodness of the fit is determined using χ^2 statistics. The value of reduced χ^2 (χ^2_{red}) varies between 0.9−1.3. All the parameters estimated from the wideband phenomenological modelling are presented in Table 4.2. The parameter uncertainties are calculated within the 90% confidence range. Note that the *NuSTAR* observations on Epoch 8, 11 & 12 (Table 4.1) are omitted here as no simultaneous *NICER* observations are available. The n_H is left free and it varies between $(0.45 - 0.54) \times 10^{22}$ cm^{-2}. We aim to find out the evolution of various parameters with the progress of the outburst. Fig. 4.4 gives the variation of the inner disc temperature T_{in}, photon index Γ and `gabs` optical depth (τ) with time. Here, points in green and red colour represent the parameter values estimated from the modelling of *NICER-NuSTAR* and *AstroSat*, respectively.

Table 4.2: Wideband *NICER-NuSTAR* simultaneous pairs and *AstroSat* observations (highlighted in grey colour) using the model M1: `tbabs(thcomp×diskbb)edge×gabs` and `tbabs(thcomp×diskbb)gabs` respectively. The error values represent 90% confidence interval. The *NuSTAR* data on Epoch 8, 11 & 12 are not included here as no simultaneous *NICER* observations are available. The bolometric (0.5 − 100 keV) observed flux and estimated luminosity for each epoch is also shown.

Epoch	n_H	diskbb		thcomp			edge or gauss*		gabs			χ^2_{red}	F_{bol}	L_{bol}
	($\times10^{22}$ cm^{-2})	T_{in} (keV)	$norm$ ($\times10^3$)	Γ	k_BT_e (keV)	cov_frac ($\times10^{-2}$)	$line\ E$ (keV)	D or σ (keV)	$line\ E$ (keV)	σ (keV)	$strength$ (keV)		($\times10^{-8}$ erg cm^{-2} s^{-1})	(L_{Edd})
1	$0.470^{+0.002}_{-0.002}$	$1.272^{+0.002}_{-0.002}$	$7.96^{+0.05}_{-0.05}$	$2.44^{+0.06}_{-0.05}$	20^f	$2.3^{+0.2}_{-0.2}$	$7.16^{+0.05}_{-0.05}$	$0.04^{+0.01}_{-0.01}$	$10.0^{+0.1}_{-0.1}$	$1.60^{+0.09}_{-0.09}$	$0.84^{+0.08}_{-0.08}$	0.90	$27.64^{+0.04}_{-0.04}$	$1.52^{+0.14}_{-0.14}$
2	$0.458^{+0.002}_{-0.002}$	$1.159^{+0.002}_{-0.002}$	$6.07^{+0.04}_{-0.04}$	$2.0^{+0.1}_{-0.1}$	$11.6^{+3.9}_{-1.9}$	$0.9^{+0.2}_{-0.1}$	$7.19^{+0.07}_{-0.07}$	$0.03^{+0.01}_{-0.01}$	$9.9^{+0.1}_{-0.1}$	$1.65^{+0.07}_{-0.08}$	$1.2^{+0.1}_{-0.1}$	1.00	$17.22^{+0.02}_{-0.03}$	$0.95^{+0.09}_{-0.09}$
3	$0.52^{+0.02}_{-0.02}$	$0.99^{+0.01}_{-0.01}$	$15.4^{+1.5}_{-1.4}$	$1.84^{+0.14}_{-0.12}$	20^f	$0.39^{+0.07}_{-0.06}$	$6.77^{+0.15}_{-0.15}$	0.6^f	$7.35^{+0.34}_{-0.39}$	2^f	$1.73^{+0.47}_{-0.47}$	1.17	$19.5^{+0.1}_{-0.1}$	$1.07^{+0.001}_{-0.001}$
4	$0.461^{+0.002}_{-0.002}$	$1.094^{+0.002}_{-0.002}$	$5.82^{+0.05}_{-0.05}$	$2.2^{+0.1}_{-0.1}$	20^f	$0.3^{+0.1}_{-0.1}$	$7.27^{+0.07}_{-0.07}$	$0.05^{+0.01}_{-0.01}$	$10.4^{+0.1}_{-0.1}$	$1.94^{+0.08}_{-0.07}$	$2.2^{+0.2}_{-0.1}$	0.95	$12.38^{+0.02}_{-0.03}$	$0.68^{+0.06}_{-0.06}$
5	$0.458^{+0.002}_{-0.002}$	$1.050^{+0.002}_{-0.002}$	$5.77^{+0.04}_{-0.04}$	$2.3^{+0.2}_{-0.2}$	20^f	$0.2^{+0.1}_{-0.1}$	$7.28^{+0.05}_{-0.05}$	$0.06^{+0.01}_{-0.01}$	$10.7^{+0.1}_{-0.1}$	$1.97^{+0.08}_{-0.07}$	$2.7^{+0.2}_{-0.2}$	1.02	$10.10^{+0.01}_{-0.02}$	$0.56^{+0.05}_{-0.05}$
6	$0.50^{+0.02}_{-0.02}$	$0.97^{+0.02}_{-0.02}$	$12.1^{+1.5}_{-1.4}$	2.3^f	20^f	$0.3^{+0.02}_{-0.02}$	$6.77^{+0.18}_{-0.18}$	0.6^f	$9.05^{+0.51}_{-0.55}$	2.5^f	$2.27^{+0.66}_{-0.68}$	1.27	$13.9^{+0.06}_{-0.05}$	$0.76^{+0.001}_{-0.001}$
7	$0.54^{+0.01}_{-0.01}$	$0.98^{+0.01}_{-0.01}$	$7.64^{+0.33}_{-0.33}$	$2.26^{+0.06}_{-0.05}$	20^f	0.2^f	-	-	$10.7^{+0.2}_{-0.2}$	$1.46^{+0.24}_{-0.18}$	$1.56^{+0.25}_{-0.33}$	1.29	$9.36^{+0.21}_{-0.20}$	$0.51^{+0.004}_{-0.004}$
9	$0.451^{+0.003}_{-0.003}$	$0.966^{+0.002}_{-0.002}$	$5.60^{+0.05}_{-0.05}$	$2.6^{+0.5}_{-0.4}$	20^f	$0.1^{+0.2}_{-0.1}$	$7.44^{+0.08}_{-0.08}$	$0.08^{+0.02}_{-0.02}$	$10.5^{+0.2}_{-0.1}$	$2.02^{+0.09}_{-0.09}$	$3.3^{+0.3}_{-0.2}$	1.05	$6.88^{+0.02}_{-0.02}$	$0.38^{+0.04}_{-0.04}$
10	$0.53^{+0.01}_{-0.01}$	$0.96^{+0.01}_{-0.01}$	$5.63^{+0.35}_{-0.31}$	$1.92^{+0.30}_{-0.25}$	20^f	$0.11^{+0.05}_{-0.03}$	-	-	$10.1^{+0.2}_{-0.2}$	$1.56^{+0.20}_{-0.18}$	$2.13^{+0.39}_{-0.32}$	1.28	$7.59^{+0.04}_{-0.03}$	$0.40^{+0.001}_{-0.001}$
13	$0.52^{+0.01}_{-0.01}$	$0.91^{+0.01}_{-0.01}$	$7.48^{+0.24}_{-0.23}$	$1.77^{+0.03}_{-0.03}$	20^f	$0.12^{+0.05}_{-0.05}$	-	-	$9.42^{+0.27}_{-0.27}$	$0.75^{+0.30}_{-0.28}$	$0.47^{+0.13}_{-0.11}$	1.10	$6.59^{+0.06}_{-0.07}$	$0.36^{+0.002}_{-0.003}$
14	$0.48^{+0.01}_{-0.01}$	$0.91^{+0.01}_{-0.01}$	$7.92^{+0.58}_{-0.53}$	$1.94^{+0.02}_{-0.02}$	20^f	0.4^f	-	-	$10.7^{+0.24}_{-0.21}$	$1.34^{+0.18}_{-0.17}$	$1.47^{+0.18}_{-0.18}$	1.31	$6.22^{+1.89}_{-6.56}$	$0.34^{+0.08}_{-0.29}$
15	$0.465^{+0.004}_{-0.010}$	$0.904^{+0.030}_{-0.004}$	$6.10^{+0.09}_{-0.69}$	$2.09^{+0.04}_{-0.04}$	20^f	$1.6^{+0.1}_{-0.1}$	$7.31^{+0.08}_{-0.14}$	$0.10^{+0.05}_{-0.03}$	$9.6^{+0.3}_{-0.3}$	$2.1^{+1.2}_{-0.4}$	$1.1^{+1.1}_{-0.3}$	1.27	$5.66^{+0.02}_{-0.02}$	$0.31^{+0.03}_{-0.03}$
16	$0.471^{+0.002}_{-0.002}$	$0.897^{+0.002}_{-0.001}$	$6.22^{+0.05}_{-0.05}$	$2.04^{+0.04}_{-0.06}$	20^f	$1.6^{+0.1}_{-0.1}$	$7.35^{+0.06}_{-0.03}$	$0.12^{+0.02}_{-0.03}$	$9.4^{+0.4}_{-0.3}$	$1.5^{+0.4}_{-0.3}$	$0.5^{+0.1}_{-0.1}$	1.00	$5.39^{+0.01}_{-0.01}$	$0.30^{+0.03}_{-0.03}$

* `edge` is used for *NICER-NuSTAR* pairs whereas `gauss` component is used only for Epoch 3 & 6 of *AstroSat* data.
^{f} Frozen parameters

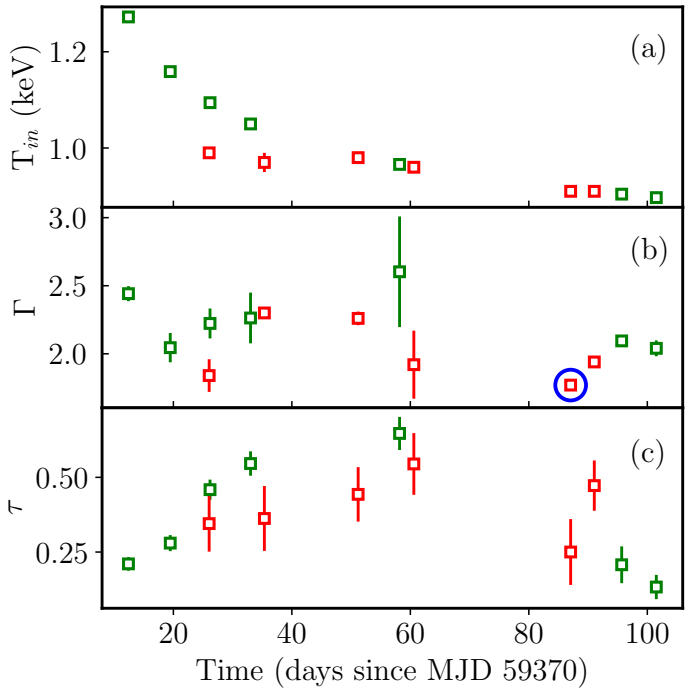

Figure 4.4: Evolution of **(a)** T_{in} and **(b)** Γ from simultaneous *NICER-NuSTAR* pairs (green) and *AstroSat* observations (red) fitted using the model M1. We calculate the (**c**) optical depth (τ) of the absorber from `gabs` components for each epoch. The Γ of Epoch 13 marked with a blue circle carries a special signature, discussed in §5.4.

We find that T_{in} (Fig. 4.4a and Table 4.2) monotonically decreases throughout the outburst decay. The evolution of the *diskbb norm* (Table 4.2) estimated using *NICER-NuSTAR* observations decreases till Epoch 9 and a reverse trend is observed for later epochs. The *diskbb norm* from the *AstroSat* data also shows a similar pattern though the values are higher than that of *NICER-NuSTAR*. The photon index Γ variation is presented in Fig. 4.4b. The value of Γ estimated from *AstroSat* data (red square) differs from that of *NICER-NuSTAR* pairs (green square). This can be due to the non-availability of the high-energy contribution (beyond 30 keV) in the *LAXPC* data. From *NICER-NuSTAR* fitting, Γ varies between 2 – 2.6, showing spectral softening until Epoch 9. We endeavoured to estimate the electron temperature (k_BT_e) of the corona using the `thcomp` model. But the broadband spectral fitting could not constrain the value of k_BT_e, except for Epoch 2, for which we obtained $k_BT_e = 11.6^{+3.9}_{-1.9}$ keV (Table 4.2). For all the remaining epochs, we freeze k_BT_e at 20 keV. Only a tiny fraction, *cov_frac* < 3 % (Table 4.2), of the soft photons undergo Comptonization in the corona. It gradually decreases till Epoch 10 and increases afterwards. This behaviour is consistent with the spectral softening trend shown in Fig. 4.4b.

The broad absorption feature at ∼ 8−11 keV in the spectrum is well represented by the

gabs model. The *strength* shows an increasing trend, reaching the maximum in Epoch 9 and declining beyond that. We calculate the optical depth, $\tau = strength/\sigma\sqrt{2\pi}$, associated with the gabs component. The evolution of τ is shown in Fig. 4.4c, which shows that the absorption optical depth increases and reaches a maximum on Epoch 9 and then decreases. The dynamic behaviour of the gabs absorption *strength* seems interesting. It deserves an in-depth examination, attempted in Chapter 5, to identify the real cause. The evolution of the edge component is listed in Table 4.2. We discuss a possible connection between edge and gabs components in Chapter 5.

We estimate the observed bolometric flux (F_{bol}) in 0.5 − 100 keV from the wideband simultaneous spectral data, which is also shown in Table 4.2. The error values indicate uncertainty in the 90% confidence interval. Corresponding bolometric luminosity (L_{bol}) of the source is also calculated by assuming the distance to the source as 7.5 ± 0.5 kpc (Jonker & Nelemans, 2004). The Eddington luminosity of the source is $L_{Edd} = 1.22 \pm 1 \times 10^{39}$ ergs s^{-1} with an assumed BH mass of 9.4 ± 1 $M_\odot$ (Russell et al., 2006). It can be seen from Table 4.2 that the luminosity of the source exceeds the L_{Edd} at the peak (Epoch 1 is close to the peak) of the outburst, and the luminosity decreases gradually with the outburst decay.

4.4.2 Spectral Modelling for Reflection Studies

To understand the reflection features in the spectra of 4U 1543 − 47, we use the relativistic reflection model RELXILL v1.4.3. Different flavours of the RELXILL model (see §2.3.2) are tried. The unfolded *NICER-NuSTAR* spectra and data-to-model ratios using various reflection models are shown in Fig. 4.5 for Epoch 2. We started with the model tbabs(diskbb+relxill) which gives a χ^2_{red} of 2.46. The data-to-model ratio (Fig. 4.5a) shows that the reflection model cannot fit the absorption feature existed in the spectrum at $\sim 8 - 11$ keV. We added the absorption model gabs with this, and the resulting model tbabs(diskbb+relxill)gabs (Fig. 4.5b) improved the residual but still the χ^2_{red} for this combination is 1.6. Then, we replaced the model relxill with relxillCp (Fig. 4.5c), where a thermal Comptonizing continuum is assumed for the illuminating flux. This combination has $\chi^2_{red} = 1.63$, which is also unacceptable. Then, we used relxilllpCp (Fig. 4.5d) as the reflection model, which also resulted in a large residual, with $\chi^2_{red} = 1.79$. We replaced relxilllpCp with relxilllp (Fig. 4.5e) where the illuminating flux is modelled as a powerlaw with a high-energy cut-off just like the relxill. For this trial, we got a reasonable fit with $\chi^2_{red} = 0.91$, and we decided to proceed with the model combination, tbabs(diskbb+relxilllp)gabs (model M2, hereafter) as the final model to study the

reflection features in the spectra. Note that no additional `edge` or `gauss` component is required in the reflection modelling.

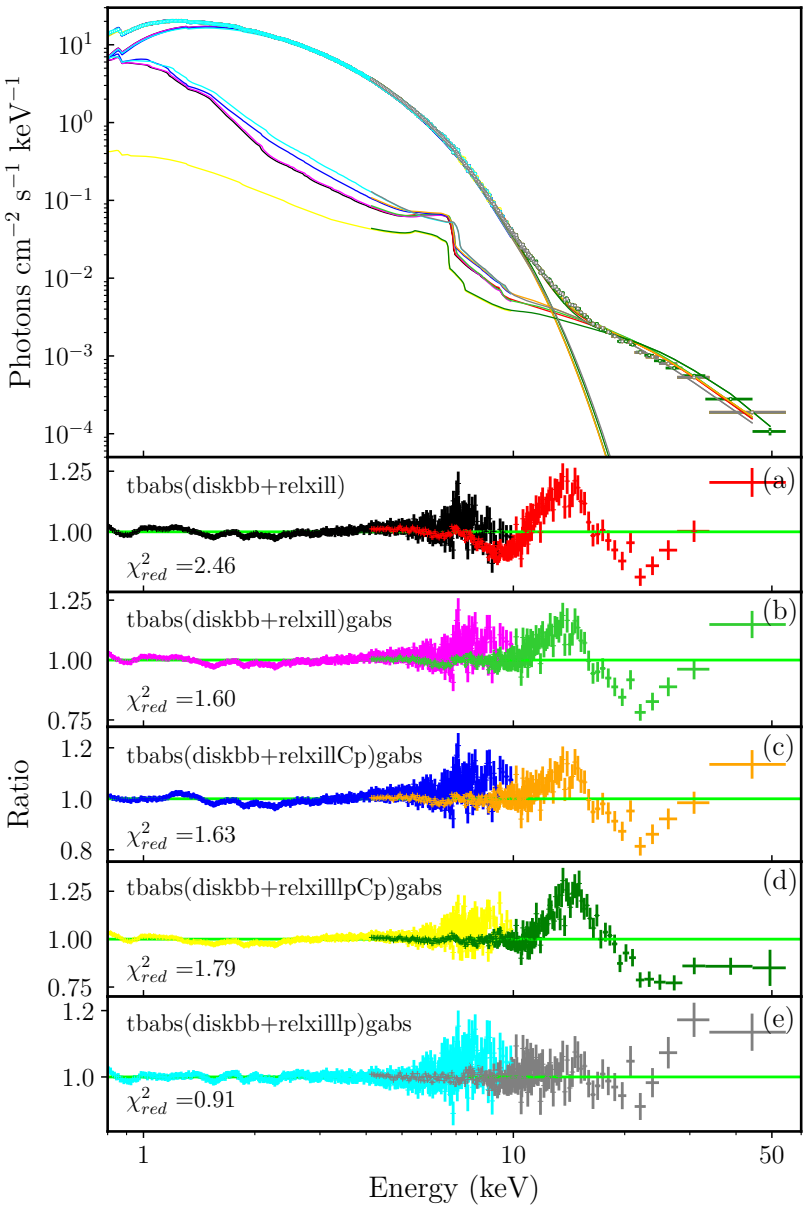

Figure 4.5: Unfolded spectrum (top panel) of simultaneous *NICER-NuSTAR* pair on Epoch 2 and ratio of the model to the data using various reflection models **(a)** `tbabs(diskbb+relxill)`, **(b)** `tbabs(diskbb+relxill)gabs`, **(c)** `tbabs(diskbb+relxillCp)gabs`, **(d)** `tbabs(diskbb+relxilllpCp)gabs` and **(e)** `tbabs(diskbb+relxilllp)gabs`. The model and the value of χ^2_{red} are mentioned at the top left and bottom left corners, respectively, in each case.

Using the model M2, we did the spectral fitting of the simultaneous *NICER-NuSTAR*

pairs and *AstroSat* observations. Here, n_H is a free parameter. Inner and outer disc radii are frozen at the innermost stable circular orbit R_{ISCO} and 400 r_g, respectively. The `powerlaw` cut-off energy, E_{cut}, is fixed at 60 keV since it is hitting the upper limit. All other parameters of `relxilllp` are kept free; the lamp-post height h (in units of r_g), the inclination angle of the system θ (in degree), Γ of the incident radiation, ionization parameter $log\ \xi$ (erg cm s^{-1}), iron abundance (A_{Fe}) of the accretion disc in terms of the solar abundance $A_{Fe,\odot}$, and the reflection fraction R_f. We wish to estimate the spin parameter, a_* of the system, but it is found to hit the upper limit for almost all the epochs. Based on previous studies (Morningstar & Miller, 2014; Dong et al., 2020) we freeze $a_* = 0.4$ for this study.

The estimated reflection model (M2) parameters are listed in Table 4.3. The errors represent a 90% confidence interval. The evolution of T_{in} follows the same trend as that observed in the phenomenological spectral modelling (Table 4.2). The value of Γ varies between $2 - 3.3$ and appears slightly steeper than that of phenomenological modelling (Table 4.2). It may be due to the additional low-energy contribution from the reflection component over the `diskbb` component. However, reflection modelling also shows spectral softening till Epoch 9. The *NICER-NuSTAR* results suggest that 4U 1543 − 47 is a low-inclination system with θ varying between $\sim 32^\circ - 40^\circ$. We could not constrain the inclination angle from *AstroSat* data and we freeze it to 40°.

The evolution of a few important model parameters (h, $\log \xi$ and R_f) are shown in Fig. 4.6 for better presentation. Simultaneous *NICER-NuSTAR* pairs and *AstroSat* observations are marked in green and red squares, respectively. We could not estimate the uncertainty of h in most epochs. The evolution of h (Fig. 4.6a) indicates that the primary source is moving away from the BH till Epoch 6 and then gradually coming closer to the central object. The ionization structure of the disc is established through the parameter log ξ. Its value (Fig. 4.6b) gradually increases, reaches the maximum around Epoch 10, and gradually decreases further. The high value of log ξ (>3) suggests a highly ionized disc material throughout the outburst. We could estimate iron abundance A_{Fe} for Epoch 1, 2, 4 and 5, and it hits the upper limit during the rest of the epochs. Our study reveals an overabundance (3.6−10 $A_{Fe,\odot}$) of iron in the disc. The reflection fraction R_f is estimated well at only the first three and last two epochs. Fig. 4.6c suggests that the fraction of primary photons reaching the disc increases until Epoch 9 and decreases afterward. The *gabs strength* exhibits a similar behaviour as observed in the phenomenological modelling.

Table 4.3: Reflection modelling of *NICER-NuSTAR* simultaneous pairs and *AstroSat* observations (highlighted with grey colour) using the model `tbabs(diskbb+relxilllp)gabs`. The error values represent 90% confidence interval. The *NuSTAR* data on Epoch 8, 11 & 12 are not included here as no simultaneous *NICER* observations are available.

Epoch	n_H	`diskbb`		`relxilllp`							`gabs`			χ^2_{red}
	($\times 10^{22}$ cm^{-2})	T_{in} (keV)	$norm$ ($\times 10^3$)	h (GM/c^2)	θ (deg)	Γ	$log\ \xi$ ($erg\ cm\ s^{-1}$)	A_{Fe} ($A_{Fe,\odot}$)	R_f	$norm$ ($\times 10^{-3}$)	$line\ E$ (keV)	σ (keV)	$strength$ (keV)	
1	$0.49^{+0.01}_{-0.01}$	$1.276^{+0.001}_{-0.001}$	$6.31^{+0.03}_{-0.03}$	25.50^{a}	$32.7^{+3.4}_{-2.9}$	$2.81^{+0.03}_{-0.03}$	$3.58^{+0.09}_{-0.07}$	$8.5^{+1.2}_{-1.3}$	$1.4^{+0.1}_{-0.2}$	$282.7^{+84.3}_{-46.1}$	$9.9^{+0.1}_{-0.1}$	$2.05^{+0.1}_{-0.03}$	$1.1^{+0.1}_{-0.1}$	0.80
2	$0.70^{+0.04}_{-0.05}$	$1.151^{+0.006}_{-0.005}$	$6.3^{+0.2}_{-0.2}$	9.4^{a}	$36.3^{+1.6}_{-1.8}$	$2.94^{+0.04}_{-0.08}$	$3.65^{+0.05}_{-0.08}$	$7.7^{+1.2}_{-1.1}$	$3.5^{+0.9}_{-0.7}$	$200.4^{+47.8}_{-53.9}$	$9.8^{+0.1}_{-0.1}$	$1.94^{+0.09}_{-0.09}$	$1.3^{+0.2}_{-0.2}$	0.91
3	$0.46^{+0.02}_{-0.01}$	$1.01^{+0.006}_{-0.006}$	$11.7^{+0.76}_{-0.44}$	30^{f}	40^{f}	3.0^{f}	4.7^{b}	$9.37^{b}_{-0.40}$	$5.59^{+1.85}_{-3.48}$	$0.32^{+0.08}_{-0.08}$	$9.37^{+0.27}_{-0.13}$	$0.75^{+0.37}_{-0.64}$	$0.48^{+0.03}_{-0.19}$	1.37
4	$0.683^{+0.004}_{-0.03}$	$1.081^{+0.001}_{-0.001}$	$6.14^{+0.008}_{-0.04}$	$30.5^{+24.3}_{-2.0}$	$35.7^{+2.2}_{-2.7}$	$3.23^{+0.01}_{-0.06}$	$4.23^{+0.05}_{-0.04}$	$5.8^{+0.8}_{-0.7}$	10.0^{a}	$41.1^{+20.3}_{-2.0}$	$10.04^{+0.04}_{-0.07}$	$1.92^{+0.04}_{-0.06}$	$1.99^{+0.2}_{-0.08}$	0.83
5	$0.67^{+0.01}_{-0.03}$	$1.044^{+0.001}_{-0.001}$	$5.83^{+0.01}_{-0.04}$	$84.0^{+56.6}_{-18.3}$	$39.6^{+2.6}_{-3.1}$	$3.385^{+0.006}_{-0.05}$	4.7^{b}	$7.1^{+0.6}_{-0.7}$	10.0^{a}	$33.6^{+3.7}_{-2.5}$	$10.33^{+0.03}_{-0.03}$	$2.06^{+0.03}_{-0.05}$	$2.76^{+0.02}_{-0.06}$	0.83
6	$0.49^{+0.01}_{-0.02}$	$0.99^{+0.07}_{-0.01}$	$9.23^{+1.46}_{-0.19}$	100^{f}	40^{f}	3^{f}	$4.30^{+0.21}_{-0.21}$	10^{b}	7.18^{a}	$7.11^{+1.95}_{-4.1}$	$10.0^{+0.13}_{-0.14}$	$1.30^{+0.13}_{-0.13}$	$1.39^{+0.28}_{-0.11}$	1.30
7	$0.53^{+0.03}_{-0.01}$	$0.99^{+0.003}_{-0.003}$	$6.94^{+0.16}_{-0.27}$	8.26^{a}	40^{f}	$2.46^{+0.36}_{-0.25}$	$3.70^{+0.75}_{-0.68}$	10^{b}	9.99^{a}	$5.75^{+0.55}_{-0.69}$	$10.5^{+0.16}_{-0.14}$	$1.45^{+0.20}_{-0.17}$	$1.65^{+0.30}_{-0.25}$	1.44
9	$0.496^{+0.01}_{-0.007}$	$0.958^{+0.001}_{-0.001}$	$5.85^{+0.04}_{-0.04}$	40.29^{a}	40^{f}	$3.17^{+0.1}_{-0.06}$	4.7^{b}	10^{b}	10^{f}	$4.0^{+2.3}_{-1.0}$	$10.11^{+0.08}_{-0.08}$	$1.86^{+0.06}_{-0.06}$	$3.1^{+0.2}_{-0.2}$	1.10
10	$0.44^{+0.03}_{-0.01}$	$0.98^{+0.004}_{-0.004}$	$4.95^{+0.10}_{-0.90}$	70^{f}	40^{f}	$2.87^{+0.33}_{-0.24}$	4.7^{b}	10^{b}	8.10^{a}	$1.33^{+0.28}_{-0.12}$	$10.2^{+0.13}_{-0.12}$	$1.78^{+0.16}_{-0.19}$	$2.76^{+0.36}_{-0.38}$	1.19
13	$0.47^{+0.01}_{-0.01}$	$0.94^{+0.002}_{-0.003}$	$5.90^{+0.08}_{-0.09}$	44.3^{a}	40^{f}	2.25^{f}	$3.64^{+0.09}_{-0.18}$	$3.56^{+0.56}_{-0.46}$	8.10^{a}	$1.11^{+0.07}_{-0.16}$	$9.22^{+0.21}_{-0.18}$	$0.84^{+0.20}_{-0.21}$	$0.74^{+0.10}_{-0.13}$	1.11
14	$0.48^{+0.01}_{-0.01}$	$0.91^{+0.002}_{-0.002}$	$7.95^{+0.21}_{-0.12}$	6.69^{a}	40^{f}	$2.61^{+0.08}_{-0.19}$	$3.96^{+0.07}_{-0.26}$	10^{b}	10.6^{a}	$0.14^{+0.01}_{-0.01}$	$10.1^{+0.13}_{-0.13}$	$1.03^{+0.12}_{-0.13}$	$1.25^{+0.14}_{-0.14}$	1.24
15	$0.475^{+0.004}_{-0.003}$	$0.906^{+0.001}_{-0.001}$	$5.91^{+0.04}_{-0.04}$	33.74^{a}	$38.0^{+8.5}_{-4.4}$	$2.07^{+0.06}_{-0.06}$	$2.7^{+0.1}_{-0.3}$	10.0^{b}	$0.9^{+0.2}_{-0.2}$	$4.9^{+1.5}_{-0.7}$	$9.1^{+0.1}_{-0.1}$	$1.5^{+0.1}_{-0.2}$	$1.0^{+0.1}_{-0.1}$	1.12
16	$0.482^{+0.004}_{-0.004}$	$0.904^{+0.001}_{-0.001}$	$5.63^{+0.05}_{-0.05}$	50.01^{a}	$36.7^{+9.4}_{-5.5}$	$2.05^{+0.05}_{-0.05}$	$3.7^{+0.1}_{-0.2}$	10.0^{b}	$0.9^{+0.2}_{-0.1}$	$4.2^{+0.8}_{-0.6}$	$8.7^{+0.1}_{-0.1}$	$1.49^{+0.08}_{-0.08}$	$1.2^{+0.2}_{-0.2}$	0.87

[a] Parameter uncertainty can't be estimated.
[b] Parameter hits the boundary.
[f] Frozen parameters.

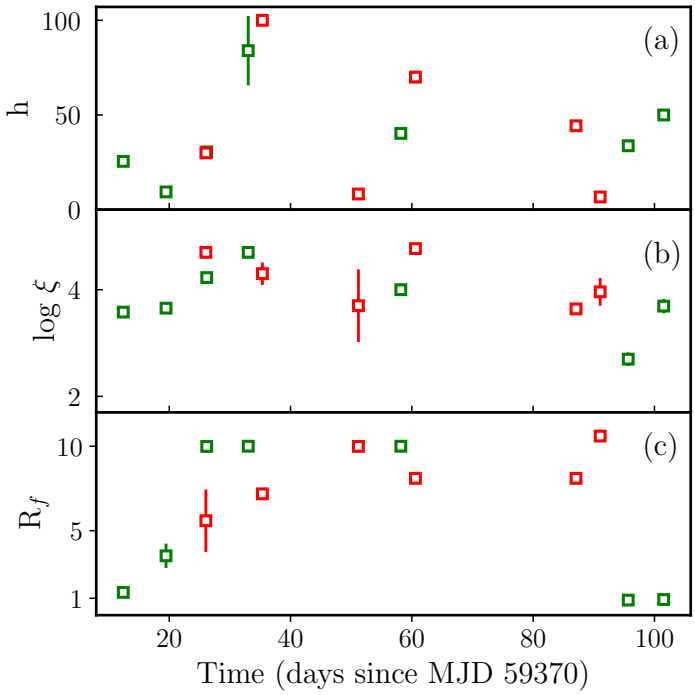

Figure 4.6: Evolution of **(a)** h, **(b)** log ξ and **(c)** R_f from reflection modelling of simultaneous *NICER-NuSTAR* pairs (green) and *AstroSat* observations (red) using the model `tbabs(diskbb+relxilllp)gabs`. See text for details.

The RELXILL model (version v2.2) has recently undergone some modifications by considering the effect of returning radiation in calculating reflected flux. Particularly in `relxilllpCp`, where the effects of returning radiation, the density profile and ionization gradient of the disc and the velocity of the primary source are also included. However, the velocity of the primary source and the effects of returning radiation are the new parameters added to the `relxilllp` model. We have applied this modified `relxilllp` model to the broadband *NICER-NuSTAR* data but could not constrain the source velocity. Also, we have tried to estimate the parameters using the v2.2 flavour of `relxilllpCp`. We have fitted all the wideband *NICER-NuSTAR* observations using the model `tbabs(diskbb+relxilllpCp)gabs`. But, we could not constrain most of the parameters since the number of free parameters is very large. Therefore, we need to essentially freeze all the new parameters introduced in the updated version, and RELXILL v2.2 does not improve the result.

4.5 Comprehensive Study of the Outburst: The HID

We want to understand the evolution of the source during the 2021 outburst in the Hardness-Intensity diagram (HID). *NICER* has a full coverage of the source 4U 1543-47 during its 2021 outburst. This analysis considers all the available *NICER* observations with exposure time greater than 500 sec. The spectral modelling of *NICER* observations in 0.8−10 keV energy band has been performed using model M1.

We estimated the flux in 0.8−2 keV, 2−10 keV and 0.8−10 keV bands separately for each observation. Hardness is defined as the flux ratio in 2−10 keV to that in 0.8−2 keV. The hardness-intensity diagram of the source is shown in Fig. 4.7a. The arrows track the evolution of the outburst. The HID shows correlated behaviours of flux and HR in both

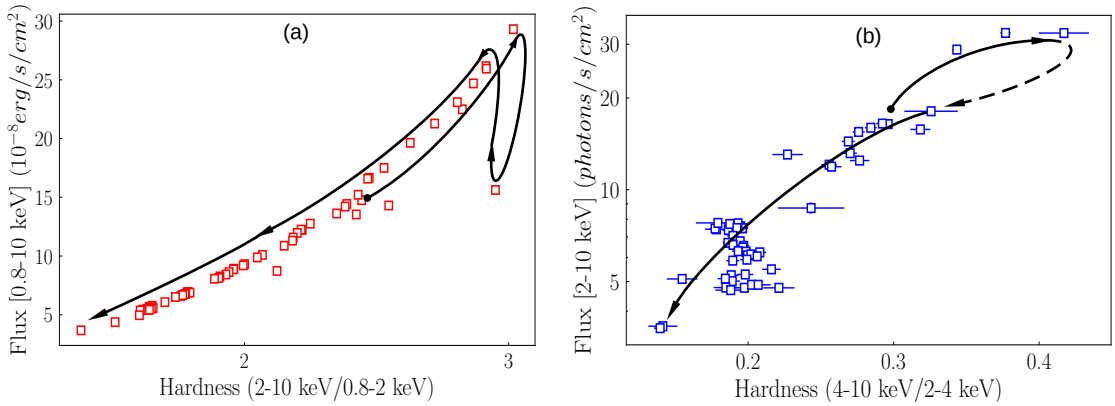

Figure 4.7: **(a)** HID of 4U 1543-47 in 2021 outburst generated using *NICER* observations. Hardness is the ratio of fluxes in 2−10 keV and 0.8−2 keV. **(b)** HID generated from *MAXI/GSC* daily lightcurve information for a similar period of time. Here, hardness is defined as the ratio of fluxes in 4−10 keV and 2−4 keV. The time evolution of the outburst is shown in arrows.

the rising and declining phase of the outburst with a 'loop' structure due to a momentary reduction of flux just after the peak. This shape of the HID departs from its standard q-shape, and instead, it displays a linear connection during the outburst. This shape of the HID is generic even if we change the definition of HR.

For comparison, the HID generated using the daily lightcurve of *MAXI/GSC* is shown in Fig. 4.7b. Here, we use the same definition of HR as in Fig. 4.1c. The *MAXI/GSC* lightcurve has a data gap of 9 days just after the peak of the outburst, which is shown in the dashed line in Fig. 4.7b. Therefore, *MAXI/GSC* did not capture the sudden drop in the flux after the peak observed in the HID of *NICER*.

4.6 Timing Analysis of 4U 1543-47

The timing analysis of 4U 1543-47 is carried out using the *NICER, NuSTAR* and *AstroSat/LAXPC* observations for around the first 100 days of the outburst, from MJD 59377 to 59471. We consider all 10 *NuSTAR* observations and 6 *AstroSat/LAXPC* observations. *NICER* has good coverage during the outburst, and we consider observations with exposure time greater than 500 sec for this study. Lightcurves are generated with a bin size of 0.003 sec for *NICER*, 0.01 sec for *NuSTAR* and *LAXPC* observations. To maintain a common energy range between instruments, we generate *NICER* lightcurves in three energy bands, 0.8−3 keV, 3−10 keV, and the total energy band from 0.8 to 10 keV. Similarly, we create lightcurves in the energy ranges 3−10 keV, 10−20 keV for *LAXPC*, and only 3−10 keV lightcurve for *NuSTAR*. Since the source is mostly in the HSS throughout the outburst and the hard flux contribution is much less, *NuSTAR* timing results beyond 10 keV are statistically insignificant.

We generated PDS in each energy band, and the Poison noise subtracted PDS are modelled in *XSPEC* (see §2.4.1). The PDS are almost flat and featureless throughout the outburst. A powerlaw, or combination of a powerlaw and broad `Lorentzians`, fits the PDS. The RMS (in percentage) is estimated between 0.001−1 Hz from individual PDS, and in most cases, the PDSs become noisy beyond this frequency range. The RMS evolution is plotted against time (Fig. 4.8) for the first 100 days of the outburst. The blue and red stars represent RMS in 0.8−3 keV and in 3−10 keV energy bands of *NICER*, respectively. The green circles and magenta squares represent RMS in 3−10 keV of *NuSTAR* and *LAXPC*, respectively. Orange squares represent RMS in 10−20 keV of *LAXPC*. The overall RMS is low as the source was in the HSS during the outburst. The RMS in 0.8−3 keV of *NICER* varies between 0.1−0.8%, and the RMS in 3−10 keV from *NICER, NuSTAR* and *LAXPC* varies between 0.4−2.2%. For *LAXPC*, the RMS in 10−20 keV varies between 5.3−6.7%, which is relatively higher than the RMS in the low-energy band. The PDS in 3−10 keV of *NICER* observations, particularly beyond day 40, are noisy. Hence we have omitted such observations from the study. The PDS from the higher energy bands has poor statistics, leading to high uncertainties in the estimated RMS.

We did not detect QPO in the *NICER* and *NuSTAR* observations. However, *LAXPC* observation on day 91 (Epoch 14) shows a QPO (Fig. 4.9) signature in the 3−10 keV energy band. The observed QPO feature has a characteristic frequency of 2.45±0.08 Hz, Q-factor of 7.42 and significance of 2.6.

Also, we checked if the data show any timing signature of the absorption features at

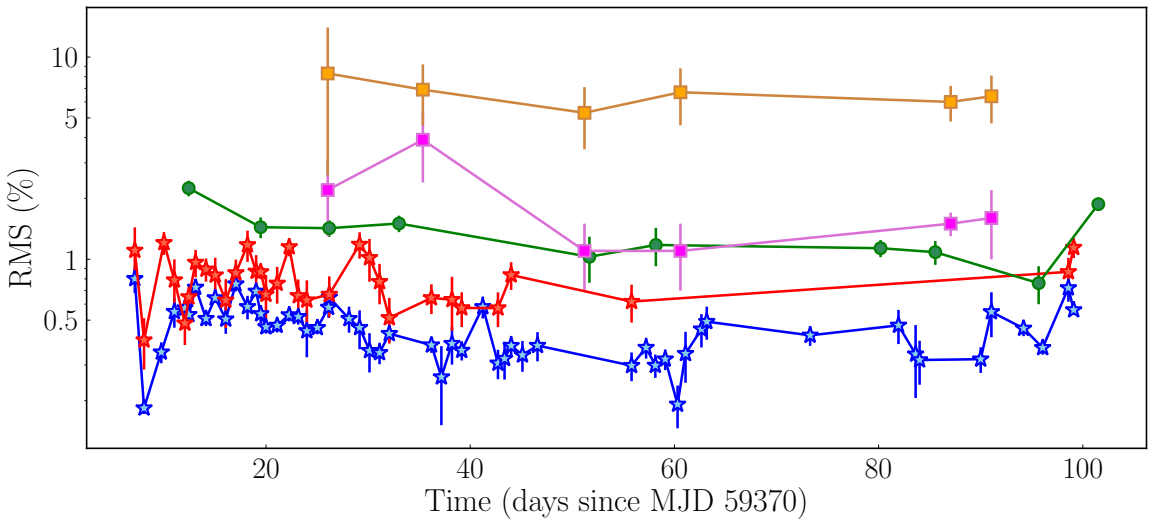

Figure 4.8: Evolution of the RMS (in percentage) estimated between 0.001−1 Hz from the three instruments. Blue and red stars indicate RMS in 0.8−3 keV and 3−10 keV respectively of *NICER*. Green circles indicate RMS in 3−10 keV of *NuSTAR*. Magenta and orange squares indicate RMS in 3−10 and 10−20 keV of *AstroSat/LAXPC* respectively.

$\sim 8-11$ keV in the spectra. To explore this, we generated *NuSTAR* and *AstroSat* lightcurves in 3−7 keV, 7−12 keV and 12−20 keV. But the nature of the PDS and RMS show similar behaviour as shown in Fig. 4.8. Also, the lightcurves in various energy bands showed no detectable time lag.

4.7 Discussion

The wideband spectral modelling of *NICER-NuSTAR* and *AstroSat* data have revealed that the accretion disc is extremely luminous with a super Eddington peak luminosity on Epoch 1 (last column of Table 4.2). The estimated column density along the line of sight is $(0.44-0.7)\times10^{22}\mathrm{cm}^{-2}$. The inner disc temperature T_{in} is highest (1.27 keV) on Epoch 1, and it keeps on decreasing during the decay of the outburst (Fig. 4.4a). The estimated *diskbb norm* (Table 4.2, Table 4.3) suggests a marginal inward movement of the inner disc radius r_{in} since *diskbb norm* $\propto r_{in}^2$ and r_{in} is possibly close to ISCO. However, the decrease in r_{in} could not prevent the drop in T_{in} due to the gradual decline in $\dot{M}$ as $T_{in} \propto \dot{M}^{1/4}\, r_{in}^{-3/4}$ (Equation 1.17). The extreme luminosity in the inner accretion disc may slow down the accretion of matter to the BH. The gradual decline of T_{in} can be due to the reduced infall of matter onto the BH through the inner disc. The source luminosity is completely soft-photon-dominated due to the very little fractional Comptonization (*cov_frac* in Table 4.2),

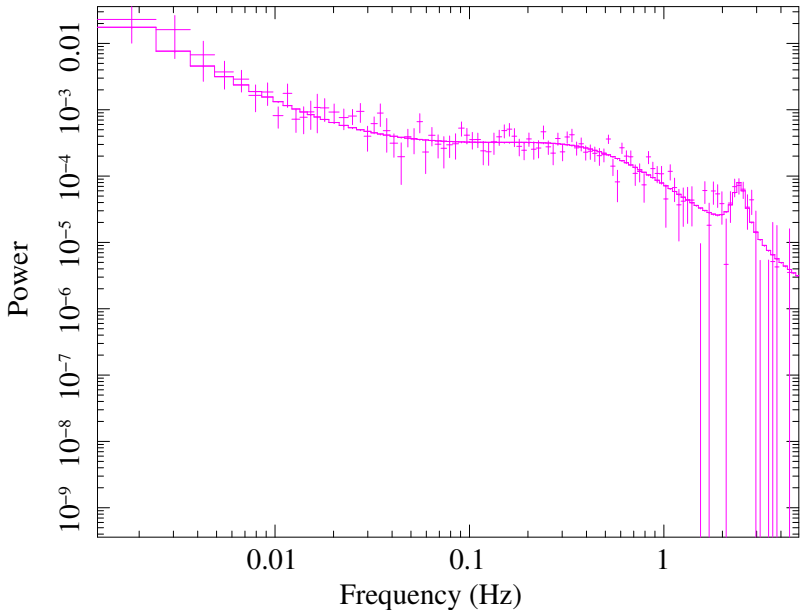

Figure 4.9: The power density spectrum of the Epoch 14 *Astrosat/LAXPC* observation in 3−10 keV band. A QPO feature is observed at 2.45±0.08 Hz with a Q-factor of 7.42 and a significance of 2.6.

the low corona temperature, and the steeper photon index Γ (Fig. 4.4b). Therefore, the source was in the high/soft spectral state during our study, and it was the softest on Epoch 9.

The important parameters for reflection modelling are shown in Table 4.3 and Fig. 4.6. The estimated inclination of the system is $\theta \sim 32^\circ - 40^\circ$ (Table 4.3). The lamp-post height comes closer to the central object as the source becomes softer. The reflection fraction (R_f) increases and hits the boundary when the source is the softest. If the value of the ionization parameter, $\log \xi \gtrsim 3$, the fluorescence yield of the highly ionized Fe line (more ionized than Fe XXIII) increases (Matt et al., 1993). The high value of $\log \xi$ (Table 4.3) obtained from reflection modelling suggests a highly ionized accretion disc throughout the outburst.

An important characteristic of this source is the presence of a broad, symmetric and dynamic absorption feature in the spectrum $\sim 8 - 11$ keV. Such a broad and wide feature has never been observed in XRB systems. Both phenomenological and reflection modelling show that the *gabs strength* shows an increasing trend, reaches the maximum in Epoch 9 and declines beyond that. We will examine the dynamic nature of this feature in detail in Chapter 5.

The *NICER* and *MAXI/GSC* HID (Fig. 4.7a,b) show a roughly linear correlation between flux and HR with a loop structure just after the peak flux. It differs from the standard q-

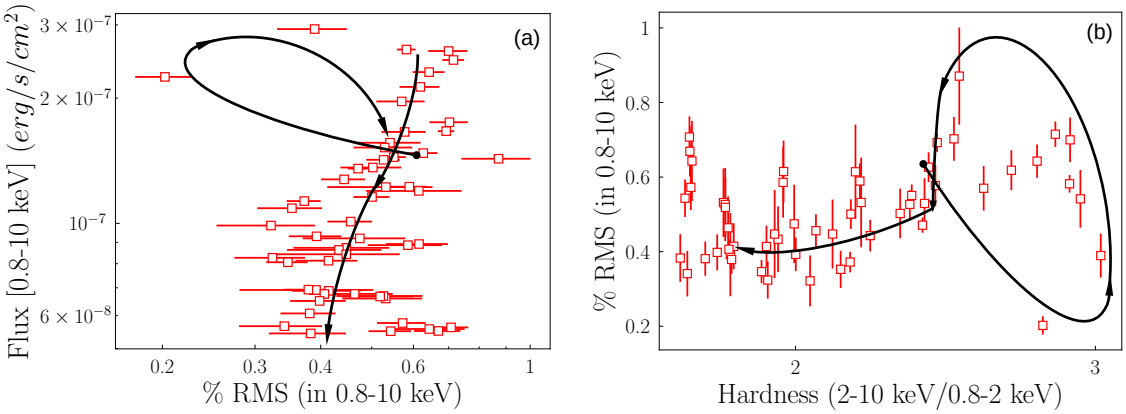

Figure 4.10: **(a)** The RMS-intensity diagram and **(b)** the hardness-RMS diagram of the source for the first 100 days of the outburst using *NICER* observations. The evolutionary track of the outburst is shown in arrows.

shape profile observed in most complete outbursts. Also, contrary to other outbursts, the source was in the HSS, even at quiescence. This is a sign that most of the observed flux is contributed by the accretion disc, and therefore as the flux decreases, HR also follows the same. A similar kind of loop behaviour followed by correlated decay in HID is observed in the 2019 outburst of MAXI J0637−430 (Baby et al., 2021; Jana et al., 2021) and 2016, 2018 outbursts of 4U 1630−472 Baby et al. (2020).

The timing analysis of *NICER, NuSTAR* and *AstroSat/LAXPC* show featureless PDS with very low RMS since the source was in HSS during the outburst. The estimated RMS in 0.8−3 keV is less than 1% while the same in 3−10 keV is 0.4−2.2%. The *LAXPC* observation on day 91 (Epoch 14) shows the occurrence of a QPO at 2.45±0.08 Hz in 3−10 keV. However, we detected no QPO in the *LAXPC* 10−20 keV band. The observed QPO feature may be associated with the transient activity at the inner accretion disc (see §5.4, Chapter 5). In contrast, the 2002 outburst of this source showed the presence of strong low-frequency QPO (7.3−8.1 Hz) for several days (Park et al., 2004), with a significantly higher RMS in the PDS.

The source's RMS–intensity diagram (RID) is created using the NICER observations in 0.8−10 keV. Fig. 4.10a shows a loop structure in RID at the beginning due to the momentary drop of the flux between rising and gradual decline. The flux declines weakly correlated with the RMS (within uncertainties). Therefore, the variability in the lightcurve has an accretion disc origin.

The spectro-temporal behaviour of the source is presented in the hardness-RMS diagram (HRD) in Fig. 4.10b using *NICER* observations. The HRD also shows a loop structure at

the beginning due to the momentary change in HR close to the peak of the outburst. The RMS and HR change in a correlated fashion, along with the declination of the outburst. Therefore, the source's spectro-temporal behaviour is consistent with the accretion disc-dominated nature of the outburst.

4.8 Summary and Conclusion

We studied the wideband spectral and timing properties of the 2021 outburst of 4U 1543−47. The *MAXI/GSC* lightcurve (Fig. 4.1) shows that the outburst rises over 9 days followed by a slow decay over $\sim$ 175 days. We used multi-instruments data (*NICER, NuSTAR and AstroSat*) for simultaneous broadband spectral study over 100 days from MJD 59370. We performed the spectral study using the phenomenological model M1 and reflection model M2. We also did timing studies using all three instruments. The major findings from our study are summarized below:

- The source generally remains very bright during this outburst with a super Eddington peak luminosity on Epoch 1 (Table 4.2).
- The source was in the HSS during our study, with a steep photon index (Fig. 4.4b) due to a very small fraction ($< 3\%$) of inverse-Comptonized photons and low corona temperature.
- The reflection modelling reveals that the system's inclination is between $32°-40°$.
- The extreme luminosity, high ionization ($\log \xi > 3$) and an overabundance of iron ($3.6 - 10\ A_{Fe,\odot}$) are observed.
- Presence of a broad, dynamic absorption feature at $\sim$ 8−11 keV is observed throughout our study. This detection is the first of its kind for X-ray binaries. The strength of the feature (Table 4.2 & Table 4.3) increases between Epoch 1 to Epoch 9.
- The HID (Fig. 4.7a,b) of the source shows a correlated evolution of flux and HR, consistent with the observed flux's thermal disc origin.
- The multi-instrument timing analysis in various energy bands reveals mostly featureless PDS with very low total RMS. Though *LAXPC* observation on Epoch 14 showed a strong QPO at 2.45±0.08 Hz in the 3−10 keV band.

- The RID (Fig. 4.10a) shows a loop pattern and then follows a gradual decline. As HR and RMS are correlated with flux, combining the two in an HRD (Fig. 4.10b) showed a gradual correlated decline. Therefore, the spectral and timing results reveal that the 2021 outburst of this source is thermal disc dominated.

Chapter 5

Absorption Features in the Spectra of 4U 1543−47: Detection of Relativistic Disc Wind

In Chapter 4, we have performed a broadband spectral study of 4U 1543 − 47 during the 2021 outburst. The spectra reveal a strong and broad absorption feature at $\sim 8-11$ keV. Such an absorption has never been observed in any X-ray binary system. Here, we present a detailed analysis of the absorption signature and discuss its possible origin. This work has been published in *MNRAS* Prabhakar et al. (2023).

5.1 Analysis of the Absorption Feature in the *NuSTAR* Data

We choose only *NuSTAR* observations to characterise the observed absorption signature since it has the best energy resolution. Also, multi-instrument spectral modelling may affect the parameter estimation of the absorption component. Additionally, we aim to study the variation of the absorption feature with the orbital phase of the system. Since 4U 1543 – 47 is a low-inclination system, $\theta \sim 32^{\circ} - 40^{\circ}$ (Table 4.3), the expected orbital variation of the absorption feature, if any, will be weak. Therefore, we avoid using multi-instrument data as the calibration discrepancies in the spectral response between instruments may screw up the variation.

We perform spectral modelling of 10 epochs (see Table 4.1) of *NuSTAR* data by the same combination of models `tbabs(thcomp` $\times$ `diskbb)edge` $\times$ `gabs` (model M1) and `tbabs(diskbb+relxilllp)gabs` (model M2) used in Chapter 4. Fig. 5.1 displays the

spectrum of Epoch 4 *NuSTAR* observation fitted using the model M1. Panel (a) shows the absorption feature existed between ∼ 8−11 keV, which is then fitted using gabs as shown in Panel (b).

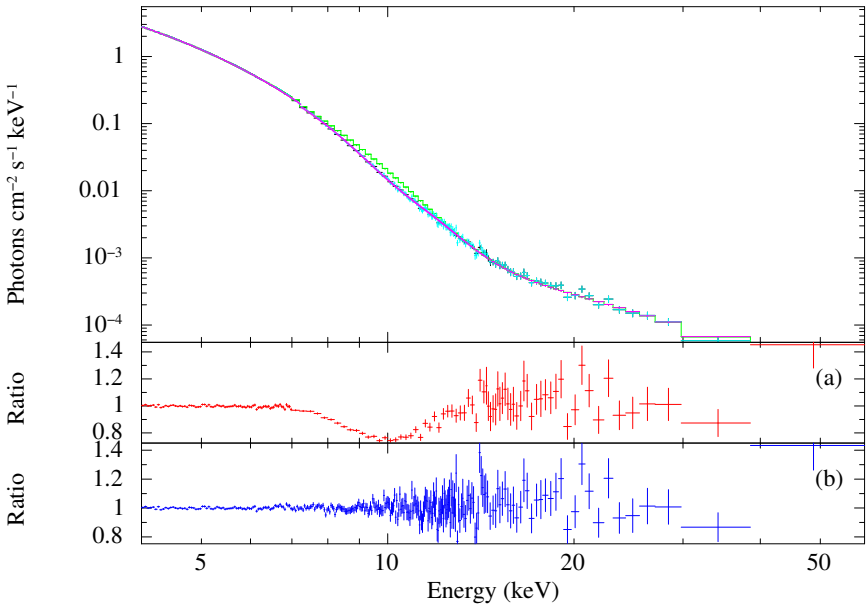

Figure 5.1: The spectra of Epoch 4 *NuSTAR* observation fitted using the model `tbabs(thcomp×diskbb)edge`. The ratio of the model to the data in panel (a) displays the absorption feature at ∼ 8−11 keV, which is being fitted using an additional the model *gabs* in panel (b).

The line-of-sight column density, n_H, is frozen at 0.45×10^{22} cm^{-2} which was determined from the broadband *NICER-NuSTAR* spectral modelling. Table 5.1 and Table 5.2 summarise the important model parameters obtained from the phenomenological and reflection modelling. The value of spectral parameters are consistent with that from the wideband spectral study (Table 4.2 and Table 4.3). Again, we use the `gabs` model to characterize the absorption feature. We calculated the `gabs strength` (say, S_i) for each *NuSTAR* epoch using both models. The evolution of S_i is shown in Fig. 5.2. The black, red, green, blue, cyan, pink, magenta, orange, yellow, and grey indicate the NuSTAR epochs chronologically (Table 4.1). The absorption `strength` represented by the square symbol is estimated using the model M1, whereas the same using M2 is denoted by the star symbol. We notice that the value estimated using M2 are marginally higher than the same from M1. This can be the effect of an additional `edge` component used in the M1 model. The `gabs strength` of *NuSTAR* data is showing the same trend of wideband spectral data, getting more stronger as the outburst progresses and reaches the maximum value on Epoch 9 (pink in colour), then declines gradually.

Table 5.1: Parameters of phenomenological spectral modelling of *NuSTAR* using the model `tbabs(thcomp×diskbb)edge×gabs` (M1). Errors are in 90% confidence intervals.

Epoch	`diskbb`		`thcomp`			`edge`		`gabs`			χ^2_{red}
	T_{in} (keV)	*norm* ($\times 10^3$)	Γ	k_BT_e (keV)	*cov_frac* ($\times 10^{-2}$)	*line E* (keV)	D (keV)	*line E* (keV)	σ (keV)	*strength* (keV)	
1	$1.238^{+0.005}_{-0.004}$	$3.81^{+0.06}_{-0.08}$	$2.73^{+0.06}_{-0.06}$	150.00^a	$0.088^{+0.007}_{-0.032}$	$7.2^{+0.1}_{-0.1}$	$0.04^{+0.01}_{-0.01}$	$10.0^{+0.2}_{-0.1}$	$1.3^{+0.2}_{-0.1}$	$0.48^{+0.10}_{-0.07}$	1.17
2	$1.129^{+0.003}_{-0.001}$	$3.58^{+0.05}_{-0.05}$	$2.3^{+0.1}_{-0.1}$	24.53^a	$0.026^{+0.017}_{-0.005}$	$7.20^{+0.07}_{-0.07}$	$0.05^{+0.01}_{-0.01}$	$9.82^{+0.07}_{-0.09}$	$1.27^{+0.09}_{-0.08}$	$0.68^{+0.08}_{-0.07}$	1.14
4	$1.055^{+0.003}_{-0.002}$	$3.58^{+0.05}_{-0.06}$	$2.4^{+0.2}_{-0.3}$	24.75^a	$0.008^{+0.007}_{-0.003}$	$7.23^{+0.05}_{-0.05}$	$0.08^{+0.01}_{-0.01}$	$10.06^{+0.09}_{-0.09}$	$1.32^{+0.09}_{-0.09}$	$1.0^{+0.1}_{-0.1}$	1.09
5	$1.024^{+0.004}_{-0.004}$	$3.27^{+0.07}_{-0.08}$	$2.0^{+0.6}_{-0.9}$	9.98^a	$0.002^{+0.005}_{-0.002}$	$7.28^{+0.06}_{-0.06}$	$0.09^{+0.02}_{-0.02}$	$10.3^{+0.2}_{-0.2}$	$1.5^{+0.1}_{-0.1}$	$1.5^{+0.2}_{-0.3}$	1.07
8	$0.952^{+0.005}_{-0.004}$	$3.31^{+0.09}_{-0.10}$	$2.1^{+0.3}_{-0.3}$	7.53^a	$0.002^{+0.001}_{-0.001}$	$7.27^{+0.06}_{-0.06}$	$0.10^{+0.02}_{-0.02}$	$10.1^{+0.2}_{-0.1}$	$1.5^{+0.1}_{-0.1}$	$1.8^{+0.3}_{-0.2}$	1.13
9	$0.940^{+0.004}_{-0.004}$	$3.29^{+0.08}_{-0.09}$	$2.7^{+0.4}_{-0.5}$	150.00^a	$0.004^{+0.003}_{-0.003}$	$7.36^{+0.07}_{-0.07}$	$0.10^{+0.02}_{-0.02}$	$10.2^{+0.1}_{-0.1}$	$1.6^{+0.1}_{-0.1}$	$2.0^{+0.3}_{-0.2}$	1.04
11	$0.921^{+0.002}_{-0.002}$	$3.27^{+0.05}_{-0.06}$	$2.00^{+0.10}_{-0.08}$	21.04^a	$0.016^{+0.009}_{-0.002}$	$7.20^{+0.04}_{-0.04}$	$0.11^{+0.02}_{-0.02}$	$9.4^{+0.1}_{-0.1}$	$1.1^{+0.1}_{-0.1}$	$0.7^{+0.1}_{-0.1}$	1.03
12	$0.920^{+0.004}_{-0.004}$	$2.94^{+0.08}_{-0.08}$	$2.20^{+0.09}_{-0.07}$	19.90^a	$0.087^{+0.020}_{-0.010}$	$7.27^{+0.09}_{-0.09}$	$0.10^{+0.02}_{-0.02}$	$9.5^{+0.4}_{-0.4}$	$1.0^{+0.3}_{-0.3}$	$0.17^{+0.06}_{-0.07}$	1.06
15	$0.901^{+0.002}_{-0.003}$	$3.11^{+0.06}_{-0.06}$	$1.98^{+0.08}_{-0.07}$	19.76^a	$0.026^{+0.007}_{-0.003}$	$7.07^{+0.09}_{-0.04}$	$0.07^{+0.02}_{-0.02}$	$9.2^{+0.1}_{-0.1}$	$1.1^{+0.1}_{-0.1}$	$0.54^{+0.11}_{-0.09}$	1.13
16	$0.897^{+0.002}_{-0.003}$	$3.05^{+0.06}_{-0.07}$	$1.92^{+0.08}_{-0.06}$	15.01^a	$0.026^{+0.004}_{-0.002}$	$7.3^{+0.1}_{-0.1}$	$0.09^{+0.03}_{-0.03}$	$9.0^{+0.3}_{-0.3}$	$1.0^{+0.2}_{-0.2}$	$0.33^{+0.11}_{-0.09}$	1.05

[a] Parameter uncertainty can't be estimated.

Table 5.2: Parameters of the reflection modelling of *NuSTAR* using the model `tbabs(diskbb+relxilllp)gabs` (M2). Errors are in 90% confidence intervals.

Epoch	`diskbb`		`relxilllp`							`gabs`			χ^2_{red}
	T_{in} (*keV*)	*norm* ($\times 10^3$)	h (GM/c^2)	θ (*deg*)	Γ	$log\ \xi$ (*erg cm/s*)	A_{Fe} ($A_{Fe,\odot}$)	R_f	*norm* ($\times 10^{-3}$)	*line E* (*keV*)	σ (*keV*)	*strength* (*keV*)	
1	$1.24^{+0.01}_{-0.01}$	$7.2^{+0.3}_{-0.3}$	$40.03^{+2.5}_{-2.3}$	$25.8^{+6.3}_{-8.4}$	$2.72^{+0.09}_{-0.09}$	$4.0^{+0.5}_{-0.5}$	10.0^{b}	$0.4^{+0.4}_{-0.1}$	$0.23^{+0.08}_{-0.07}$	$9.7^{+0.2}_{-0.2}$	$1.6^{+0.3}_{-0.2}$	$0.6^{+0.2}_{-0.1}$	1.16
2	$1.112^{+0.002}_{-0.002}$	$7.44^{+0.05}_{-0.05}$	$9.4^{+4.6}_{-3.7}$	$28.9^{+3.6}_{-3.7}$	$2.60^{+0.1}_{-0.05}$	$4.1^{+0.2}_{-0.2}$	10^{b}	$1.2^{+0.3}_{-0.2}$	$8.16^{+0.08}_{-0.02}$	$9.4^{+0.1}_{-0.1}$	$1.4^{+0.1}_{-0.1}$	$0.59^{+0.08}_{-0.09}$	1.02
4	$1.058^{+0.003}_{-0.003}$	$6.84^{+0.089}_{-0.09}$	$16.62^{+13.8}_{-7.6}$	$33.6^{+2.3}_{-1.8}$	3.21^{a}	4.52^{a}	10.0^{b}	$4.8^{+2.3}_{-1.7}$	$0.1^{+0.1}_{-0.05}$	$9.8^{+0.1}_{-0.2}$	$1.8^{+0.2}_{-0.2}$	$1.5^{+0.3}_{-0.3}$	1.10
5	$1.035^{+0.001}_{-0.001}$	$6.09^{+0.2}_{-0.01}$	$32.42^{+8.7}_{-5.6}$	$34.49^{+2.8}_{-2.7}$	$3.37^{+0.01}_{-0.1}$	4.7^{b}	$9.13^{+0.8}_{-0.7}$	34.06^{a}	$0.0127^{+0.0007}_{-0.0007}$	$10.03^{+0.04}_{-0.04}$	$1.95^{+0.03}_{-0.03}$	$2.29^{+0.04}_{-0.04}$	1.03
8	$0.962^{+0.002}_{-0.001}$	$6.20^{+0.08}_{-0.04}$	$41.9^{+32.3}_{-12.9}$	$37.3^{+3.1}_{-5.2}$	$3.37^{+0.02}_{-0.19}$	4.7^{b}	10.0^{b}	11.86^{a}	$0.013^{+0.006}_{-0.001}$	$9.95^{+0.14}_{-0.07}$	$1.76^{+0.03}_{-0.06}$	$2.53^{+0.06}_{-0.05}$	1.17
9	$0.949^{+0.001}_{-0.002}$	$6.15^{+0.01}_{-0.1}$	81.35^{a}	$43.5^{+6.2}_{-6.3}$	$3.16^{+0.03}_{-0.07}$	4.7^{b}	10.0^{b}	14.58^{a}	$0.0031^{+0.0003}_{-0.0003}$	$9.94^{+0.03}_{-0.09}$	$1.72^{+0.02}_{-0.03}$	$2.54^{+0.04}_{-0.08}$	1.12
11	$0.923^{+0.002}_{-0.002}$	$6.4^{+0.1}_{-0.1}$	22.45^{a}	$39.5^{+6.1}_{-2.8}$	$2.39^{+0.1}_{-0.04}$	$2.6^{+0.2}_{-0.4}$	10.0^{b}	$2.6^{+0.4}_{-0.4}$	$0.007^{+0.006}_{-0.002}$	$9.22^{+0.1}_{-0.08}$	$1.48^{+0.1}_{-0.05}$	$1.2^{+0.2}_{-0.1}$	1.04
12	$0.90^{+0.01}_{-0.01}$	$6.3^{+0.5}_{-0.4}$	9.04^{a}	$30.1^{+4.1}_{-4.4}$	$2.24^{+0.06}_{-0.04}$	$3.6^{+0.4}_{-0.3}$	8.90^{a}	$0.5^{+0.2}_{-0.2}$	$0.03^{+0.03}_{-0.01}$	$8.6^{+0.3}_{-0.3}$	$1.3^{+0.3}_{-0.3}$	$0.4^{+0.3}_{-0.2}$	1.01
15	$0.903^{+0.005}_{-0.005}$	$6.0^{+0.2}_{-0.2}$	32.3^{a}	21.05^{a}	$1.96^{+0.06}_{-0.08}$	$3.3^{+0.3}_{-0.3}$	10.0^{b}	$0.4^{+0.3}_{-0.2}$	$0.004^{+0.002}_{-0.001}$	$9.06^{+0.09}_{-0.13}$	$1.3^{+0.1}_{-0.1}$	$0.9^{+0.2}_{-0.2}$	1.10
16	$0.898^{+0.01}_{-0.008}$	$5.9^{+0.3}_{-0.2}$	26.0^{a}	$32.8^{+27}_{-6.8}$	$2.0^{+0.1}_{-0.1}$	$3.3^{+0.4}_{-0.6}$	10.0^{b}	$0.6^{+0.3}_{-0.2}$	$0.005^{+0.004}_{-0.001}$	$8.8^{+0.1}_{-0.1}$	$1.3^{+0.2}_{-0.2}$	$0.9^{+0.3}_{-0.3}$	1.04

[a] Parameter uncertainty can't be estimated.

[b] Parameter hits the boundary.

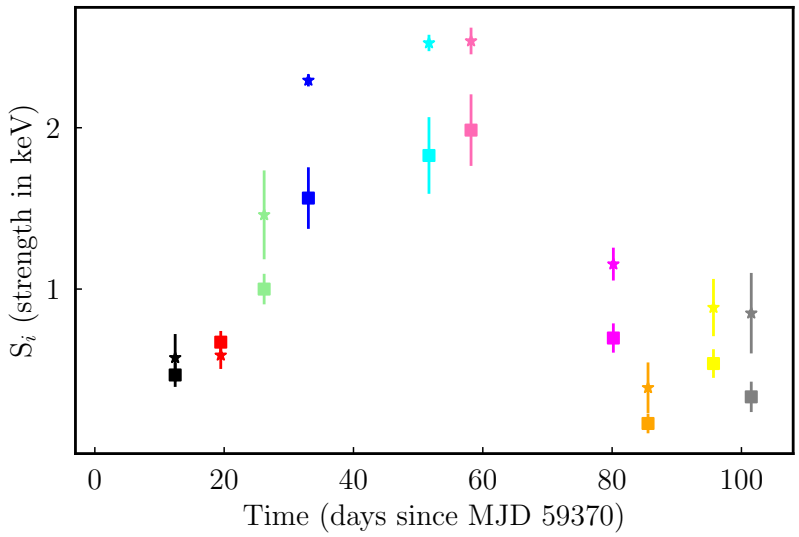

Figure 5.2: Evolution of `gabs strength` (S_i) estimated from *NuSTAR* using the models `tbabs(thcomp×diskbb)edge×gab` (square) and `tbabs(diskbb+relxilllp)×gabs` (star).

5.2 Possible Origin of the Absorption Feature

In general, the absorption features in the spectrum could be due to multiple reasons, such as the presence of obscuring cloud in the line-of-sight, occultation due to the companion star, strong accretion disc wind and/or the stellar wind from the companion (Miller et al., 2008; Szostek & Zdziarski, 2008; Koljonen & Tomsick, 2020).

We used a partial covering fraction absorption model `pcfabs`[1] in *XSPEC* to check if this strong absorption feature can be due to an intervening absorber, but it did not improve the fitting, and the low-energy residuals were high. Therefore, we discard the chances of absorption due to obscuring clouds in the line of sight.

If the absorption feature is produced by the occultation or stellar wind of the binary companion, it must show some orbital variations. Precise diagnostic of the orbital variations provides significant insight into the understanding of the absorption features' nature and origin.

5.2.1 Investigating Orbital Variations of Absorption

Each epoch of *NuSTAR* observation consists of multiple GTIs, referred to as GTI-patches. We consider GTIs with an exposure time greater than 500 sec for the study. However,

[1] `https://heasarc.gsfc.nasa.gov/xanadu/xspec/manual/XSmodelPcfabs.html`

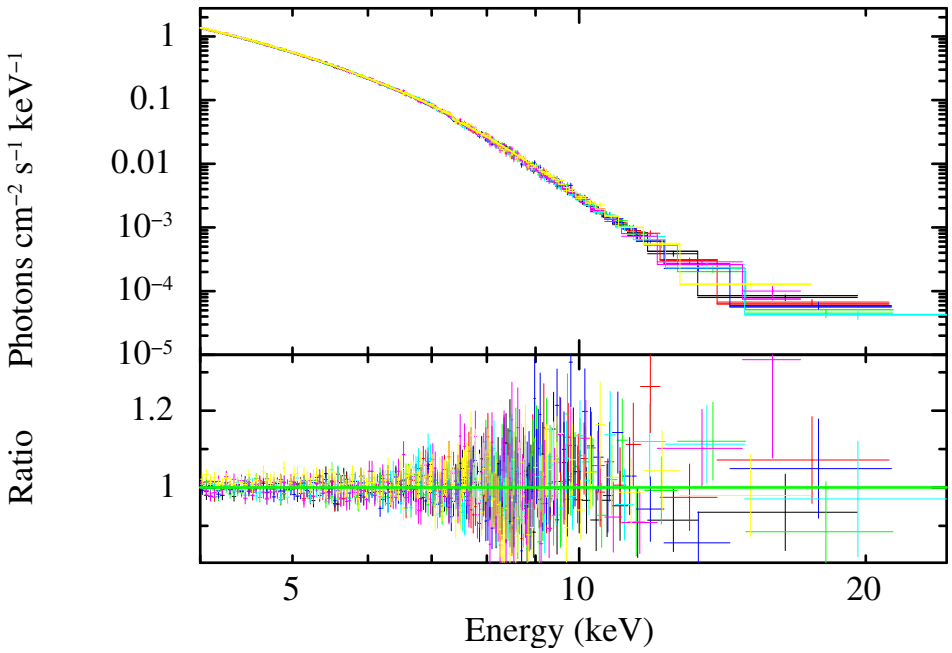

Figure 5.3: Folded spectra of different patches in *NuSTAR* observation of Epoch 9 using the model `tbabs(thcomp×diskbb)edge×gab`. The parameters are tied between the GTI-patches except for the `gabs strength`. See text for details.

for those with lower exposure times, we merge them together as single GTI-patches. We extracted spectrum from individual GTI-patch under each *NuSTAR* observation epoch, and grouped the spectrum with 30 counts per bin. We performed a simultaneous joint spectral fitting of all the GTI-patches under each epoch using the model M1. All parameters are tied between the GTI-patches except `gabs strength` in the joint fitting. Fig. 5.3 shows the simultaneous joint fitting spectra of Epoch 9, which has 7 GTI-patches. The black, red, green, blue, cyan, magenta and yellow colours represent them in the ascending order of time.

We have estimated the `gabs strength` (say, S_p) corresponding to each GTI-patch for a given epoch from the simultaneous joint fitting of the patch spectra. The residual `strength` (S_p - S_i) is estimated for each GTI-patch inside an epoch and is plotted against the orbital phase in Fig. 5.4. As mentioned, S_i (square symbol in Fig. 5.2) is estimated using the same model M1 for an epoch. The binary orbital period (P) of 4U 1543 – 47 is 26.79377 ± 0.00007 hours (Orosz et al., 1998; Orosz, 2003). The orbital position of each *NuSTAR* GTI-patch has been identified based on the start time (MJD 59382.42) of Epoch 1 as the reference time. For Epoch 12 (orange square in Fig. 5.2), the value of S_i is unusually

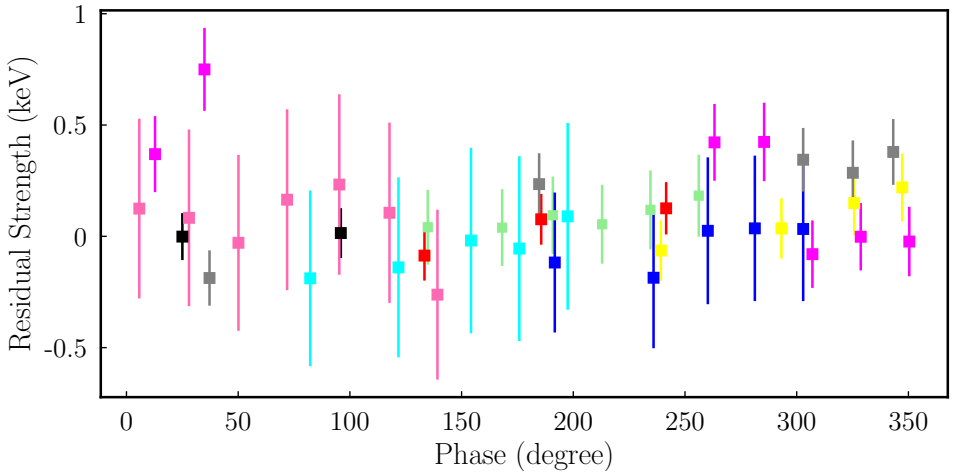

Figure 5.4: The residual strength (S_p - S_i) for different patches in each *NuSTAR* epoch with the orbital phase. The black, red, green, blue, cyan, pink, magenta, orange, yellow and grey represent the *NuSTAR* epochs in chronological order. See text for details.

low, and the estimated S_p from the patch-spectra modelling of this epoch is not reliable. Therefore, we ignore Epoch 12 in Fig. 5.4. The residual varies within ±0.5 keV (except one GTI-patch), and we see only a marginal variation (within uncertainties) in `strength` within an orbit. This implies that the orbital position of the BH and the companion is not responsible for the dynamic nature of the absorption features. We do not expect such behaviour for a low-inclination system.

5.2.2 Role of Companion's Stellar Wind

The X-ray luminosity of the source at the peak (see Epoch 1 in Table 4.2) of the outburst is extremely high, and it may irradiate (see §1.5) the outer accretion disc and the companion star. If the irradiation affects the companion star, either a fresh accretion of matter starts at the hot spot or enhances the stellar wind in the companion star. The former may produce multiple triggering in the same outburst event, which has been observed, for example, in GX 339 − 4 (Aneesha et al., 2019). If the latter happens, the highly ionized wind material may absorb the X-ray emission from the primary to produce the broad absorption feature. The companion of 4U 1543 − 47 is an A2V type star with a mass M_s=2.45 $M_\odot$ (Russell et al., 2006) and radius R_s=2.84 $R_\odot$ (Orosz et al., 1998). The escape velocity of the stellar material from the companion's surface is calculated as 573 km s^{-1}. The binary separation (a) between the BH and the companion is estimated as 7.18 $\times 10^{11}$ cm by considering a BH mass, M_{BH}=9.4 $M_\odot$ (Russell et al., 2006) using the relation $P^2/a^3 = 4\pi^2/ G(M_{BH} + M_s)$,

where G is the Gravitational constant. Therefore, the stellar wind takes only a few hours to reach the primary. The column density of stellar wind and the ionization state should reduce with the decrease of the X-ray luminosity of the primary. Therefore, we expect that the strength of the broad absorption feature should reduce along with the progress of the outburst. Instead, we observe that the absorption strength enhances and becomes strongest during Epoch 9. Moreover, the estimated stellar wind speed is insufficient to blueshift even the highest ionized lines of Fe XXVI to produce the observed absorption feature. Therefore, the stellar wind has no role in the dynamic absorption features in the spectra of 4U 1543−47.

5.2.3 Signature of Accretion Disc Wind in 4U 1543−47

As discussed in §1.7, accretion disc wind is generally observed in the HSS state where the central X-ray luminosity of the source remains very high. The central X-ray photons can irradiate the outer accretion disc enhancing the accretion rate, and the disc remains in the hot phase longer. Therefore, the outburst source stays in the high luminosity state for a longer duration (King, 1998; Lasota, 2001; Aneesha et al., 2019; Aneesha & Mandal, 2020). This is possibly causing the 2021 outburst of 4U 1543 – 47 to decline very slowly, over ∼ 175 days (see Fig. 4.1). The super Eddington peak luminosity (Epoch 1 in Table 4.2) of the XRB source can launch strong disc wind (e.g., King et al. (2015); Muñoz-Darias et al. (2018)). The accretion disc wind is more prominent in the soft state of X-ray binaries (Miller et al., 2008; Neilsen & Lee, 2009; Ponti et al., 2012), though disc winds are not exclusively confined to soft spectral state (Lee et al., 2002). Spectral analysis of 4U 1543−47 (Table 4.2) suggests that the source was in the HSS during our study. Also, we notice spectral softening happens till Epoch 9 (∼ day 60) and beyond which spectra gradually become harder (Table 4.2 & Table 4.3). Also, the reflection modelling parameters (Table 5.2) suggest a highly ionized accretion disc. If the ionized disc wind is responsible for the absorption feature, then the strength of the features would be maximum when the source is softest. Surprisingly the *strength* of the absorption feature is maximum on ∼ day 60 as per our analysis (pink points in Fig. 5.2), and it is keeps-on decreasing further. The optical depth (τ) evolution (Fig. 4.4c) also suggests that the absorption column is maximum on ∼ day 60.

The transition energy of the most ionized line with the highest absorption yield, i.e., Fe XXV and Fe XXVI, are 6.68 keV and 6.97 keV respectively (provided by `XSTAR` line finding list[2]). Assuming the absorption feature (with *line E* ∼ 10 keV) in the *NuSTAR* spectra is produced due to the absorption of the accretion disc photons by the highly ionized

[2] `https://heasarc.gsfc.nasa.gov/docs/software/xstar/xstar.html`

blueshifted disc wind. The estimated wind speed is reaching 30% of the speed of light to blueshift the Fe XXVI line energy to 10 keV. Such a fast disc wind has never been observed in X-ray binary systems. Miller et al. (2006) and Kosec et al. (2020) found disc winds in the range of a few hundred to a few thousand km/s. Also, a highly ionized wind is never detected in low-inclination BH-XRB systems (Ponti et al., 2012); for example, GX 339 – 4, XTE J1817 − 330, 4U 1957 + 115, XTE J1650 − 500, GRS 1758 − 258 etc. Therefore, this detection is the first of its kind for X-ray binaries. However, mildly relativistic disc wind is not uncommon in quasars, ultra-luminous X-ray sources and AGNs (Reeves et al., 2009; Tombesi et al., 2015; Walton et al., 2016; Pinto et al., 2017; Hagino et al., 2017). The other difficulty is the width (σ) of the absorption feature, which is as broad as 1.95 keV (Table 5.2). Known line-broadening processes due to turbulence or scattering will face serious challenges in explaining the line width if it is from a single line. Instead, it is more likely that a forest of lines of various ionization states of iron can produce the broad feature.

5.3 Evolution of the Absorption Features

The phenomenological spectral fitting of *NuSTAR* data with model M1 reveals the presence of neutral Fe K_α absorption edge (Table 5.1) and the broad ionized absorption features. We calculate the equivalent width (EW), which is a measure of the strength of an absorption line, of both absorption features to find if there exists any connection between these two components. The EW is defined as (Arumugasamy et al., 2018),

$$EW = \int_0^\infty [1 - I(E)]\ dE, \tag{5.1}$$

where the energy-dependent function $I(E)$ for the `gabs` and `edge` components are given in Equation 2.8 and Equation 2.9 respectively.

The evolution of EW calculated based on *NuSTAR* phenomenological modelling is shown in Fig. 5.5 for both `edge` (red) and `gabs` (blue) components. The `gabs` EW increases till Epoch 9 and then gradually declines, except in Epoch 12. The implication of this result and the connection between both components (`gabs` and `edge`) are discussed in §5.4.

5.4 Discussion

The extreme central luminosity (last column of Table 4.2), high $\log \xi$, and an overabundance of Fe (parameter A_{Fe} in Table 5.2) suggest that the disc is highly ionized with a significant

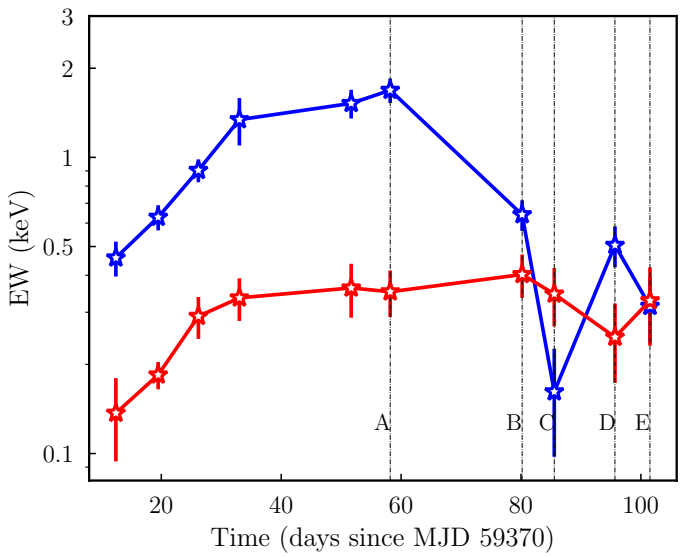

Figure 5.5: Evolution of equivalent width of `gabs` (blue in colour) and `edge` (red in colour) components from the *NuSTAR* epochs. The vertical lines (A-E) are used to describe the figure.

yield of Fe XXV, Fe XXVI etc. A broad, symmetric, and dynamic absorption feature in the spectrum is an important aspect of this outburst. We have presented various possibilities regarding the origin of this feature in §5.2. Finally, we conclude that a fast-moving ionized disc wind could absorb the primary X-ray photons and produce this broad absorption feature. Usually, the disc winds are observed in high inclination ($60^\circ \lesssim \theta \lesssim 80^\circ$) XRB systems (Frank et al., 1987; Ponti et al., 2012). Such systems may show intensity 'dips' in their X-ray spectra, e.g., GRS 1915 + 105, 4U 1630 – 47, H 1743 – 322, MAXI J1305 – 704, GRO J1655 – 40, MAXI J1820+070, etc. (Leahy, 1997; Kuulkers et al., 1998; Shidatsu et al., 2013; Kajava et al., 2019). The dips are believed to be caused by obscuring material associated with the accretion disc (Frank et al., 1987).

The phenomenological modelling of the *NuSTAR* data shows the presence of a neutral Fe Kα absorption (`edge`) at $\sim 7.1 - 7.4$ keV, originating from the outer part of the accretion disc. The initial steep rise of the EW of the neutral component (red star in Fig. 5.5) indicates the enhancement of disc matter due to irradiation of the outer disc by the super Eddington central luminosity. Due to the availability of more matter, the radiation pressure in the highly luminous inner part could release more ionized matter. The source enters the HSS, and the disc wind gradually becomes very active till Epoch 9 (possibly Epoch 10 also), where the `gabs` EW is maximum (marked A in Fig. 5.5), and the disc spectrum is the softest (Fig. 4.4b). Therefore, the evolution of the ionized EW (blue square in Fig. 5.5)

followed the neutral component till day 60 (Epoch 9). If most of the accreted matter is released as the disc wind, the amount of matter that transfers to the inner disc for falling onto the BH is much less. Therefore, the accretion process is regulated by the disc wind. After that, the EW of the ionized component declines gradually (AB in Fig. 5.5) because the disc luminosity has reduced significantly, and a good fraction of inner disc matter has already been lost in the form of wind. The neutral component remains unaffected as it takes a viscous timescale to propagate the same to the outer disc.

The *NuSTAR* data on Epoch 12 reveals a sudden drop of the strength (orange points in Fig. 5.2) and EW (marked 'C' in Fig. 5.5) of `gabs` component. We also notice the same signature in the *AstroSat* data on Epoch 13, observed after 2 days of the *NuSTAR*'s Epoch 12 observation. The `gabs strength` (Table 4.2) on Epoch 13 is smaller by a few factors compared to the nearby observations. We identify this sudden drop of ionized EW can be due to the evacuation of the inner disc. The huge central luminosity may slow the accretion onto the central object, and most of the accreted matter is released through disc wind. Once the disc luminosity reduces, there is a sudden infall of matter onto the BH, leading to an evacuation of the inner disc.

If this interpretation is correct, we expect a relatively harder spectrum due to a significant drop in soft photon flux during Epochs 12 & 13. To characterise this, we calculate the observed flux in $0.5 - 7$ keV (soft) and $7 - 20$ keV (hard) band for *NuSTAR* and *AstroSat* data. The *AstroSat* soft and hard fluxes on Epoch 10 are 7.45×10^{-8} erg cm^{-2} s^{-1} and 1.23×10^{-9} erg cm^{-2} s^{-1} respectively. The drop of *AstroSat* soft flux on the next observation (Epoch 13) is 14%, whereas the hard flux increases by 5%. This resulted in a relatively harder spectral index (marked by a blue circle in Fig. 4.4b) on Epoch 13. Similarly, the *NuSTAR* soft (extending the response to low-energy) and hard fluxes on Epoch 11 are 6.48×10^{-8} erg cm^{-2} s^{-1} and 1.1×10^{-9} erg cm^{-2} s^{-1} respectively. The drop of *NuSTAR* soft flux on Epoch 12 is 10%, whereas the hard flux increases by a factor of 2. Therefore, the suddenly enhanced accretion at the inner disc resulted in these dramatic changes in the EW and spectral properties. Also, *AstroSat/LAXPC* data on Epoch 14 (after 4 days) showed the presence of a strong QPO at 2.45 ± 0.08 Hz (Fig. 4.9). The appearance of QPO possibly supports this transient activity at the inner disc. However, the inner accretion disc recovers over the next 10 days (marked CD) due to the transfer of matter from the outer disc and the ionized component returns to a gradual declination. Interestingly, the neutral component (or the outer disc) follows the same trend as the ionized component, namely the decline and refilling signature (red stars between BE), with a delay of the typical viscous timescale of $10 - 15$ days.

5.5 Summary and Conclusion

The absorption features between $\sim 8 - 11$ keV are thoroughly investigated using the spectral modelling of *NuSTAR* observations. We search for the origin of this feature and its implications in the accretion process. The results found are astounding and are listed below.

- The detection of a broad, dynamic absorption feature at $\sim 8 - 11$ keV is the first of its kind for X-ray binaries. We propose that this feature is due to the absorption of the accretion disc photons by the blueshifted disc wind. The extreme luminosity, high ionization ($\log \xi > 3$), and an overabundance of iron ($3.6 - 10\ A_{Fe,\odot}$) reveal that the disc wind is highly ionized with a significant yield of highly ionized iron species. The strength of the ionized absorption feature (Table 5.1 & Table 5.2) increases between Epoch 1 to Epoch 9 as the disc wind column density is expected to increase with the spectral softening of the source.

- The observed line energy of the absorption feature suggests an estimated wind speed of nearly 30% of the speed of light to blueshift the most ionized line with the highest absorption yield like Fe XXVI. Hence it would become the first X-ray binary source to show a highly relativistic disc wind.

- The initial steep rise of the neutral component EW (red star in Fig. 5.5) indicates the enhancement of disc matter due to irradiation of the outer disc. It enhances the accretion rate; hence, the source remains in the high luminosity and decays very slowly.

- The evolution of EW (Fig. 5.5) of the neutral absorption component (`edge`) and the same of the ionized component (`gabs`) follow each other with a delay of the typical viscous timescale of $10 - 15$ days.

- An evacuation of the inner accretion disc is observed during Epoch $12 - 13$. This event leaves a signature of the drop in the soft photon flux and an enhancement of hard flux. Therefore, the spectrum becomes relatively harder (blue circle in Fig. 4.4b).

Finally, this study suggests that the disc wind regulates accretion dynamics of 4U $1543 - 47$ during the 2021 outburst.

Chapter 6

Summary and Future Perspectives

Studying the accretion scenario in outbursting black hole X-ray binaries provides insight into the physics of these objects. This study deals with the broadband analysis of two extremely bright BH-XRBs MAXI J1820+070 (bright due to proximity) and 4U 1543−47 (intrinsically luminous) in our galaxy using multi-instrument X-ray data.

In Chapter 1, we have introduced two popular accretion scenarios, namely wind and disc accretion, around compact objects. We briefly discuss the irritated disc instability model to address the outburst events in XRBs. Also, we introduce the general literature on spectral, timing variability, and state classification.

Chapter 2 briefly describes multiple X-ray instruments, data reduction processes, and the methodology followed in the spectral and timing modelling.

We have conducted comprehensive spectral and timing studies of MAXI J1820+070 in its 2018 double outburst (Outburst-I and II) in Chapter 3. We have performed spectral modelling using *NICER* and *Swift/XRT* for the entire outburst duration. Also, we have done wideband spectral studies using simultaneous *NICER-NuSTAR*, *XRT-NuSTAR*, and *AstroSat* observations. Spectral analysis reveals that the accretion disc remains truncated, and the source was in the LHS during Outburst-I. The lightcurve of Outburst-I had a plateau (Phase-II) followed by a gradual decline (Phase-III) after the peak. Phase-II showed spectral softening without changing the thermal component. However, thermal and non-thermal flux decline together in Phase-III, keeping a constant spectral index. Non-thermal photons dominate the Outburst-I, while the Outburst-II is soft and extremely bright. The *NICER* data shows the presence of Fe K_α line during Outburst-I. The HID traces the canonical q-shape and has shown state transitions.

The simultaneous wideband modelling reveals a strong reflection signature in both outbursts, particularly Outburst-II has recorded a very high ionization parameter ($log\,\xi \sim 4$), an overabundance of iron, and high reflection fraction (~ 3.5). We detect a vertical corona,

evolving closer to the BH (Phase II) in the LHS, and it remains closer to the BH during HSS. Therefore, it is believed that the dynamic nature of the corona is responsible for the spectral properties of the system in LHS.

The *NICER* timing analysis showed multiple QPO-like features along with flat-top or powerlaw noise in the power density spectra. The evolution of the characteristic frequency (ν_c) of QPO features reveals that ν_c initially increases (Phase-II) and then decreases (Phase-III) over time (Fig. 3.11a) while the overall flux declines during Outburst-I. Therefore, the evolution of ν_c in Phase-II defies the expectation that the source flux and the characteristic frequency would be correlated in the LHS of outbursting XRB systems (Belloni, 2010). This can be due to the reduction of the size of the corona, keeping a steady thermal component, i.e., the spectral softening observed in Phase-II. The spectral softening and reduction of corona size decrease both cooling and dynamical time. The resonance between these two timescales may generate LFQPOs as suggested by the propagation of the shock oscillation model (Molteni et al., 1996; Chakrabarti et al., 2004, and reference therein) and the QPO frequency is inverse to the oscillation time. However, an opposite trend explains the evolution of ν_c in Phase-III due to the correlated reduction of thermal and non-thermal flux. Also, we find an interesting anti-correlation between the fractional RMS and ν_c for $\nu_c > 2$ Hz in the LHS. This is a signature of type-C QPO and is commonly observed in LHS (Belloni, 2010; Athulya et al., 2022). However, no clear correlation is observed at the lower frequency. The estimated RMS is high ($\sim 40\%$) in the LHS, and the same is $< 1\%$ in the HSS. The total RMS is anti-correlated with the total flux except in Phase-II. Similarly, the spectro-temporal behaviour in HRD shows RMS and HR are anti-correlated except in Phase-II.

The source was accreting only at 5% of its Eddington accretion rate at the peak of the outburst. However, the system seems very bright due to proximity and low column density along the line of sight. The low luminosity and short rise time indicate both outbursts triggered as inside-out propagation of thermo-viscous instability. We propose that the Outburst-II was triggered when the disc was hot and the viscous timescale was short enough for the inner disc to move quickly toward the ISCO and produce bright HSS.

The spectral analysis suggests a vertically elongated corona. In contrast, the evolution of LFQPOs by the propagation of the shock oscillation model suggests a radially extended corona inside the truncated disc in the LHS. It reveals that both models are insufficient for addressing the observed trends. The findings of this study raise questions about our current understanding of coronal geometry and suggest further investigation of the disc-jet geometry around BHs.

We have performed a comprehensive spectral and timing analysis of the 2021 outburst of the source 4U 1543−47 in Chapter 4. We have done wideband spectral and timing studies of simultaneous *NICER-NuSTAR* and *AstroSat* observations. Also, we have done the spectral and timing analysis using all the three instrument data for the entire outburst.

The spectral modelling reveals that the source was super-Eddington at Epoch 1 and is completely soft-photons-dominated due to very little fractional Comptonization ($< 3\%$), low corona temperature, and steep photon index. Therefore, the source was in the HSS throughout the outburst and was the softest on Epoch 9. The inner disc temperature (T_{in}) is highest on Epoch 1 and keeps decreasing during the outburst's decay. The extreme luminosity in the inner accretion disc may slow the accretion of matter through the inner disc, which causes T_{in} to decline. Reflection modelling suggests that 4U 1543−47 is a low-inclination system ($\theta \sim 32^\circ - 40^\circ$) having a highly ionized accretion disc ($\log \xi \gtrsim 3$) with an overabundance of iron. The corona comes closer to the central object as the source becomes softer with an enhancement of the reflection fraction.

The hardness intensity diagram (HID) shows a correlated change of flux and HR with a loop structure due to a momentary drop in the flux just after the peak. The HID suggests that most of the observed flux is contributed by the accretion disc, and therefore as the flux decreases, HR also follows the same trend. HID shape differs from the standard q-shape profile observed in most complete outbursts. Also, the source was in the HSS even during quiescence, in contrast to the standard outbursts.

The timing analysis revealed that the system possesses very low variability in the lightcurves since the source stays in the HSS throughout the outburst. However, *LAXPC* observation on Epoch 14 harbours a strong QPO feature at 2.45±0.08 Hz in 3−10 keV band. The appearance of this QPO is possibly connected with the transient activity (evacuation of the inner accretion disc) on Epoch 13, followed by the refilling of the disc during this period.

The spectra of 4U 1543−47 in 2021 outburst possess a very strong and dynamic absorption feature between $\sim$ 8−11 keV. This detection is the first of its kind for X-ray binaries. A systematic study of the absorption feature is carried out in Chapter 5 to uncover its origin. The extreme luminosity, high ionization, and an overabundance of iron may cause highly ionized disc-wind with a significant yield of highly ionized iron species. The strength of the ionized absorption feature increases between Epoch 1 to Epoch 9 as the disc-wind column density is expected to increase with the spectral softening of the source. The line energy of the observed absorption features points to the relativistic nature of the wind to blueshift the most ionized line with the highest absorption yield, like Fe XXVI. Our results suggest that

the strong and dynamic absorption feature is produced by the absorption of the accretion disc photons by a highly ionized and relativistic (30% speed of light) disc wind in the system.

The *NuSTAR* data also show the presence of a neutral Fe Kα absorption at $\sim 7.1 - 7.4$ keV, originating from the outer part of the accretion disc. The initial steep rise of the neutral component equivalent width (EW) indicates an enhancement of disc matter due to the irradiation of the outer disc. Therefore, the source remains in high luminosity and decays very slowly. The evolution of the EW of the neutral and ionized absorption components suggests that they follow each other with a delay of the typical viscous timescale of 10−15 days. We noticed a clear drop in the EW of the ionized absorption components during Epoch 12−13. This event leaves a signature of the drop in the soft photon flux and an enhancement of hard flux resulting in a relatively harder spectrum. We interpret this as evidence of the evacuation of the inner accretion disc and propose that the QPO observed in the *LAXPC* data on Epoch 14 is connected with this. This study suggests that the disc wind plays a significant role in controlling the accretion dynamics of the 2021 outburst of 4U 1543−47.

Future Perspectives

Our study of 4U 1543−47 revealed strong, dynamic, and broad absorption lines in the spectra, which could be attributed to the relativistic disc wind in the system. The present study utilises phenomenological models to explain the characteristics of the absorption features. An in-depth investigation utilizing physical models for disc wind would enable us to obtain a more realistic picture of the scenario. A few such models are discussed below.

The `DISK-WIND`[1] model (Sim et al., 2008, 2010; Matzeu et al., 2022) in *XSPEC* is widely used to study the properties of disc winds in X-ray binaries, including their origin, dynamics, and the feedback they provide to the accretion disc and the surrounding environment. This model can handle both absorption and emission from a disc wind by calculating the flow's local ionisation state and velocity field. It estimates several parameters, such as the terminal velocity of the wind, mass outflow rate, and X-ray ionizing luminosity, etc. The photoionization model `XSTAR` (Kallman & Bautista, 2001; Kallman et al., 2004) in *XSPEC* is used to model the physical properties of astrophysical plasma. It is suitable to model the absorption signatures of the disc wind and provide information about the ionization state and column density of the wind.

[1] `https://gabrielematzeu.com/disk-wind/`

The broad absorption feature observed in the spectra of 4U 1543-47 is unique in its nature. The typical line width expected for a neutral Fe line is around 50-60 eV (Ueda et al., 2004; Torrejón et al., 2010; Ponti et al., 2019). When these lines are blueshifted by a strong disk wind, they become smeared out. If these lines are coming from a large number of ionized elements, they may get overlap and makes it difficult to differentiate them. If the lines are contributed by only a few elements, there exists a possibility of detecting them. We assume that the very broad ($\sim$ 2 keV) absorption feature observed in 4U 1543-47 could possibly be produced by a forest of lines of varying ionisation states of different elements. Identifying the elements responsible for the multitude of absorption lines that generated the feature would be interesting.

The 2021 outburst of the system 4U 1543−47 is unique, as it only exhibits a soft state and possesses a different (non-canonical) HID than other transient BH sources. We are planning to extend the spectro-temporal study to other sources, particularly soft state dominated, non-canonical outbursts for comparison. Until now, there has been a lack of studies specifically addressing the evolutionary trends of non-canonical outbursts. Consequently, there are numerous open questions regarding these systems. One crucial question is whether a common evolutionary trend exists among non-canonical systems. Furthermore, it is yet to be ascertained whether the unique features witnessed in these systems directly from their non-canonical behavior. In the coming years, our aim is to explore the discrepancies in the outburst HID profile among various sources. We intend to investigate whether sources displaying non-canonical behavior exhibit distinct dynamics during their outbursts. Furthermore, the presence of a disk wind signature in the high soft state (HSS) across various sources raises questions such as: Is there a specific luminosity threshold linked to the emergence of the disk wind? These inquiries could serve as central themes for a research initiative focused on attaining a deeper understanding of the intricate behaviors exhibited by these systems. By conducting a comprehensive spectro-temporal analysis of several such X-ray binary systems, it is possible to explore and uncover potential commonalities or unique aspects of non-canonical outbursts.

Also, I intend to prioritize and focus on X-ray polarization studies of XRB systems. The future of X-ray binary system studies hinges on the integration of spectroscopic, temporal, and polarimetric analyses. The X-ray polarization studies will provide valuable information about the system's geometry, magnetic field orientation, and more. The recent launch of NASA's *Imaging X-ray Polarimetry Explorer (IXPE)* (Weisskopf et al., 2016; Soffitta, 2017) in 2021 and the upcoming ISRO mission *POLIX* (Paul et al., 2016) onboard *XPoSat* offer exceptional prospects in this field.

Bibliography

Abramowicz M. A., Kluźniak W., 2001, A&A, 374, L19

Abramowicz M. A., Czerny B., Lasota J. P., Szuszkiewicz E., 1988, ApJ, 332, 646

Agrawal P. C., et al., 2017, Journal of Astrophysics and Astronomy, 38, 30

Alam M. S., Dewangan G. C., Belloni T., Mukherjee D., Jhingan S., 2014, MNRAS, 445, 4259

Anders E., Grevesse N., 1989, Geochimica Cosmochimica Acta, 53, 197

Aneesha U., Mandal S., 2020, A&A, 637, A47

Aneesha U., Mandal S., Sreehari H., 2019, MNRAS, 486, 2705

Antia H. M., et al., 2017, ApJS, 231, 10

Antia H. M., et al., 2021, Journal of Astrophysics and Astronomy, 42, 32

Antia H. M., Agrawal P. C., Katoch T., Manchanda R. K., Mukerjee K., Shah P., 2022, ApJS, 260, 40

Arumugasamy P., Kargaltsev O., Posselt B., Pavlov G. G., Hare J., 2018, ApJ, 869, 97

Athulya M. P., Radhika D., Agrawal V. K., Ravishankar B. T., Naik S., Mandal S., Nandi A., 2022, MNRAS, 510, 3019

Atri P., et al., 2020, MNRAS, 493, L81

Axelsson M., Veledina A., 2021, MNRAS, 507, 2744

Baby B. E., Agrawal V. K., Ramadevi M. C., Katoch T., Antia H. M., Mandal S., Nandi A., 2020, MNRAS, 497, 1197

Baby B. E., Bhuvana G. R., Radhika D., Katoch T., Mandal S., Nandi A., 2021, MNRAS, 508, 2447

Ballet J., 1999, A&AS, 135, 371

Bambi C., 2016, Astrophysics of Black Holes: From Fundamental Aspects to Latest Developments. Springer Berlin, Heidelberg, doi:10.1007/978-3-662-52859-4

Bambi C., Dolgov A. D., Petrov A. A., 2009, J. Cosmology Astropart. Phys., 2009, 013

Bardeen J. M., Press W. H., Teukolsky S. A., 1972, ApJ, 178, 347

Basko M. M., Sunyaev R. A., Titarchuk L. G., 1974, A&A, 31, 249

Begelman M. C., Meier D. L., 1982, ApJ, 253, 873

Belloni T. M., 2010, States and Transitions in Black Hole Binaries. p. 53, doi:10.1007/978-3-540-76937-8_3

Belloni T., Homan J., Casella P., van der Klis M., Nespoli E., Lewin W. H. G., Miller J. M., Méndez M., 2005, A&A, 440, 207

Belloni T. M., Sanna A., Méndez M., 2012, MNRAS, 426, 1701

Bharali P., Chauhan J., Boruah K., 2019, MNRAS, 487, 5946

Bhargava Y., Belloni T., Bhattacharya D., Motta S., Ponti. G., 2021, MNRAS, 508, 3104

Bhuvana G. R., Radhika D., Agrawal V. K., Mandal S., Nandi A., 2021, MNRAS, 501, 5457

Bhuvana G. R., Radhika D., Nandi A., 2022, Advances in Space Research, 69, 483

Blandford R. D., Payne D. G., 1982, MNRAS, 199, 883

Blandford R. D., Znajek R. L., 1977, MNRAS, 179, 433

Bolton C. T., 1971, in Bulletin of the American Astronomical Society. p. 458

Bolton C. T., 1972, Nature, 235, 271

Bondi H., 1952, MNRAS, 112, 195

Bondi H., Hoyle F., 1944, MNRAS, 104, 273

Bright J., Motta S., Fender R., 2018, The Astronomer's Telegram, 12061, 1

Buisson D., Fabian A., Alston W., Walton D., Kara E., Garcia J., Homan J., Tomsick J., 2018, The Astronomer's Telegram, 11578, 1

Buisson D. J. K., et al., 2019, MNRAS, 490, 1350

Buisson D. J. K., et al., 2021, MNRAS, 500, 3976

Burleigh M. R., Jordan S., 1998, in American Astronomical Society Meeting Abstracts #191. p. 15.11

Burrows D. N., et al., 2005, Space Sci. Rev., 120, 165

Carter B., 1971, Phys. Rev. Lett., 26, 331

Castro-Tirado A. J., Brandt S., Lund N., Lapshov I., Sunyaev R. A., Shlyapnikov A. A., Guziy S., Pavlenko E. P., 1994, ApJS, 92, 469

Chakrabarti S. K., 1990, Theory of Transonic Astrophysical Flows, doi:10.1142/1091.

Chakrabarti S. K., 1996, ApJ, 464, 664

Chakrabarti S. K., 1997, ApJ, 484, 313

Chakrabarti S., Titarchuk L. G., 1995, ApJ, 455, 623

Chakrabarti S. K., Acharyya K., Molteni D., 2004, A&A, 421, 1

Chakrabarti S. K., Debnath D., Nandi A., Pal P. S., 2008, A&A, 489, L41

Chakraborty S., Navale N., Ratheesh A., Bhattacharyya S., 2020, MNRAS, 498, 5873

Chandrasekhar S., 1939, Ciel et Terre, 55, 412

Chaty S., 2011, in Schmidtobreick L., Schreiber M. R., Tappert C., eds, Astronomical Society of the Pacific Conference Series Vol. 447, Evolution of Compact Binaries. p. 29 (arXiv:1107.0231), doi:10.48550/arXiv.1107.0231

Corbel S., Nowak M. A., Fender R. P., Tzioumis A. K., Markoff S., 2003, A&A, 400, 1007

Corbel S., Coriat M., Brocksopp C., Tzioumis A. K., Fender R. P., Tomsick J. A., Buxton M. M., Bailyn C. D., 2013, MNRAS, 428, 2500

Coriat M., Fender R. P., Dubus G., 2012, MNRAS, 424, 1991

Cunningham C. T., 1975, ApJ, 202, 788

Dauser T., Wilms J., Reynolds C. S., Brenneman L. W., 2010, MNRAS, 409, 1534

Dauser T., Garcia J., Wilms J., Böck M., Brenneman L. W., Falanga M., Fukumura K., Reynolds C. S., 2013, MNRAS, 430, 1694

Dauser T., García J., Walton D. J., Eikmann W., Kallman T., McClintock J., Wilms J., 2016, A&A, 590, A76

De Marco B., Zdziarski A. A., Ponti G., Migliori G., Belloni T. M., Segovia Otero A., Dziełak M. A., Lai E. V., 2021, A&A, 654, A14

Debnath D., Molla A. A., Chakrabarti S. K., Mondal S., 2015, ApJ, 803, 59

Deegan P., Combet C., Wynn G. A., 2009, MNRAS, 400, 1337

Deka K., Shah Z., Misra R., Ahmed G. A., 2021, Journal of High Energy Astrophysics, 31, 23

Denisenko D., 2018, The Astronomer's Telegram, 11400, 1

Done C., Gierliński M., Kubota A., 2007, A&ARv, 15, 1

Dong Y., García J. A., Steiner J. F., Gou L., 2020, MNRAS, 493, 4409

Draghis P. A., Miller J. M., Zoghbi A., Reynolds M., Costantini E., Gallo L. C., Tomsick J. A., 2022, arXiv e-prints, p. arXiv:2210.02479

Dziełak M. A., De Marco B., Zdziarski A. A., 2021, MNRAS, 506, 2020

Ebisawa K., 1997, in Makino F., Mitsuda K., eds, X-Ray Imaging and Spectroscopy of Cosmic Hot Plasmas. p. 427

Ebisawa K., et al., 1994, PASJ, 46, 375

Fabian A. C., Rees M. J., Stella L., White N. E., 1989, MNRAS, 238, 729

Fabian A. C., Iwasawa K., Reynolds C. S., Young A. J., 2000, PASP, 112, 1145

Fabian A. C., et al., 2020, MNRAS, 493, 5389

Farr W. M., Sravan N., Cantrell A., Kreidberg L., Bailyn C. D., Mandel I., Kalogera V., 2011, ApJ, 741, 103

Fender R. P., Belloni T. M., Gallo E., 2004, MNRAS, 355, 1105

Fender R. P., Homan J., Belloni T. M., 2009, MNRAS, 396, 1370

Frank J., King A. R., Lasota J. P., 1987, A&A, 178, 137

Frank J., King A., Raine D., 1992, Accretion power in astrophysics.. Vol. 21

Fürst F., et al., 2015, ApJ, 808, 122

Galeev A. A., Rosner R., Vaiana G. S., 1979, ApJ, 229, 318

Gallo E., Fender R. P., Pooley G. G., 2003, MNRAS, 344, 60

García J., Kallman T. R., 2010, ApJ, 718, 695

García J., Dauser T., Reynolds C. S., Kallman T. R., McClintock J. E., Wilms J., Eikmann W., 2013, ApJ, 768, 146

García J., et al., 2014, ApJ, 782, 76

García J. A., et al., 2019, ApJ, 885, 48

Garg A., et al., 2021, The Astronomer's Telegram, 14749, 1

Gehrels N., et al., 2004, ApJ, 611, 1005

Gendreau K. C., et al., 2016, in den Herder J.-W. A., Takahashi T., Bautz M., eds, Society of Photo-Optical Instrumentation Engineers (SPIE) Conference Series Vol. 9905, Space Telescopes and Instrumentation 2016: Ultraviolet to Gamma Ray. p. 99051H, doi:10.1117/12.2231304

George I. M., Fabian A. C., 1991, MNRAS, 249, 352

Giacconi R., Kellogg E., Gorenstein P., Gursky H., Tananbaum H., 1971, ApJ, 165, L27

Giacconi R., et al., 1979, ApJ, 230, 540

Gilfanov M., 2010, in Belloni T., ed., , Vol. 794, Lecture Notes in Physics, Berlin Springer Verlag. p. 17, doi:10.1007/978-3-540-76937-8_2

Gonzalez A. G., Wilkins D. R., Gallo L. C., 2017, MNRAS, 472, 1932

Grinberg V., et al., 2017, A&A, 608, A143

Guan J., et al., 2021, MNRAS, 504, 2168

Gursky H., Kellogg E. M., Leong C., Tananbaum H., Giacconi R., 1971, ApJ, 165, L43

Haardt F., Maraschi L., 1991, ApJ, 380, L51

Haardt F., Maraschi L., 1993, ApJ, 413, 507

Hagino K., Done C., Odaka H., Watanabe S., Takahashi T., 2017, MNRAS, 468, 1442

Harmon B. A., Wilson R. B., Finger M. H., Paciesas W. S., Rubin B. C., Fishman G. J., 1992, IAU Circ., 5504, 1

Harrison F. A., et al., 2013, ApJ, 770, 103

Heil L. M., Vaughan S., Uttley P., 2012, MNRAS, 422, 2620

Homan J., Belloni T., 2005, Ap&SS, 300, 107

Homan J., et al., 2020, ApJ, 891, L29

Hoyle F., Lyttleton R. A., 1939, Proceedings of the Cambridge Philosophical Society, 35, 405

Ingram A. R., Motta S. E., 2019, New Astron. Rev., 85, 101524

Israel W., 1967, Physical Review, 164, 1776

Israel W., 1968, Communications in Mathematical Physics, 8, 245

Jana A., Jaisawal G. K., Naik S., Kumari N., Chhotaray B., Altamirano D., Remillard R. A., Gendreau K. C., 2021, MNRAS, 504, 4793

Jansen F., et al., 2001, A&A, 365, L1

Jonker P. G., Nelemans G., 2004, MNRAS, 354, 355

Kajava J. J. E., Motta S. E., Sanna A., Veledina A., Del Santo M., Segreto A., 2019, MNRAS, 488, L18

Kallman T., Bautista M., 2001, ApJS, 133, 221

Kallman T. R., Palmeri P., Bautista M. A., Mendoza C., Krolik J. H., 2004, ApJS, 155, 675

Kara E., et al., 2019, Nature, 565, 198

Katoch T., Baby B. E., Nandi A., Agrawal V. K., Antia H. M., Mukerjee K., 2021, MNRAS, 501, 6123

Kawamura T., Axelsson M., Done C., Takahashi T., 2022, MNRAS,

Kawamuro T., et al., 2018, The Astronomer's Telegram, 11399, 1

Kerr R. P., 1963, Phys. Rev. Lett., 11, 237

Kilic M., Allende Prieto C., Brown W. R., Koester D., 2007, ApJ, 660, 1451

King A. R., 1998, MNRAS, 296, L45

King A. L., Miller J. M., Raymond J., Reynolds M. T., Morningstar W., 2015, ApJ, 813, L37

Kitamoto S., Miyamoto S., Tsunemi H., Makishima K., Nakagawa M., 1984, PASJ, 36, 799

Koljonen K. I. I., Tomsick J. A., 2020, A&A, 639, A13

Kosec P., Fabian A. C., Pinto C., Walton D. J., Dyda S., Reynolds C. S., 2020, MNRAS, 491, 3730

Kotani T., et al., 1997, in Dermer C. D., Strickman M. S., Kurfess J. D., eds, American Institute of Physics Conference Series Vol. 410, Proceedings of the Fourth Compton Symposium. pp 922–926, doi:10.1063/1.53963

Kotani T., Ebisawa K., Dotani T., Inoue H., Nagase F., Tanaka Y., Ueda Y., 2000, ApJ, 539, 413

Kretschmar P., et al., 2019a, New Astron. Rev., 86, 101546

Kretschmar P., et al., 2019b, Mem. Soc. Astron. Italiana, 90, 221

Kubota A., Tanaka Y., Makishima K., Ueda Y., Dotani T., Inoue H., Yamaoka K., 1998, PASJ, 50, 667

Kumar R., Chattopadhyay I., Mandal S., 2014, MNRAS, 437, 2992

Kuulkers E., Wijnands R., Belloni T., Méndez M., van der Klis M., van Paradijs J., 1998, ApJ, 494, 753

Lasota J.-P., 2001, New Astron. Rev., 45, 449

Lasota J.-P., 2016, in Bambi C., ed., Astrophysics and Space Science Library Vol. 440, Astrophysics of Black Holes: From Fundamental Aspects to Latest Developments. p. 1 (arXiv:1505.02172), doi:10.1007/978-3-662-52859-4_1

Lattimer J. M., 2012, Annual Review of Nuclear and Particle Science, 62, 485

Leahy D. A., 1997, MNRAS, 287, 622

Leahy D. A., Darbro W., Elsner R. F., Weisskopf M. C., Sutherland P. G., Kahn S., Grindlay J. E., 1983, ApJ, 266, 160

Lee J. C., Reynolds C. S., Remillard R., Schulz N. S., Blackman E. G., Fabian A. C., 2002, ApJ, 567, 1102

Li L.-X., Zimmerman E. R., Narayan R., McClintock J. E., 2005, ApJS, 157, 335

Lightman A. P., White T. R., 1988, ApJ, 335, 57

Lynden-Bell D., 1969, Nature, 223, 690

Ma X., et al., 2021, Nature Astronomy, 5, 94

Maccarone T. J., Coppi P. S., 2003, MNRAS, 338, 189

Madsen K. K., Beardmore A. P., Forster K., Guainazzi M., Marshall H. L., Miller E. D., Page K. L., Stuhlinger M., 2017, AJ, 153, 2

Madsen K. K., et al., 2021, arXiv e-prints, p. arXiv:2111.01613

Makishima K., 1986, in Mason K. O., Watson M. G., White N. E., eds, , Vol. 266, The Physics of Accretion onto Compact Objects. p. 249, doi:10.1007/3-540-17195-9_14

Makishima K., Maejima Y., Mitsuda K., Bradt H. V., Remillard R. A., Tuohy I. R., Hoshi R., Nakagawa M., 1986, ApJ, 308, 635

Malzac J., Dumont A. M., Mouchet M., 2005, A&A, 430, 761

Marino A., et al., 2021, A&A, 656, A63

Martocchia A., Matt G., 1996, MNRAS, 282, L53

Mastroserio G., et al., 2021, MNRAS, 507, 55

Matilsky T. A., Giacconi R., Gursky H., Kellogg E. M., Tananbaum H. D., 1972, ApJ, 174, L53

Matt G., Fabian A. C., Ross R. R., 1993, MNRAS, 262, 179

Matzeu G. A., et al., 2022, MNRAS, 515, 6172

McClintock J. E., Remillard R. A., 2006, Black hole binaries. pp 157–213

Melia F., 2009, High-energy astrophysics. Princeton University Press

Menou K., Hameury J.-M., Lasota J.-P., Narayan R., 2000, MNRAS, 314, 498

Merloni A., et al., 2012, arXiv e-prints, p. arXiv:1209.3114

Miller-Jones J. C. A., et al., 2019, Nature, 569, 374

Miller J. M., Raymond J., Fabian A., Steeghs D., Homan J., Reynolds C., van der Klis M., Wijnands R., 2006, Nature, 441, 953

Miller J. M., Raymond J., Reynolds C. S., Fabian A. C., Kallman T. R., Homan J., 2008, ApJ, 680, 1359

Miller J. M., Reynolds C. S., Fabian A. C., Miniutti G., Gallo L. C., 2009, ApJ, 697, 900

Mirabel I. F., Rodrigues I., 2003, A&A, 398, L25

Mirabel I. F., Rodríguez L. F., 1994, Nature, 371, 46

Mirabel I. F., Mignani R., Rodrigues I., Combi J. A., Rodríguez L. F., Guglielmetti F., 2002, A&A, 395, 595

Mitsuda K., et al., 1984, PASJ, 36, 741

Miyamoto S., Kitamoto S., 1991, ApJ, 374, 741

Miyamoto S., Kitamoto S., Hayashida K., Egoshi W., 1995, ApJ, 442, L13

Molteni D., Sponholz H., Chakrabarti S. K., 1996, ApJ, 457, 805

Morgan E. H., Remillard R. A., Greiner J., 1997, ApJ, 482, 993

Morningstar W. R., Miller J. M., 2014, ApJ, 793, L33

Motta S. E., 2016, Astronomische Nachrichten, 337, 398

Motta S., Muñoz-Darias T., Casella P., Belloni T., Homan J., 2011, MNRAS, 418, 2292

Motta S., Homan J., Muñoz Darias T., Casella P., Belloni T. M., Hiemstra B., Méndez M., 2012, MNRAS, 427, 595

Motta S. E., Franchini A., Lodato G., Mastroserio G., 2018, MNRAS, 473, 431

Muñoz-Darias T., Motta S., Stiele H., Belloni T. M., 2011, MNRAS, 415, 292

Muñoz-Darias T., et al., 2016, Nature, 534, 75

Muñoz-Darias T., Torres M. A. P., Garcia M. R., 2018, MNRAS, 479, 3987

Muñoz-Darias T., et al., 2019, ApJ, 879, L4

Mudambi S. P., Maqbool B., Misra R., Hebbar S., Yadav J. S., Gudennavar S. B., S. G. B., 2020, ApJ, 889, L17

Narayan R., Yi I., 1994, ApJ, 428, L13

Narayan R., Yi I., 1995a, ApJ, 444, 231

Narayan R., Yi I., 1995b, ApJ, 452, 710

Negoro H., et al., 2021a, The Astronomer's Telegram, 14701, 1

Negoro H., et al., 2021b, The Astronomer's Telegram, 14708, 1

Neilsen J., 2013, Advances in Space Research, 52, 732

Neilsen J., Lee J. C., 2009, Nature, 458, 481

Neilsen J., Coriat M., Fender R., Lee J. C., Ponti G., Tzioumis A. K., Edwards P. G., Broderick J. W., 2014, ApJ, 784, L5

Niedźwiecki A., Zdziarski A. A., Szanecki M., 2016, ApJ, 821, L1

Okajima T., et al., 2016, in den Herder J.-W. A., Takahashi T., Bautz M., eds, Society of Photo-Optical Instrumentation Engineers (SPIE) Conference Series Vol. 9905, Space Telescopes and Instrumentation 2016: Ultraviolet to Gamma Ray. p. 99050Z, doi:10.1117/12.2231705

Orosz J. A., 2003, in van der Hucht K., Herrero A., Esteban C., eds, Vol. 212, A Massive Star Odyssey: From Main Sequence to Supernova. p. 365 (arXiv:astro-ph/0209041)

Orosz J. A., Jain R. K., Bailyn C. D., McClintock J. E., Remillard R. A., 1998, ApJ, 499, 375

Osaki Y., 1974, PASJ, 26, 429

Paice J. A., et al., 2019, MNRAS, 490, L62

Paice J. A., et al., 2021, MNRAS, 505, 3452

Park S. Q., et al., 2004, ApJ, 610, 378

Parmar A. N., Oosterbroek T., Boirin L., Lumb D., 2002, A&A, 386, 910

Paul B., Gopala Krishna M. R., Puthiya Veetil R., 2016, in 41st COSPAR Scientific Assembly. pp E1.15–8–16

Pedersen H., 1983, The Messenger, 34, 21

Pinto C., et al., 2017, MNRAS, 468, 2865

Ponti G., Fender R. P., Begelman M. C., Dunn R. J. H., Neilsen J., Coriat M., 2012, MNRAS, 422, L11

Ponti G., Bianchi S., De Marco B., Bahramian A., Degenaar N., Heinke C. O., 2019, MNRAS, 487, 858

Poutanen J., Veledina A., Zdziarski A. A., 2018, A&A, 614, A79

Poutanen J., et al., 2021, arXiv e-prints, p. arXiv:2109.07511

Prabhakar G., Mandal S., Athulya M. P., Nandi A., 2022, MNRAS, 514, 6102

Prabhakar G., Mandal S., Bhuvana G. R., Nandi A., 2023, MNRAS, 520, 4889

Predehl P., et al., 2021, A&A, 647, A1

Pretorius F., 2005, Phys. Rev. Lett., 95, 121101

Pringle J. E., 1981, ARA&A, 19, 137

Pringle J. E., Rees M. J., 1972, A&A, 21, 1

Radhika D., Nandi A., Agrawal V. K., Seetha S., 2016, MNRAS, 460, 4403

Reeves J. N., et al., 2009, ApJ, 701, 493

Remillard R. A., McClintock J. E., 2006, ARA&A, 44, 49

Remillard R. A., Sobczak G. J., Muno M. P., McClintock J. E., 2002, ApJ, 564, 962

Remillard R. A., et al., 2021, arXiv e-prints, p. arXiv:2105.09901

Reynolds C. S., 1999, in Poutanen J., Svensson R., eds, Astronomical Society of the Pacific Conference Series Vol. 161, High Energy Processes in Accreting Black Holes. p. 178 (arXiv:astro-ph/9810018)

Rhoades C. E., Ruffini R., 1974, Phys. Rev. Lett., 32, 324

Robinson E. L., Ivans I. I., Welsh W. F., 2002, ApJ, 565, 1169

Rodi J., Tramacere A., Onori F., Bruni G., Sànchez-Fernàndez C., Fiocchi M., Natalucci L., Ubertini P., 2021, ApJ, 910, 21

Ross R. R., Fabian A. C., Young A. J., 1999, MNRAS, 306, 461

Russell D. M., Fender R. P., Hynes R. I., Brocksopp C., Homan J., Jonker P. G., Buxton M. M., 2006, MNRAS, 371, 1334

Russell D. M., Casella P., Kalemci E., Vahdat Motlagh A., Saikia P., Pirbhoy S. F., Maitra D., 2020, MNRAS, 495, 182

Rybicki G. B., Lightman A. P., 1979, Radiative processes in astrophysics. John Wiley & Sons, Inc

Sánchez-Sierras J., Muñoz-Darias T., 2020, A&A, 640, L3

Schwarzschild K., 1999, arXiv e-prints, p. physics/9905030

Shafee R., McClintock J. E., Narayan R., Davis S. W., Li L.-X., Remillard R. A., 2006, ApJ, 636, L113

Shakura N. I., Sunyaev R. A., 1973, A&A, 24, 337

Shappee B. J., et al., 2014, ApJ, 788, 48

Shidatsu M., et al., 2013, ApJ, 779, 26

Shidatsu M., et al., 2018, ApJ, 868, 54

Shidatsu M., Nakahira S., Murata K. L., Adachi R., Kawai N., Ueda Y., Negoro H., 2019, ApJ, 874, 183

Sim S. A., Long K. S., Miller L., Turner T. J., 2008, MNRAS, 388, 611

Sim S. A., Miller L., Long K. S., Turner T. J., Reeves J. N., 2010, MNRAS, 404, 1369

Singh K. P., et al., 2017, Journal of Astrophysics and Astronomy, 38, 29

Singh K. P., Stewart G., Chandra S., Dewangan G. C., Bhattacharyya S., Kamble N. S., Vishwakarma S., Koyande J. G., 2021, Journal of Astrophysics and Astronomy, 42, 77

Soffitta P., 2017, in Siegmund O. H., ed., Society of Photo-Optical Instrumentation Engineers (SPIE) Conference Series Vol. 10397, Society of Photo-Optical Instrumentation Engineers (SPIE) Conference Series. p. 103970I, doi:10.1117/12.2275485

Sreehari H., Ravishankar B. T., Iyer N., Agrawal V. K., Katoch T. B., Mandal S., Nandi A., 2019, MNRAS, 487, 928

Stella L., Vietri M., 1998, ApJ, 492, L59

Stella L., Vietri M., Morsink S. M., 1999, ApJ, 524, L63

Stern B. E., Begelman M. C., Sikora M., Svensson R., 1995, MNRAS, 272, 291

Stiele H., Kong A. K. H., 2020, ApJ, 889, 142

Stirling A. M., Spencer R. E., de la Force C. J., Garrett M. A., Fender R. P., Ogley R. N., 2001, MNRAS, 327, 1273

Sunyaev R. A., Titarchuk L. G., 1980, A&A, 500, 167

Sunyaev R. A., Titarchuk L. G., 1985, A&A, 143, 374

Sunyaev R. A., Truemper J., 1979, Nature, 279, 506

Svensson R., 1996, A&AS, 120, 475

Szostek A., Zdziarski A. A., 2008, MNRAS, 386, 593

Tagger M., Pellat R., 1999, A&A, 349, 1003

Takizawa M., et al., 1997, ApJ, 489, 272

Tanaka Y., Inoue H., Holt S. S., 1994, PASJ, 46, L37

Tananbaum H., Kellogg E., Gursky H., Murray S., Schreier E., Giacconi R., 1971, ApJ, 165, L37

Tetarenko A. J., et al., 2021, MNRAS, 504, 3862

Thorne K. S., 1974, ApJ, 191, 507

Titarchuk L., 1994, in Fichtel C. E., Gehrels N., Norris J. P., eds, American Institute of Physics Conference Series Vol. 304, The Second Compton Symposium. pp 380–384, doi:10.1063/1.45591

Tombesi F., Meléndez M., Veilleux S., Reeves J. N., González-Alfonso E., Reynolds C. S., 2015, Nature, 519, 436

Torrejón J. M., Schulz N. S., Nowak M. A., Kallman T. R., 2010, ApJ, 715, 947

Torres M. A. P., Casares J., Jiménez-Ibarra F., Muñoz-Darias T., Armas Padilla M., Jonker P. G., Heida M., 2019, ApJ, 882, L21

Torres M. A. P., Casares J., Jiménez-Ibarra F., Álvarez-Hernández A., Muñoz-Darias T., Armas Padilla M., Jonker P. G., Heida M., 2020, ApJ, 893, L37

Tucker M. A., et al., 2018, ApJ, 867, L9

Ueda Y., Inoue H., Tanaka Y., Ebisawa K., Nagase F., Kotani T., Gehrels N., 1998, ApJ, 492, 782

Ueda Y., Murakami H., Yamaoka K., Dotani T., Ebisawa K., 2004, ApJ, 609, 325

Uttley P., Cackett E. M., Fabian A. C., Kara E., Wilkins D. R., 2014, A&ARv, 22, 72

Uttley P., et al., 2018, The Astronomer's Telegram, 11423, 1

van Paradijs J., McClintock J. E., 1994, A&A, 290, 133

van der Klis M., 1989, ARA&A, 27, 517

van der Klis M., 2006, Advances in Space Research, 38, 2675

Vyas M. K., Kumar R., Mandal S., Chattopadhyay I., 2015, in Astronomical Society of India Conference Series. pp 109–110

Walton D. J., et al., 2016, ApJ, 826, L26

Wang Y., et al., 2020, ApJ, 896, 33

Wang J., et al., 2021, ApJ, 910, L3

Weisskopf M. C., 1999, arXiv e-prints, pp astro–ph/9912097

Weisskopf M. C., et al., 2016, in den Herder J.-W. A., Takahashi T., Bautz M., eds, Society of Photo-Optical Instrumentation Engineers (SPIE) Conference Series Vol. 9905, Space Telescopes and Instrumentation 2016: Ultraviolet to Gamma Ray. p. 990517, doi:10.1117/12.2235240

Wilkins D. R., Fabian A. C., 2011, MNRAS, 414, 1269

Wilkins D. R., Gallo L. C., 2015, MNRAS, 448, 703

Wilkins D. R., Cackett E. M., Fabian A. C., Reynolds C. S., 2016, MNRAS, 458, 200

Wilms J., Allen A., McCray R., 2000, ApJ, 542, 914

Yadav J. S., et al., 2016, in den Herder J.-W. A., Takahashi T., Bautz M., eds, Society of Photo-Optical Instrumentation Engineers (SPIE) Conference Series Vol. 9905, Space Telescopes and Instrumentation 2016: Ultraviolet to Gamma Ray. p. 99051D, doi:10.1117/12.2231857

You B., et al., 2021, Nature Communications, 12, 1025

Zdziarski A. A., Fabian A. C., Nandra K., Celotti A., Rees M. J., Done C., Coppi P. S., Madejski G. M., 1994, MNRAS, 269, L55

Zdziarski A. A., Johnson W. N., Magdziarz P., 1996, MNRAS, 283, 193

Zdziarski A. A., Szanecki M., Poutanen J., Gierliński M., Biernacki P., 2020, MNRAS, 492, 5234

Zdziarski A. A., You B., Szanecki M., Li X.-B., Ge M.-Y., 2021a, arXiv e-prints, p. arXiv:2112.08116

Zdziarski A. A., Dziełak M. A., De Marco B., Szanecki M., Niedźwiecki A., 2021b, ApJ, 909, L9

Zhang W., Jahoda K., Swank J. H., Morgan E. H., Giles A. B., 1995, ApJ, 449, 930

Zoghbi A., Kalli S., Miller J. M., Mizumoto M., 2020, ApJ, 893, 97

van Paradijs J., 1996, ApJ, 464, L139

van der Klis M., 2000, ARA&A, 38, 717

List of Publications

Refereed Journals

1. **Prabhakar G.**, Mandal S., Bhuvana G. R., Nandi A., "Wideband Study of the Brightest Black Hole X-ray Binary 4U 1543−47 in the 2021 Outburst: Signature of Disk-Wind Regulated Accretion", 2023, MNRAS, 520, 4889.

2. **Prabhakar G.**, Mandal S., Athulya M. P., Nandi A., "Accretion scenario of MAXI J1820+070 during 2018 outbursts with multimission observations", 2022, MNRAS, 514, 6102.

3. Dihingia I. K., Das S., **Prabhakar G .**, Mandal S., "Properties of two- temperature magnetized advective accretion flow around rotating black hole", 2020, MNRAS, 496, 3043.

4. **Prabhakar G.**, Mandal S., Bhuvana G. R., Nandi A., "Comparative spectro-temporal studies of thermal state dominated outbursts ", 2023 (under preparation).

Conferences

1. 'Wideband spectro-temporal analysis of MAXI J1820+070 during 2018 outbursts', Oral presentation on *Young Astronomers' Meet 2022*, November 2022, Aryabhatta Research Institute of Observational Sciences, Nainital.

2. 'Wideband spectral analysis of the brightest BH-XRB 4U 1543−47 in 2021 Outburst', Oral presentation on *National conference on REcent Trends in the study of Compact Objects (RETCO-V): Theory and Observation*, April 2023, Kodaikanal Solar Observatory.

Appendix A

Swift/XRT and *NICER* Spectral Calibration Discrepancies

The estimation of spectral parameters gets affected due to the difference in spectral energy calibration of *XRT* and *NICER*. To understand it better, we model two pairs of simultaneous *NICER* and *XRT* observations; the first one is on MJD 58212 (Pair-I) and the second observation (Pair-II) is on ∼ MJD 58401 (Pair-II is quasi-simultaneous, but the source did not evolve significantly during the observations).

Pair-I observation is close to the peak of Outburst-I, and the model `tbabs(diskbb+powerlaw)` provides a good fitting for *XRT* data. In contrast, *NICER* data need an additional Gaussian component due to Fe K_α emission line signature. The fitted spectra for *XRT* and *NICER* data are plotted together in Fig. A.1a. Here, orange represents the *XRT* spectrum, and the green represents the *NICER* spectrum. Pair-II observation is close to the quiescence after Outburst-II. The `tbabs(diskbb+powerlaw)` model is needed to fit the *NICER* data, but only `tbabs×powerlaw` is enough to fit the *XRT* data and the model fitting is presented in Fig. A.1b. For a given simultaneous observation, the requirement of additional model components for *NICER* data implies that the *NICER* calibration is still updating since *Swift/XRT* is well calibrated with other instruments (Madsen et al., 2017).

We attempt an order-of-magnitude estimation of the spectral discrepancies between the instruments from these simultaneous observations. The model-fitted parameters and estimated fluxes in various energy bands are summarised in Table A.1. We find that the overall (0.8 – 10 keV) flux matched well when the source was bright (Pair-I) though *NICER* flux in the high-energy (2 – 10 keV) band is 7.1% lower than the *XRT* flux due to a steeper spectral index (difference of ∼ 0.24). However, the inner disk temperature, T_{in}, is comparable, but a higher *diskbb norm* reflects 5.8% higher flux in the low-energy (0.8 – 2 keV) band. Therefore, there is a mutual balance between the low and high-energy fluxes,

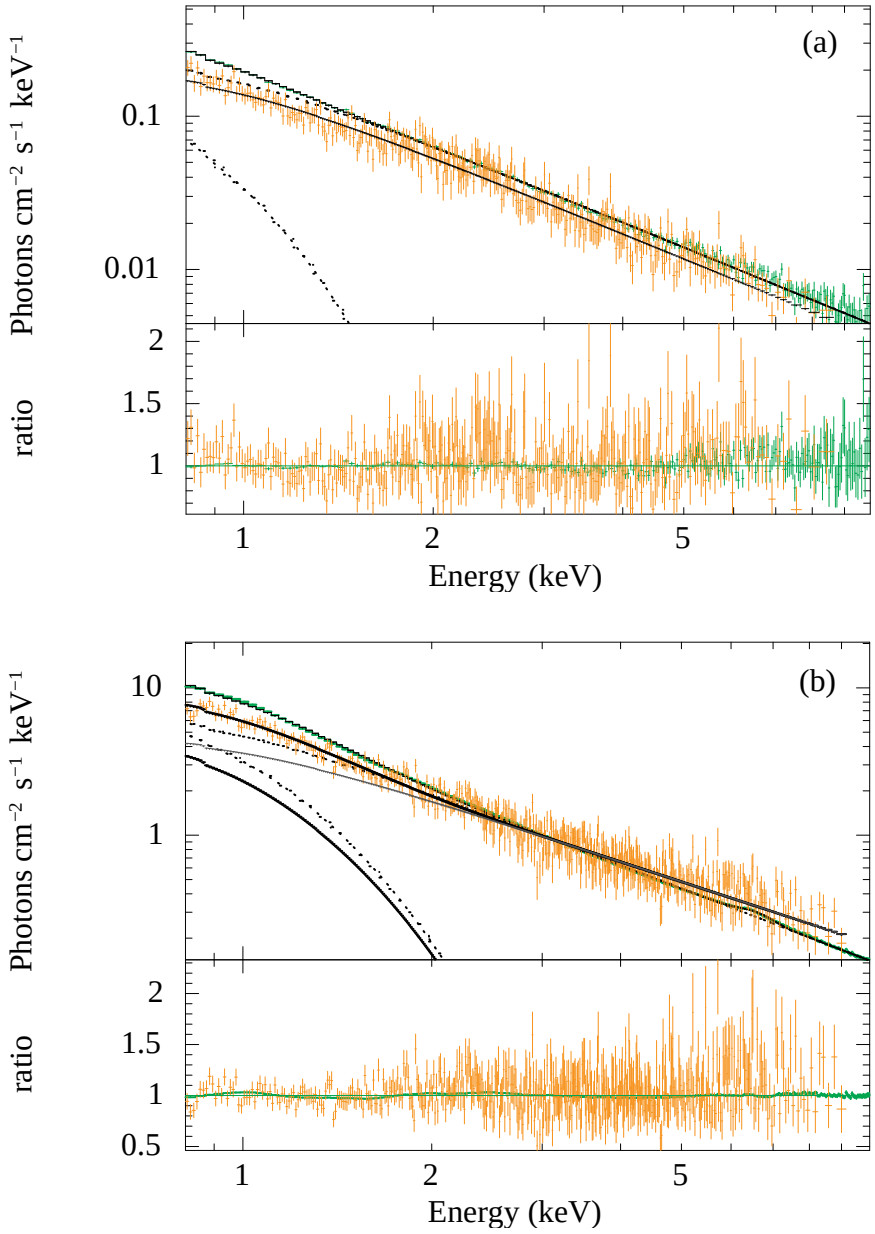

Figure A.1: **(a)** Simultaneous *XRT* and *NICER* spectrum on MJD 58212 fitted using `tbabs(diskbb+powerlaw)` for *XRT* and `tbabs(diskbb+gauss+powerlaw)` for *NICER*, and are plotted together. The orange colour corresponds to the *XRT*, and the green is for *NICER*. **(b)** Quasi-simultaneous observation on ∼ MJD 58401 are fitted using `tbabs×powerlaw` and `tbabs(diskbb+powerlaw)` for *XRT* and *NICER* respectively with the same colour scheme.

keeping the overall fluxes comparable when the source is bright. Note that the *XRT* flux in the 0.8 − 10 keV band is used as a reference to calculate the percentage of flux difference.

The spectral index for the Pair-II data set appears comparable. But a higher *powerlaw norm*

Table A.1: Model fitted parameters and estimated fluxes in various energy bands from simultaneous *NICER-XRT* fittings

Model	Component	Pair I		Pair II	
		NICER	*XRT*	*NICER*	*XRT*
`powerlaw`	Γ	$1.648^{+0.004}_{-0.004}$	$1.41^{+0.07}_{-0.07}$	$1.70^{+0.01}_{-0.01}$	$1.69^{+0.03}_{-0.03}$
	norm	$6.16^{+0.04}_{-0.04}$	$4.68^{+0.05}_{-0.05}$	$0.214^{+0.003}_{-0.003}$	$0.179^{+0.004}_{-0.004}$
`diskbb`	$T_{in}(keV)$	$0.283^{+0.004}_{-0.004}$	$0.30^{+0.04}_{-0.03}$	$0.18^{+0.01}_{-0.01}$	-
	norm ($\times 10^4$)	$11.1^{+0.68}_{-0.63}$	$6.78^{+4.7}_{-2.4}$	$1.43^{+0.78}_{-0.47}$	-
`gauss`	*line E* (keV)	$6.60^{+0.04}_{-0.04}$	-	-	-
	sigma (keV)	$0.6^{\dagger}$	-	-	-
	norm	$0.034^{+0.002}_{-0.002}$	-	-	-
χ^2_{red}		1.02	1.16	1.04	0.86
Flux (ergs/s/cm^2)	Energy range	($\times 10^{-8}$)	($\times 10^{-8}$)	($\times 10^{-9}$)	($\times 10^{-9}$)
	0.8-10 keV	$3.945^{+0.002}_{-0.002}$	$4.00^{+0.03}_{-0.06}$	$1.189^{+0.004}_{-0.007}$	$0.98^{+0.01}_{-0.01}$
	0.8-2 keV	$1.180^{+0.001}_{-0.002}$	$0.948^{+0.003}_{-0.020}$	$0.314^{+0.007}_{-0.003}$	$0.242^{+0.002}_{-0.003}$
	2-10 keV	$2.765^{+0.002}_{-0.002}$	$3.05^{+0.06}_{-0.04}$	$0.874^{+0.005}_{-0.005}$	$0.74^{+0.01}_{-0.01}$

† frozen parameter.

and the presence of additional `disk` components record 13.6% and 7.3% higher flux in the high and low-energy band, respectively, for *NICER*. Therefore, we find considerable discrepancies between fluxes in the high and low-energy bands due to the differences in spectral response.

Finally, the simultaneous multi-mission observation campaign of quasar 3C 273 involving *NuSTAR, Swift*, and *NICER* were performed on 2019-07-02, 2020-07-06, and 2021-06-09. The recent report (Madsen et al., 2021) of the International Astronomical Consortium for High Energy Calibration (IACHEC) has mentioned that the data analysis of these observations is underway. Therefore, the *NICER* calibration is still evolving, and

proper *NICER-Swift/XRT* cross-calibration is very much required.